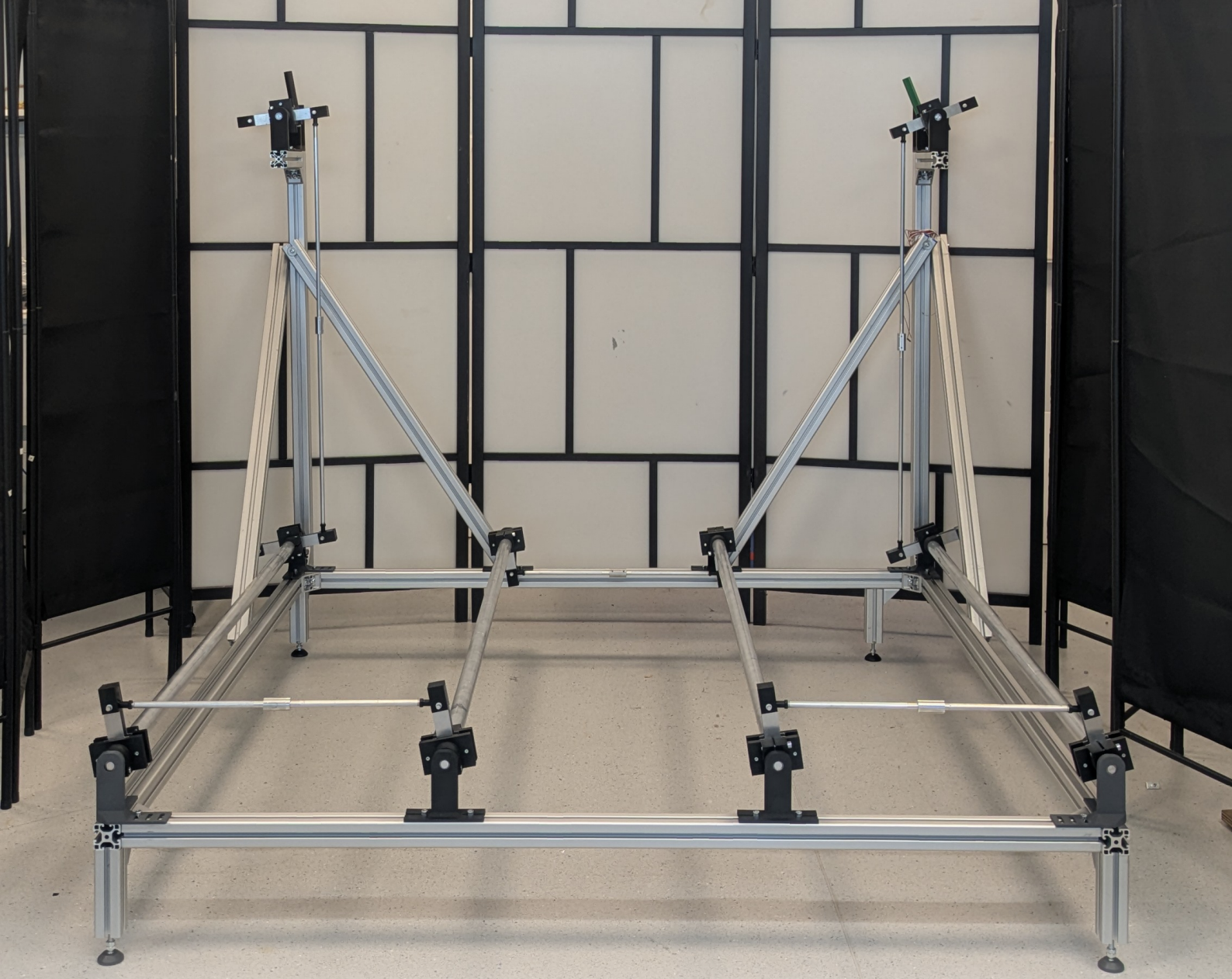

Remote Torque Transmission for MR-Conditional Haptic Manipulation: A Torsion-Rod Approach

Design and Experimental Validation of the MaRCHMan: A Proof-of-Concept Transmission

Thomas Valk

2026

Remote Torque Transmission for MR-Conditional Haptic Manipulation: A Torsion-Rod Approach

Design and Experimental Validation of the MaRCHMan: A Proof-of-Concept Transmission

Master of Science Thesis

For the degree of Master of Science in
Mechanical Engineering
at Delft University of Technology
Department of BioMechanical Engineering

Thomas Valk

June 9, 2026

Preface

This thesis is the result of a graduation project which started in November 2025, carried out at the department of BioMechanical Engineering at Delft University of Technology. The assignment concerned developing a proof-of-concept transmission for a Magnetic Resonance Conditional Haptic Manipulator. This report is a thorough account of the engineering process that led to the resulting prototype.

I am very proud of the end result. The prototype is the largest thing I have ever built, and working on it allowed me to put into practice the theory accumulated throughout my master's and my entire education. At the moment I do not know where my career will go from here, but I will definitely keep building things. Eight years of studying seems like a long time, but it is suddenly over. It was great, definitely would recommend.

I want to thank Mark and Winfred for their academic guidance throughout the project. Their feedback during the validation phase in particular significantly improved the quality of the results. I also want to thank Piet, the discussions we had via e-mail have greatly improved the prototype.

I want to thank my friends for the many coffee breaks I needed. Thank you to everyone in the RobotLab downstairs. I really needed space to build what I wanted, and I found it there. I hope you could tolerate the mess. Thank you to my roommates and family for your support. Lastly, thank you Anieke, for your endless positivity and support.

Thomas Valk

Delft, June 2026

Remote Torque Transmission for MR-Conditional Haptic Manipulation: A Torsion-Rod Approach

T.A. Valk
Supervisors: W. Mugge, M. van de Ruit, P. Lammertse

***Abstract*—Combining EEG (electroencephalography) and fMRI (functional Magnetic Resonance Imaging) in motor control research requires a haptic manipulator capable of operating safely in both environments. Conventional electromagnetic actuators are incompatible with MRI, requiring motion and force to be transmitted mechanically from outside the scanner room into the bore. Transmission length, friction, and backlash are the primary performance bottlenecks in such systems.**

A hybrid torsion-pushrod architecture was selected through systematic elimination of cable-driven, pneumatic, and hydraulic transmission families. Pneumatic and hydraulic systems introduce compliance-driven nonlinearities that limit bandwidth and force fidelity. C able-driven M R-Conditional transmissions achieve control bandwidths of only $10\,\mathrm{Hz}$, falling short of the $20\,\mathrm{Hz}$ requirement. Rigid linkage systems remained as the only viable path, and a hybrid torsion-pushrod concept was developed that navigates direction changes via crank-and-pushrod stages while covering straight segments with torsion rods. The resulting proof-of-concept prototype, the MaRCHMan (Magnetic Resonance Conditional Haptic Manipulator), transmits motion over a total length of $9\,\mathrm{m}$ with no actuators or electronics inside the scanner room.

Two configurations r epresenting g eometric e xtremes were validated: a square layout incorporating ten 90° bends, and a straight-line layout without corner joints. Most proof-of-concept requirements were satisfied b y b oth c onfigurations, in cluding a control bandwidth exceeding $20\,\mathrm{Hz}$, torque transmission of at least $1.2\,\mathrm{N\,m}$, and a range of motion of $[-42^\circ, 42^\circ]$. The square configuration a chieved a r esonance f requency o f $15.0\,\mathrm{Hz}$ and a $-3\,\mathrm{dB}$ bandwidth of $24.1\,\mathrm{Hz}$; the straight-line configuration achieved a resonance frequency of $27.5\,\mathrm{Hz}$ with an extrapolated bandwidth of $46.9\,\mathrm{Hz}$. The square configuration i s substantially less stiff than the straight-line configuration ($k_\mathrm{A} = 14.5\,\mathrm{N\,m/rad}$ versus $k_\mathrm{B} = 48.5\,\mathrm{N\,m/rad}$). A series compliance model identified the 3D-printed bearing housings as the dominant compliance source. Pushrod axial stiffness is approximately three orders of magnitude higher than bearing housing compliance and does not contribute to the bottleneck. Including out-of-plane bearing housing deflection a t a n e stimated m isalignment f raction of $\alpha = 0.3$ reduces the model prediction from $38.1\,\mathrm{N\,m/rad}$ to $19\,\mathrm{N\,m/rad}$, approaching the measured value. Replacing the 3D-printed housings with stiffer alternatives is predicted to raise the Square Configuration r esonance f requency f rom $15.0\,\mathrm{Hz}$ to approximately $31\,\mathrm{Hz}$, exceeding the $20\,\mathrm{Hz}$ target. The current prototype uses steel fasteners and bearings; MR-Conditional material substitution and in-bore validation are identified a s the primary next steps toward a clinically deployable system.

***Index Terms*—MR-Conditional, haptic manipulation, torsion-rod transmission, transmission design, system identification, frequency response, mechanical design, robotics**

Delft University of Technology, Delft, 2628CD, The Netherlands

An electronic version of this thesis is available at http://repository.tudelft.nl

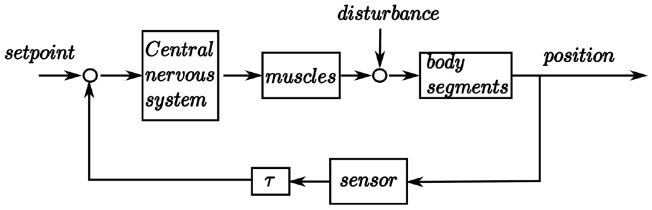

Fig. 1: Schematic representation of the human motor control loop. A desired limb position (setpoint) is generated in the brain. The position is compared with the actual position of the limb. Next, the central nervous system (CNS) sends a neural signal to the muscles. The muscles generate forces that move the limb, while external forces act as disturbances. Sensory signals are fed back to the brain with a small delay(τ) due to physical transmission and neural processing time [6].

I. Introduction

HUMAN motion control results from the interaction between the nervous and musculoskeletal systems, and is often described as a closed-loop control process which integrates sensory feedback, plans motor commands and executes movement [1, 2]. Understanding motion control is fundamental for neuroscience and is essential for the diagnosis and treatment of neurological disorders such as stroke, Parkinson's disease and multiple sclerosis, which together account for a major share of neurological disease worldwide [3].

System identification techniques are used to characterize the dynamics of human motion control, by comparing the system's output to varying inputs [4]. Such analysis allows estimation of how the central nervous system transforms sensory input into motor output. An example of the approach can be illustrated by a task in which a participant moves their hand between targets while cortical activity is being measured with EEG. If the task is repeated while the hand is perturbed by some manipulator, the evoked cortical activity will give information about the motor cortex [5]. Figure 1 illustrates how sensory feedback enables accurate movement.

Several studies investigated brain activity through EEG measurements, such as the study by Vlaar et al., who demonstrated that combining EEG and robotic manipulation allowed for quantitative assessment of evoked cortical activity using a haptic manipulator. A haptic manipulator is a robotic system designed to interact with its user through force feedback,

allowing the user to have physical interaction with the robotic system [7, 8]. Sharifi et al. demonstrated the potential of the haptic manipulation approach for clinical application by applying controlled wrist perturbations during fMRI to separately identify motor and sensory contributions to tremor in essential tremor and Parkinson's disease patients [9]. Sharifi et al. used a haptic manipulator developed by Bode et al. during a thesis project at TU Delft. Another study by Vlaar et al. used fMRI with an MR-Conditional torque measuring device and showed that safe measurements in the MR scanner room are feasible [11]. Ahmad et al. [12] argued that simultaneous EEG-fMRI can provide a more complete understanding of brain function and dysfunction. Although the complementary nature of EEG (high temporal resolution) and fMRI (high spatial resolution) is appealing, simultaneous recordings are challenging due to electromagnetic interference (EMI) introducing noise on the MR image [13].

If simultaneous measurement is not possible, sequential measurement must be explored. Using the same haptic manipulator for both EEG and fMRI sessions ensures that task conditions remain identical, so any differences in brain activity can be attributed to the measurement modality rather than changes in the experimental setup. A dedicated device is therefore needed that can operate safely in both environments. Devices intended for use in MR environments must meet criteria defined by the American Society for Testing and Materials (ASTM) to be rated either MR-Safe or MR-Conditional [14, 15]. An MR-Safe device poses no known hazards in any MR environment, whereas an MR-Conditional device is safe to use only under specific conditions, including conditions for the static magnetic field, the time-varying gradient magnetic fields, and the radiofrequency fields. For a haptic manipulator in fMRI, MR-Conditional is the practical target rating, as the mechanical and force-feedback requirements of the device make a fully non-metallic, MR-Safe design difficult to achieve without compromising performance. The dedicated device for sequential measurements must therefore be an MR-Conditional Haptic Manipulator (MRCHM).

Since conventional electromagnetic (EM) actuators are incompatible with the MR environment due to electromagnetic interference and heating, actuators must be placed outside the bore, ideally in the adjacent control room. The bore is the cylindrical opening of the MRI scanner where the patient is positioned during imaging. Transmitting motion and force from the actuator into the bore requires a transmission system, and backlash, friction, and compliance inherent to any transmission will degrade haptic performance at the end-effector. The transmission is therefore a critical performance bottleneck in any remotely actuated MRCHM.

An alternative approach places (non electromagnetic) actuators directly inside the bore using non-magnetic actuator types such as piezoelectric, ultrasonic, or shape memory alloy (SMA) actuators [16–18]. The limited space inside the bore restricts actuator size and therefore torque output [16, 17], and the low control bandwidth of these actuator types makes them unsuitable for haptic manipulation. Furthermore, because direct-drive actuators are partly constructed from conductive materials, they introduce imaging artifacts and are susceptible to heating from eddy currents [18]. In-bore actuation is therefore not a viable path for MRCHM development, and any suitable design must rely on a transmission system. Transmission design is consequently the central engineering challenge in developing an MRCHM.

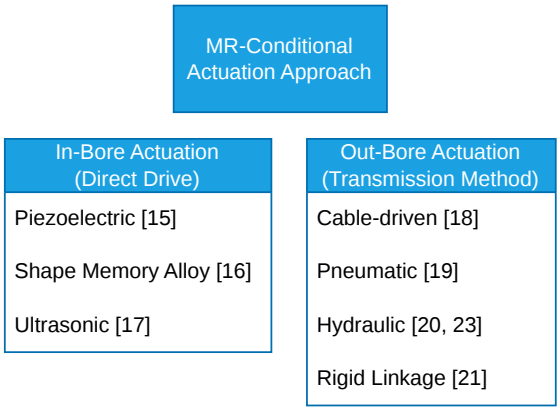

Fig. 2: An overview of current MR-Conditional actuation approaches found in literature, with examples per actuation method.

To understand the influence of transmission design on MRCHM performance, four main transmission categories were identified and compared: cable-driven [19], pneumatic [20], hydraulic [21], and rigid linkage systems [22]. An overview of MR-Conditional actuation approaches is shown in Figure 2. Each category presents trade-offs across control bandwidth, force fidelity, and signal-to-noise ratio (SNR) loss in MR imaging. What specific category performs best in the trade-off context is discussed in Section II. Across all categories, transmission length emerged as the dominant factor governing control bandwidth loss, and increasing the distance between the actuator and the bore proved more effective than electromagnetic shielding [10, 19, 23]. The transmission is therefore the fundamental performance bottleneck of any remotely actuated MRCHM, and without a well-characterized transmission the haptic performance of the complete system cannot be predicted or controlled.

The goal of this work is to address the transmission bottleneck by designing, building, and validating a proof-of-concept transmission for an MRCHM. The research question guiding this work is:

> How can a transmission system for an MR-Conditional haptic manipulator be developed to meet predefined mechanical and MR-Conditionality requirements, and validated through experimental testing?

Two objectives follow from the research question. Objective A is to develop a proof-of-concept prototype. Objective B is to experimentally validate the prototype against stated proof-of-concept requirements and to identify the steps required to realize a fully MR-Conditional system. This project is a continuation of the thesis by Bode et al., who developed a

hydraulic MRCHM. The device was used in a clinical setting by Sharifi et al., but low control bandwidth and leakage made the device hard to use, identifying the need for a better alternative. Nevertheless, requirements developed by Bode et al. can be reused.

The remainder of this paper is structured as follows. Section II describes the requirements, concept selection, and analytical methods for estimating transmission stiffness and reflected mass. Section III presents the preliminary calculations and describes the prototype in both configurations. Section IV describes the experimental validation methods, covering the test setup and excitation signal design. Section V presents the validation results, including stiffness measurements, frequency response characterization, and an analytical compliance breakdown identifying the dominant compliance sources for both configurations. Section VI interprets the results against the stated requirements, explains the discrepancy between predicted and measured stiffness, and outlines the steps required to realize a fully MR-Conditional transmission. Section VII states the conclusions. The design and iteration process leading to the prototype, and the data for the compliance and mass models is documented in Appendix A. The excitation signal documentation is provided in Appendix B.

II. Methodology A

A. Methods Part I: Requirements and Prototype Development

Building a fully MR-Conditional prototype introduces practical constraints that would significantly slow development. Commonly available components such as steel bolts and standard bearings are not MR-Conditional and would therefore need to be replaced with expensive MR-Conditional alternatives like ceramic bearings and nylon bolts. Investing in expensive MR-Conditional materials before the mechanical concept is validated would be costly. The project therefore distinguishes between two requirement categories: concept requirements and proof-of-concept (PoC) requirements. Concept requirements define what the final MR-Conditional transmission must achieve. PoC requirements define what the current prototype must demonstrate to validate the underlying mechanical principle. The prototype is designed such that it can be transformed into a fully MR-Conditional transmission by substituting ferromagnetic and conductive components with MR-Conditional equivalents without changing the fundamental architecture. How the performance is expected to change when MR-Conditional components are implemented is discussed in Section VI.

The concept requirements, partially adopted from the earlier TU Delft MRCHM thesis by Bode et al. [10], are:

- The transmission must be constructed entirely from MR-Conditional materials.
- The system must not pose hazard risks in an MR environment, must not cause imaging artifacts, and must not degrade fMRI image quality.
- The transmission must be modular; adjacent transmission units must be connectable within two minutes each.
- The transmission must not obstruct patient access or scanner operation.

The proof-of-concept requirements are:

- The transmission must offer at least one degree of freedom, sufficient for wrist perturbation experiments.
- The system must be capable of transmitting a torque of at least $1.2\,\mathrm{N\,m}$, sufficient to overcome wrist joint resistance during perturbation tasks [10, 27].
- The control bandwidth at the output must be at least $20\,\mathrm{Hz}$. The eigenfrequency of a contracted human wrist is approximately $15\,\mathrm{Hz}$ [28], and all relevant arm dynamics are excited below $20\,\mathrm{Hz}$ [29]. A bandwidth of at least $20\,\mathrm{Hz}$ is therefore required to cover the full frequency range of interest [10, 30].
- The transmission must allow a range of motion of at least 40° from neutral. A range of $[-40^\circ, 40^\circ]$ is sufficient to allow functional flexion and extension movement of the wrist joint, and excluding abduction-adduction simplifies the design without limiting the motion of interest [10, 28, 30].
- The transmission must function independently of any specific MRI scanner or facility.
- Joints must allow for 90° bends.
- Joints must have zero backlash.
- Static friction in the joints must be less than $0.0225\,\mathrm{N\,m}$ per joint, equivalent to $0.3\,\mathrm{N}$ at the $75\,\mathrm{mm}$ crank radius. No standardized threshold was identified in the literature; lower static friction is always preferable for haptic transparency, and $0.3\,\mathrm{N}$ was adopted as a practical upper bound based on the force range of the target application.

B. Concept Selection

Transmission categories were evaluated against four performance criteria: control bandwidth, force fidelity, MR-Conditionality, and friction and backlash. An overview of the transmission category trade-offs is given in Table I. Pneumatic systems suffer from compressibility, which introduces compliance and limits control bandwidth [20]. Hydraulic systems suffer from nonlinearities due to cavitation and compliance in tubing [10]. Pneumatic and hydraulic transmissions were therefore eliminated early in concept development.

Cable transmissions were eliminated on three grounds. First, cables are inherently compliant and require continuous pretensioning, which increases system friction and makes long-term reproducibility difficult to maintain [23, 24]. Second, Bowden cable configurations exhibit nonlinear friction between cable and sheath [25], which is difficult to characterize and would compromise force fidelity in a haptic setting. Third, cable-driven MR-Conditional transmissions reported in the literature achieve control bandwidths of only $10\,\mathrm{Hz}$ [19, 23], which falls short of the $20\,\mathrm{Hz}$ requirement.

Rigid linkage systems remained as the only viable family. A pure pushrod transmission offers high stiffness and predictable kinematics, but navigating the 90° bends required between the control room and the scanner bore requires a rocker arm at each bend to redirect the push-pull force, as shown in Figure 3. Each rocker arm introduces an additional joint, and every joint adds friction and backlash. A minimal installation already requires four direction changes, shown in Figure 4.

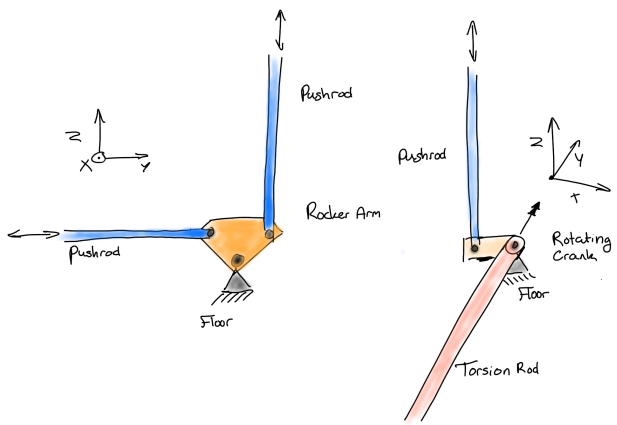

Fig. 3: *Left:* A pure pushrod system requires a rocker arm (orange) at each 90° bend, increasing joint count and bulk. *Right:* A torsion rod (red) transmits torque along the rod axis (y) and requires only a single crank-pushrod stage per bend.

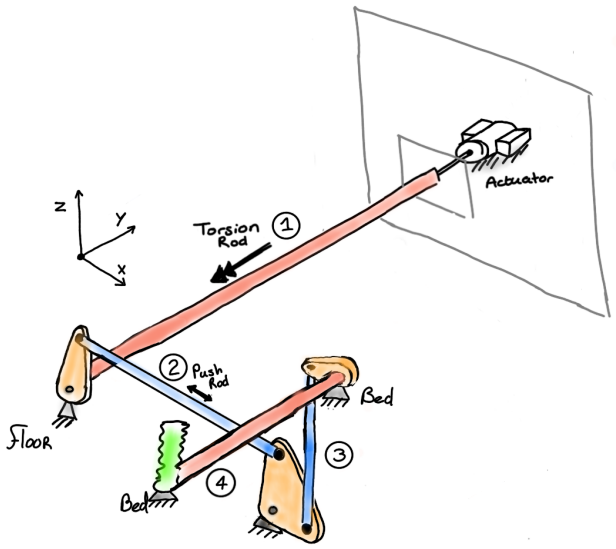

Fig. 4: Schematic of the selected torsion-pushrod concept. The actuator is located outside the MRI room and the end-effector interfaces with the patient at the MRI bed. The torsion rod (red) enters the scanner room through the wall, parallel to the bore axis (segment 1). The bore axis itself is not shown. A pushrod redirects motion laterally to the bed position (segment 2). A second pushrod rises vertically to bed height (segment 3). A final torsion rod extends into the bore to the patient interface (segment 4)

In a more complex room geometry the bend count increases further, and the cumulative joint count, backlash, and bulk become difficult to manage over a total transmission path of approximately 9 m [10]. The Square Configuration tested in this work, with ten 90° bends, therefore represents an upper bound on installation complexity.

Torsion rods reduce joint count by transmitting torque torsionally along the rod axis, so that a direction change requires only a single compact crank-and-pushrod stage rather than a dedicated rocker arm. A crank-and-pushrod stage is required as a purely torsional transmission is not feasible in practice: connecting two torsion rods at an angle requires a coupling that transmits torque across a change in axis direction. The standard solutions are universal joints and bevel gears, but both require clearance to function and therefore introduce backlash, which is incompatible with the zero-backlash requirement. No backlash-free torsion-to-torsion coupling was identified in the literature or among commercially available components.

A hybrid torsion-pushrod concept resolves the coupling problem. Pushrods transmit force linearly and connect to a rotating crank via a spherical rod end bearing, which has minimal backlash when properly assembled. Direction changes at each bend are handled by a crank-pushrod stage, eliminating the need for universal joints or bevel gears entirely. The torsion rods cover the long straight segments where their compactness is most beneficial, particularly inside the bore where space is limited. The pushrods handle direction changes. An example of the MRI installation geometry is shown schematically in Figure 4.

1) Torsion Rod Performance Estimate: Before committing to the hybrid concept, calculations were performed to confirm that torsion rods of practical dimensions are sufficiently stiff to meet the 20 Hz bandwidth requirement over the required transmission length.

In a torsional transmission, the shear modulus G governs torsional stiffness, whereas in a pure pushrod configuration the elastic modulus E governs axial stiffness. For an isotropic material, $G = E/2(1+\nu)$, so for aluminum with $\nu \approx 0.33$, $G \approx 0.376\,E$. The following calculations use aluminum as the example material. The method applies to any isotropic candidate material.

To contextualize the hybrid concept, the resonance frequency was estimated for three limiting cases: a pure pushrod transmission, a pure torsion-rod transmission, and the hybrid alternating configuration, all over a total length of 9 m. The axial stiffness of a pushrod is

TABLE I: Comparison of MR-Conditional transmission families across key performance criteria.

Family	Bandwidth	Force fidelity	MR-Cond.	Friction/backlash	Sources
Cable-driven	+	+	++	−	[19, 23–25]
Pneumatic	−−	−−	++	−	[20, 26]
Hydraulic	−−	+	+	−−	[10, 21]
Rigid linkage	++	++	+	+	[22]

$$k_{\text{push}} = \frac{EA}{L} \tag{1}$$

where $E = 69\,\text{GPa}$ is the elastic modulus of aluminum, $A = \pi(r_{\text{outer}}^2 - r_{\text{inner}}^2)$ is the cross-sectional area of the pushrod tube, and L is the total length. The converted stiffness at the crank radius $r_{\text{crank}} = 75\,\text{mm}$ is $k_{\text{torsion}} = k_{\text{push}} \cdot r_{\text{crank}}^2$. The torsional stiffness of the torsion rod is given by equation 2. The reflected mass per meter for each element type was computed from its geometry and density. Torsional stiffness was estimated as:

$$k = \frac{GJ}{L} \tag{2}$$

where G is the shear modulus of aluminum ($26\,\text{GPa}$), J is the polar second moment of area of the hollow rod cross-section, and L is the rod length. The polar moment was computed as

$$J = \frac{\pi}{2}\left(r_{\text{outer}}^4 - r_{\text{inner}}^4\right) \tag{3}$$

To compare the stiffness of the hybrid torsion-pushrod concept to the pure torsion and pure pushrod concepts, the total stiffness in series is calculated:

$$\frac{1}{k_{\text{total}}} = \frac{1}{k_{\text{push}} \cdot r_{\text{crank}}^2} + \frac{1}{k_{\text{torsion}}} \tag{4}$$

Rather than comparing rotational inertia directly, the analysis uses reflected mass m_{refl}, defined as the equivalent point mass at the crank tip that would produce the same rotational inertia about the crank axis:

$$m_{\text{refl}} = \frac{I}{r_{\text{crank}}^2} \tag{5}$$

Physically, the reflected mass represents how heavy the transmission feels to the actuator: a transmission with a reflected mass of $1\,\text{kg}$ requires the same force to accelerate at the crank tip as a $1\,\text{kg}$ point mass. Comparing reflected mass across configurations allows intuitive assessment of the inertial load imposed on the actuator, independent of the geometry. The resonance frequency is calculated through:

$$f_n = \frac{1}{2\pi}\sqrt{\frac{k_{\text{refl}}}{m_{\text{refl}}}} \tag{6}$$

Based on the elementary equations listed above, the development direction was chosen. The results are presented in Section III. To find the stiffness and reflected mass contribution of every component in the prototype, more in-depth calculations are required.

C. Component Reflected Mass and Compliance

For systems with both distributed and concentrated masses, the effective modal mass at the driven end differs from the total mass. For a torsion rod driven at one end and free at the other, the distributed inertia of the rod itself participates only partially in the first mode: the effective modal inertia of the distributed part is $I_{\text{dist}}/3$, where I_{dist} is the total rotational inertia of all distributed elements [31]. Concentrated masses at the free end, such as the handle, contribute their full inertia. The resonance frequency is therefore:

$$f_n = \frac{1}{2\pi}\sqrt{\frac{k_{\text{refl}}}{I_{\text{dist}}/(3\,r_{\text{crank}}^2) + M_{\text{point}}}} \tag{7}$$

where I_{dist} is the total rotational inertia of the distributed elements: torsion rods and pushrods. r_{crank} is the crank radius, and M_{point} is the sum of all concentrated masses at the crank radius at the final stage of the transmission. Equation 7 is used for the component-level analysis in Section V

To identify the dominant compliance sources in the transmission, the total stiffness was modeled as a series combination of all compliant elements. The total compliance is:

$$C_{\text{total}} = C_{\text{torsion}} + C_{\text{pushrods}} + \sum_i C_{\text{joint},i} \tag{8}$$

where $C = 1/k$ in $\text{rad}\,\text{m}/\text{N}$. The compliance of each element was estimated from its geometry and material properties using the equations introduced above.

The joint assemblies in the prototype consist of several compliant sub-elements in series: the torsion rod clamp, the bearing housing, the aluminum crank plates, and the igus rod end bearing. Each was modeled as a linear elastic element. The bearing housing and the plates were modeled as a beam of length $L_{\text{component}}$, width b, and height h in the loading direction:

$$k_{\text{component}} = \frac{3E_{\text{mat}}I_{\text{component}}}{L_{\text{component}}^3}, \quad I_{\text{component}} = \frac{bh^3}{12} \tag{9}$$

For 3D-printed parts, $I_{\text{component}}$ was adjusted with infill fraction p to account for hollowed parts by $I_{\text{adjusted}} = I_{\text{component}} - I_{\text{infill}}$. Where

$$I_{\text{infill}} = \frac{(1-p)b \cdot (1-p)h^3}{12} \tag{10}$$

Furthermore, the elastic modulus E_{PLA} was adjusted for layer orientation. For components where the loading direction lies out-of-plane with the printed layers, the elastic modulus is reduced to $E_{\text{PLA}}/3$ [32].

An implicit assumption throughout is that the frame is infinitely stiff relative to the transmission elements. Any frame compliance would appear as an additional compliance source in series, consistent with the bottleneck analysis in Section VI. The hybrid concept was developed into a prototype iteratively. The documentation of the iterations is covered in Appendix A. The final stage of iteration is covered in Section III.

III. Results A

A. Preliminary Calculations

Before prototype construction, the resonance frequency was estimated for three transmission configurations using the methods described in Section II: a pure pushrod system, a pure torsion-rod system, and the hybrid alternating configuration selected for development. All estimates assume a total

transmission length of $9\,\mathrm{m}$ and use the prototype dimensions: torsion rods of $30\,\mathrm{mm}$ outer diameter and $1\,\mathrm{mm}$ wall thickness, and pushrods of $10\,\mathrm{mm}$ outer diameter and $1\,\mathrm{mm}$ wall thickness. To include the end-effector in the analysis, a point mass of $0.146\,\mathrm{kg}$ was added, equal to the handle mass reported by Bode et al. [10]. Joint compliance is deliberately excluded from these estimates, the purpose is to establish that the selected rod dimensions are sufficient to meet the $20\,\mathrm{Hz}$ requirement before construction, not to predict the final assembled stiffness. The contribution of joint compliance is characterized analytically in Section V following experimental validation.

TABLE II: Estimated resonance frequency for three transmission configurations over $9\,\mathrm{m}$. Masses include handle point mass of $0.146\,\mathrm{kg}$. $r_{\text{crank}} = 75\,\mathrm{mm}$

Configuration	k (N m/rad)	m (kg)	f_n (Hz)
Pure pushrod	1.24×10^3	0.846	81.2
Pure torsion rod	59.7	0.224	34.6
Hybrid alternating	114	0.535	31.0

The pure torsion-rod estimate of $34.6\,\mathrm{Hz}$ confirms that the selected rod dimensions provide sufficient stiffness for the $20\,\mathrm{Hz}$ requirement in isolation. The hybrid and pure pushrod estimates provide context for interpreting the measured performance of the built prototype, and are discussed further in Section VI. The three-scenario comparison reveals the trade-off inherent to the hybrid concept. A pure pushrod transmission of $9\,\mathrm{m}$ in length achieves the highest stiffness but carries the largest reflected mass, as the pushrod material operates at the full crank radius. A pure torsion-rod transmission minimizes reflected mass due to the small tube radius, but requires backlash-free torsion-to-torsion couplings at every direction change, which are not available commercially. The hybrid alternating configuration has a lower stiffness relative to the pure pushrod case, while reducing reflected mass and reducing the joint count. Comparing the hybrid estimate to the pure torsion-rod estimate also reveals whether the addition of pushrods to the system increases or decreases overall stiffness: since the pushrods are substantially stiffer per unit length when reflected to the crank radius, their inclusion raises the total reflected stiffness relative to a pure torsion-rod system, at the cost of increased reflected mass. The estimated resonance frequency of $31\,\mathrm{Hz}$ for the hybrid configuration exceeds the $20\,\mathrm{Hz}$ requirement, confirming that the concept is mechanically viable. Therefore the rod diameter of $30\,\mathrm{mm}$ was deemed sufficient. The hybrid torsion-pushrod concept was therefore selected as the basis for prototype development.

B. Built Prototype

The resulting prototype was named the MaRCHMan (Magnetic Resonance Conditional Haptic Manipulator) transmission. The prototype is the result of the iterations described in Appendix A. Figure 5 shows both configurations.

The system is mounted on a high-stiffness aluminum extrusion frame with adjustable height for the handles, enabling flexible test configurations. Four torsion rods are connected by five pushrods, with a crank radius of $75\,\mathrm{mm}$ and a transmission ratio of 1:1. Angle sensors (ZF Electronics AN820032 magnetic angle sensor) were fitted to measure the input and output angle, both connected to an Arduino Uno. The total transmission length in the Square Configuration is $9\,\mathrm{m}$, representative of the distance between an MRI bore and the adjacent control room [10]. The torsion rods are each $1500\,\mathrm{mm}$ long, giving a total torsion-rod length of $6\,\mathrm{m}$. The vertical pushrods are $1000\,\mathrm{mm}$ long and horizontal pushrods are $500\,\mathrm{mm}$ long. The torsion rods rotate in steel roller bearings mounted in 3D-printed bearing housings, shown in Figure 6. Rod ends (igus KBRM-06) are threaded onto inserts bonded into the hollow pushrod ends, providing the connections between torsion rods, pushrods, and bearing axles. The use of steel bearings and fasteners is a deviation from MR-Conditionality requirements; the implications of substituting these components with MR-Conditional alternatives are discussed in Section VI. The Square Configuration incorporates ten $90°$ bends. In an actual MRI installation the number and placement of bends will depend on the specific room geometry, and a straight segment is likely to dominate the transmission path. The Straight-Line Configuration was therefore developed by arranging all four torsion rods end-to-end, omitting corner joints. To preserve identical sensor mounting conditions, the input and output pushrods connecting the handles to the torsion rod remain in place. The total transmission length of the Straight-Line Configuration is $7.5\,\mathrm{m}$, consisting of $6\,\mathrm{m}$ of torsion rod and $1.5\,\mathrm{m}$ of pushrod ($1\,\mathrm{m}$ and $0.5\,\mathrm{m}$ segments). The four torsion rods were coupled end-to-end using 3D-printed shaft couplers, each clamped with M6 bolts to create a single $6\,\mathrm{m}$ torsion rod. Intermediate 3D-printed support brackets were added to prevent sagging over the unsupported length. Both are shown in Figure 7. The support brackets use sliding contact without rolling elements.

To evaluate whether the prototype meets the stated proof-of-concept requirements, both configurations were subjected to experimental validation, described in Section IV.

IV. Methodology B

A. Methods Part II: Prototype Validation

1) Frequency Response Measurement: The frequency response of the transmission was estimated using open-loop system identification. The overall measurement chain is illustrated in Figure 8. The transmission input shaft was perturbed by the Proprio, a hydraulic linear actuator capable of applying controlled forces across the frequency range of interest [33]. The coupling between the Proprio and the transmission is shown in Figure 9. The control bandwidth is defined as the frequency at which the FRF magnitude first crosses the $-3\,\mathrm{dB}$ threshold relative to the low-frequency gain.

Excitation signals were designed as crested multisines. A multisine concentrates power at a discrete set of frequencies, avoiding spectral leakage by ensuring an integer number of periods fits within the observation window. Cresting reduces amplitude peaks and maximizes power per frequency for a given amplitude constraint [34]. Each run excited a defined

Fig. 5: The MaRCHMan transmission prototype in both test configurations. *Left:* Square Configuration ($9\,\mathrm{m}$ total, ten $90°$ bends). *Right:* Straight-Line Configuration ($7.5\,\mathrm{m}$ total, no bends), with corner joints replaced by coupler shafts of equal mass.

frequency band; successive runs covered progressively higher bands until the full frequency range of interest was measured. The signal was repeated twelve times within each measurement window, resulting in a total signal duration of $24\,\mathrm{s}$ per run. Rather than treating the commanded force signal as the system input directly, the resulting motion at the transmission input shaft was measured by sensor 0 and used as the true system input, as illustrated in Figure 8. The approach accounts for the unknown dynamics between the applied force and the resulting shaft motion, including actuator dynamics and mechanical compliance at the coupling interface. The transmission output was measured simultaneously by sensor 1, mounted at the distal end of the transmission. Both sensors were sampled by an Arduino at $200\,\mathrm{Hz}$. Despiking was applied when a sensor produced angular velocity values exceeding $2000\,°/\mathrm{s}$, which were deemed physically unrealistic given the transmission geometry. Points where the velocity exceeded the threshold were deleted from the measurement after which the points were replaced with interpolated values. All signal parameters and per-run despiking decisions are documented in Appendix B.

The power spectral density (PSD) of the sensor 0 signal was computed to show which frequencies received sufficient excitation energy, as shown schematically in Figure 8. Clock synchronization between the Arduino and Proprio was not available, meaning power peaks may not land exactly on the designed frequencies, risking unreliable FRF estimates. Therefore, a peak-finding approach was used to identify the excited frequencies from the sensor 0 signal. The peak-finder identifies the frequencies where excitation energy actually landed, ensuring only well-excited frequencies are carried forward into the FRF computation. The full-signal FFT of sensor 0 was computed for each measurement run. Within the user-defined frequency band of each run, local maxima were identified using a prominence-based criterion: a candidate peak was accepted only if its amplitude stood at least P_{min} dB above the local baseline relative to the band maximum, where P_{min} was set per run in the range $15\,\mathrm{dB}$ to $50\,\mathrm{dB}$ depending on the signal-to-noise ratio of the excitation. A minimum inter-peak spacing of $0.3\,\mathrm{Hz}$ to $0.4\,\mathrm{Hz}$ was enforced to prevent detection of closely-spaced peaks. The prominence and inter-peak spacing values were found empirically per run. The per-run values are documented in Appendix B.

The frequency response function (FRF) was computed at the identified peak frequencies as

$$H(f) = \frac{S_{x_1 x_0}(f)}{S_{x_0 x_0}(f)} \tag{11}$$

where $S_{x_0 x_0}$ is the auto-power spectrum of the input position (sensor 0) and $S_{x_1 x_0}$ is the cross-power spectrum between output (sensor 1) and input, both estimated using Welch's method [35] with a Hann window of 1024 samples and 50% overlap.

Coherence between sensor 0 and sensor 1 was computed alongside the FRF as a quality indicator, defined as

Fig. 6: 3D-printed bearing housing supporting the torsion rod. The housing is fastened to the aluminum extrusion frame with steel bolts.

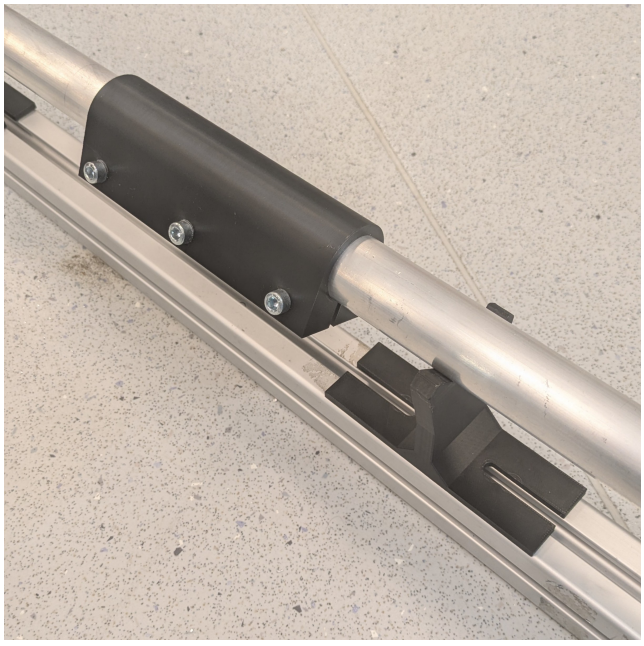

Fig. 7: Shaft coupler (left) clamping two torsion rod ends with M6 bolts, and sliding support bracket (right) preventing sagging of the $6\,\mathrm{m}$ torsion rod. The support bracket uses plain contact without rolling elements.

$$\gamma^2(f) = \frac{|S_{x_1x_0}(f)|^2}{S_{x_0x_0}(f)\,S_{x_1x_1}(f)} \tag{12}$$

where $\gamma^2 \in [0, 1]$, with values approaching one indicating a linear, noise-free relationship between input and output at that frequency. Frequencies where coherence fell below 0.8 were excluded from bandwidth interpretation.

Finally, a single degree-of-freedom mass-spring-damper model was fitted to the measured FRF. The model transfer function is

$$H(\omega) = \frac{K\omega_n^2}{\omega_n^2 - \omega^2 + 2j\zeta\omega_n\omega} \tag{13}$$

Parameters ω_n, ζ, and K were identified by minimizing a coherence-weighted, frequency-weighted logarithmic cost function [34]:

$$V(\boldsymbol{\theta}) = \sum_f \frac{\gamma^2(f)}{f} \left| \ln \frac{H_{\mathrm{meas}}(f)}{H_{\mathrm{mod}}(f, \boldsymbol{\theta})} \right|^2 \tag{14}$$

The logarithmic ratio reduces emphasis on high-magnitude frequencies, frequency weighting compensates for the unequal density of points on a logarithmic frequency axis, and coherence weighting reduces the contribution of frequencies estimated with lower reliability [34]. The natural frequency ω_n was initialized at the frequency of maximum FRF magnitude.

2) Stiffness Measurement: The torsional stiffness of the transmission was measured statically for both the Square Configuration and the Straight-Line Configuration. The output shaft (sensor 1 side) was loaded with known hanging weights at a moment arm of $75\,\mathrm{mm}$, while the input shaft (sensor 0 side) was rigidly blocked. Six load steps were applied: $0.625\,\mathrm{kg}$, $1.102\,\mathrm{kg}$, $1.584\,\mathrm{kg}$, $2.066\,\mathrm{kg}$, $2.362\,\mathrm{kg}$, and $2.844\,\mathrm{kg}$. At each step, the angular deflection at both sensor 0 and sensor 1 was recorded.

The applied torque at each load step was computed as

$$\tau = m\,g\,r_{\mathrm{eff}} \tag{15}$$

where m is the applied mass, $g = 9.81\,\mathrm{m/s^2}$ is the gravitational acceleration, and $r_{\mathrm{eff}} = r\cos(\theta)$ is the effective moment arm corrected for the deflection angle θ measured at sensor 0. The correction accounts for the reduction in horizontal moment arm as the crank rotates, though deflection angles remained small across all load steps, making the correction minor in practice.

Torsional stiffness was computed at each load step as

$$k = \frac{\tau}{\Delta\theta} \tag{16}$$

where $\Delta\theta = \theta_1 - \theta_0$ is the angular deflection between input and output, with θ_0 and θ_1 the angles recorded by sensor 0 and sensor 1 respectively. The stiffness reported is the mean across all load steps.

3) Additional Requirement Measurements: The range of motion of the transmission was assessed by rotating the input handle from one mechanical endstop to the other. Backlash was measured by blocking the output of the transmission, and rotating the input by hand back and forth. The change in relative angle was measured. Static friction was measured by applying incremental hanging weights at the $75\,\mathrm{mm}$ crank arm, analogous to the stiffness measurement procedure, until

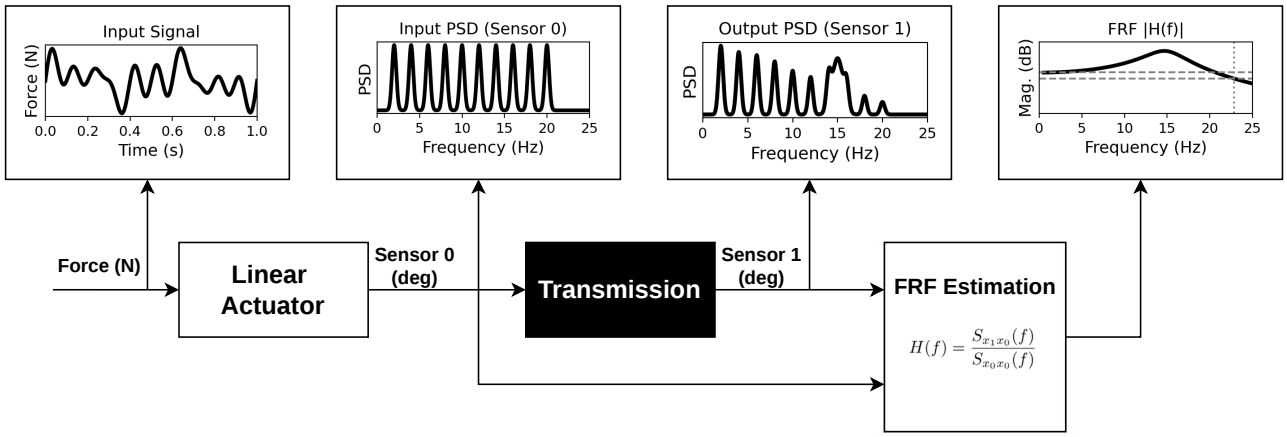

Fig. 8: Block diagram of the measurement chain. The Linear Actuator applies a force signal to the input shaft. Sensor 0 measures the resulting input motion, which is treated as the true system input. The power spectral density (PSD) is extracted from the Sensor 0 signal. The MaRCHMan transmission is the system under test. Sensor 1 measures the output motion. The PSD is extracted from the Sensor 1 signal. The frequency response function (FRF) is found through comparing the PSDs from both sensor signals. The transfer function is found with equation 11.

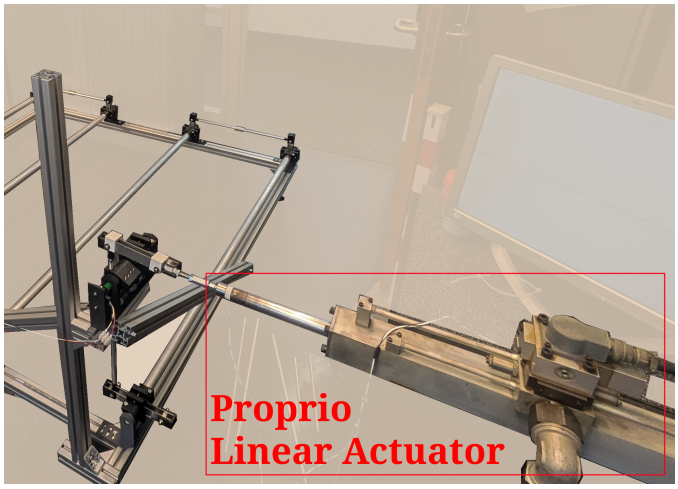

Fig. 9: The Square Configuration coupled to the Proprio hydraulic actuator via a slider crank mechanism.

the transmission began to move. The corresponding torque at the onset of motion was taken as the static friction torque.

V. Results B

A. Representative Bandwidth Measurement

A representative measurement from the Square Configuration is shown here to illustrate the measurement chain. The combined input spectra for all runs used in the Square Configuration are shown in Figure 10, demonstrating continuous excitation coverage from $0.5\,\mathrm{Hz}$ to $20\,\mathrm{Hz}$ with no gaps.

The time-domain angle signals recorded by sensor 0 (input) and sensor 1 (output) for a representative run are shown in Figure 11. The two signals overlap closely throughout the steady-state excitation interval. Two large transient spikes are visible at $t \approx 3\,\mathrm{s}$ and $t \approx 21\,\mathrm{s}$, corresponding to actuator startup and switch-off.

The frequency content of the measured input signal was observed to have shifted upward from the designed excitation frequencies. For the representative run, the designed band of $12\,\mathrm{Hz}$ to $15\,\mathrm{Hz}$ shifted to approximately $14.5\,\mathrm{Hz}$ to $19\,\mathrm{Hz}$. The shift was consistent across all runs and is discussed in Section VI.

The PSD of sensor 0 with detected peaks is shown in Figure 12, and the resulting FRF is shown in Figure 13. Coherence at the selected frequencies exceeds $\gamma^2 = 0.9$ in all cases.

1) Square Configuration, Combined FRF: Figure 14 shows the combined FRF for both configurations. For the Square Configuration, the fit (13) identifies a resonance frequency of $f_{\mathrm{res}} = 15.0\,\mathrm{Hz}$ and predicts a $-3\,\mathrm{dB}$ bandwidth of $24.1\,\mathrm{Hz}$. The resonance peak is visible in the measured data, and the FRF fit follows the measured points closely through the resonance and into the rolloff region. Above resonance, the magnitude decreases at approximately $-40\,\mathrm{dB}$ per decade. Coherence exceeds 0.8 at all measured frequencies.

2) Straight-Line Configuration, Combined FRF: The Straight-Line Configuration FRF is also shown in Figure 14. The fit identifies a resonance at $f_{\mathrm{res}} = 27.5\,\mathrm{Hz}$ and extrapolates a $-3\,\mathrm{dB}$ bandwidth of $46.9\,\mathrm{Hz}$. The $-3\,\mathrm{dB}$ crossing lies beyond $35\,\mathrm{Hz}$, above which coherence drops below 0.8. The reported bandwidth is therefore a model extrapolation rather than a directly measured value.

B. Stiffness Measurement

Figure 15 shows the measured torque as a function of angular deflection for both configurations. The torque-deflection relationship is highly linear across all load steps for both configurations. The Square Configuration yields a torsional stiffness of $k_A = 14.5\,\mathrm{N\,m/rad}$ ($R^2 = 0.997$) and the Straight-Line Configuration yields $k_B = 48.5\,\mathrm{N\,m/rad}$ ($R^2 = 1.000$). Both configurations transmitted the maximum applied torque of $2.1\,\mathrm{N\,m}$ without evidence of nonlinearity, exceeding

the $1.2\,\mathrm{N\,m}$ torque requirement. During the measurement, the bearing housings were observed to both bend in-plane and deflect out-of-plane. The significance of this observation is quantified in the analytical model below and discussed in Section VI.

C. Additional Requirements

A range of motion of $[-42°, 42°]$ was observed, exceeding the $[-40°, 40°]$ requirement. No backlash was observed in either configuration across any measurement run. The Square Configuration yielded a static friction torque of $0.070\,\mathrm{N\,m}$. With 10 joints, the Square Configuration has a static friction torque of $0.007\,\mathrm{N\,m}$ per joint. The Straight-Line Configuration yielded $0.134\,\mathrm{N\,m}$ with 4 joints, resulting in a static friction torque of $0.0335\,\mathrm{N\,m}$ per joint. The Square Configuration meets the $0.0225\,\mathrm{N\,m}$ per joint requirement; the Straight-Line Configuration does not.

D. Analytical Stiffness Model

All data required to reproduce the results calculated in this section are included in Appendix A.

1) Reflected Mass: The reflected mass was estimated from the measured resonance frequency and stiffness for each configuration using equation 6. For the Square Configuration: $m_{\text{refl,A}} = 0.291\,\mathrm{kg}$. For the Straight-Line Configuration: $m_{\text{refl,B}} = 0.289\,\mathrm{kg}$. The reflected mass is nearly identical across both configurations. The analytical reflected mass estimate from the model gives $m_{\text{refl,A}} = 0.417\,\mathrm{kg}$ and $m_{\text{refl,B}} = 0.302\,\mathrm{kg}$, both higher than the measurement-derived values. The discrepancy and the difference between configurations in the analytical estimate are discussed in Section VI.

2) Series Compliance Model: The series compliance model described in Section II was applied to both configurations using the prototype geometry and material properties. Joint compliance is included. Table III shows the predicted stiffness and the fractional compliance contribution of each component.

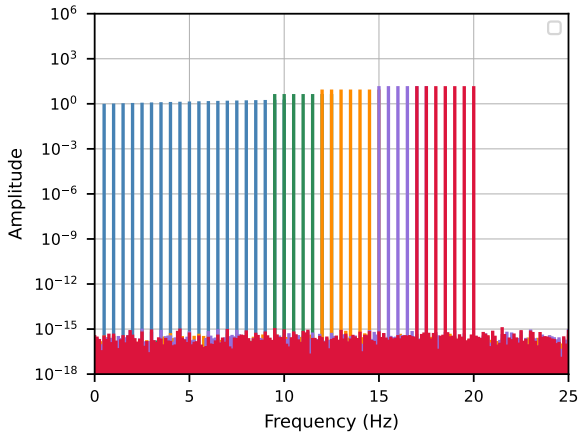

Fig. 10: Combined input spectra for all runs contributing to the Square Configuration FRF. Each color represents one measurement run. Together the runs provide continuous coverage from $0.5\,\mathrm{Hz}$ to $20\,\mathrm{Hz}$.

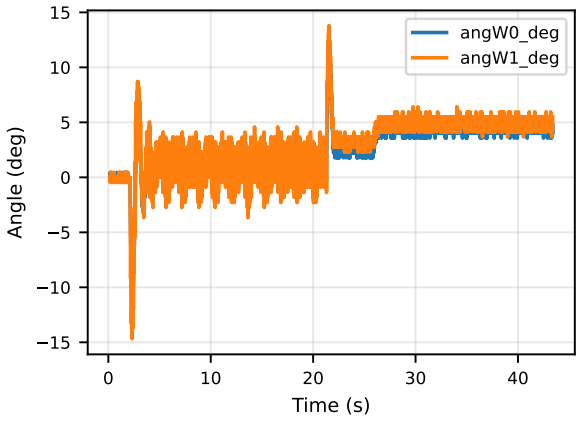

Fig. 11: Time-domain angle signals for a representative run ($12\,\mathrm{Hz}$ to $15\,\mathrm{Hz}$ band, Square Configuration). Sensor 0 (input, blue) and sensor 1 (output, orange) overlap closely. Transient spikes at $t \approx 3\,\mathrm{s}$ and $t \approx 21\,\mathrm{s}$ correspond to actuator startup and switch-off.

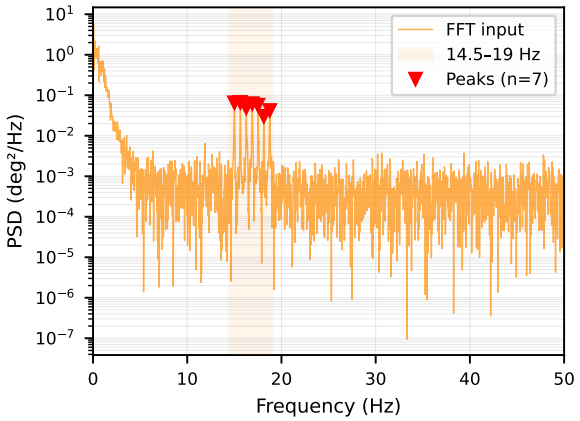

Fig. 12: PSD of sensor 0 for a representative run, with detected peaks marked. Peaks were identified using the prominence-based method described in Section IV and carried forward into the FRF computation.

The model predicts $38.1\,\mathrm{N\,m/rad}$ for the Square Configuration and $62.9\,\mathrm{N\,m/rad}$ for the Straight-Line Configuration. The discrepancy between measurement and the modeled result is discussed in Section VI.

3) Predicted Resonance Frequency: Using the predicted stiffness and reflected mass values, the resonance frequency was estimated for both configurations with equation (7). The results are shown in Table V.

VI. Discussion

A. Requirements Check

Most proof-of-concept requirements were met by both configurations. The control bandwidth exceeded $20\,\mathrm{Hz}$ in both cases: the Square Configuration achieved a $-3\,\mathrm{dB}$ bandwidth of $24.1\,\mathrm{Hz}$ and the Straight-Line Configuration an extrapolated bandwidth of $46.9\,\mathrm{Hz}$. Both configurations transmitted the

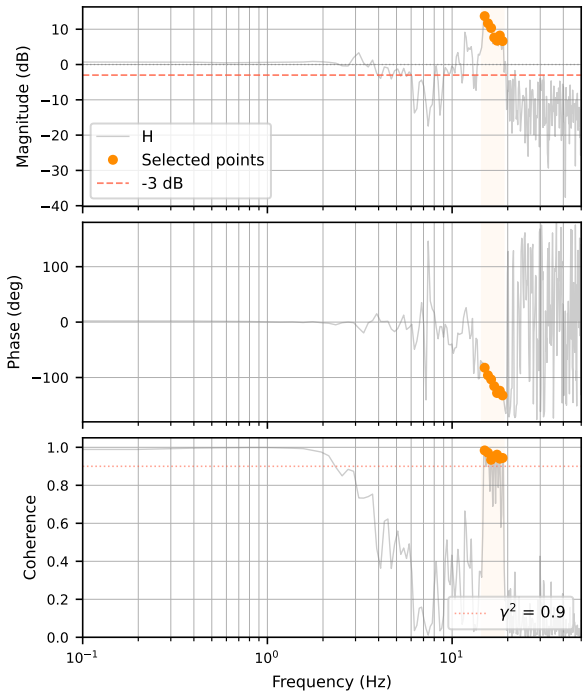

Fig. 13: FRF of a representative run (12 Hz to 15 Hz band, Square Configuration). The full FRF estimate (gray) is shown alongside selected peak frequencies (orange dots) with coherence $\gamma^2 > 0.9$. Coherence drops outside the excited band as expected.

TABLE III: Compliance breakdown for both configurations. Contributions expressed as percentage of total predicted compliance. Bearing housing includes in-plane bending only; out-of-plane effects are discussed in Section VI.

Component	Square (%)	Straight (%)
Torsion rod	45.3	74.8
Bearing housings	36.3	12.0
Crank plates	10.2	6.7
Rod ends	0.5	0.3
Clamps	6.6	4.4
Pushrods	1.0	0.8
Couplers	N/A	0.9
Predicted k (N m/rad)	38.1	63.0
Measured k (N m/rad)	14.5	48.5

maximum applied torque of $2.1\,\mathrm{N\,m}$ without nonlinearity, exceeding the $1.2\,\mathrm{N\,m}$ requirement. The range of motion of $[-42°, 42°]$ exceeds the $[-40°, 40°]$ requirement. No backlash was observed in either configuration. Static friction exceeded the $0.0225\,\mathrm{N\,m}$ per joint limit for the Straight-Line Configuration and is discussed in Section VI-C4. The MaRCHMan prototype therefore demonstrates that the torsion-pushrod concept is mechanically viable. Additional development is needed before the concept can be realized as a fully MR-Conditional system deployable in a clinical environment.

TABLE IV: Reflected mass breakdown for both configurations. Contributions expressed as percentage of total predicted reflected mass.

Component	Square (%)	Straight (%)
Torsion rod (I/3)	5.0	6.8
Pushrod Assemblies (I/3)	58.4	39.7
Handle	0.6	0.9
Output Rod	36.0	49.6
Couplers (I/3)	N/A	3.0
Predicted m_{refl} (kg)	0.417	0.302
Measured m_{refl} (kg)	0.291	0.289

TABLE V: Summary of predicted and measured transmission performance for both configurations. f_n was predicted with the predicted m_{refl}.

	Square		Straight	
	Predicted	Measured	Predicted	Measured
k (N m/rad)	38.1	14.5	63.0	48.5
m_{refl} (kg)	0.417	0.291	0.302	0.289
f_n (Hz)	20.3	15.0	30.6	27.5
Bandwidth (Hz)	—	24.1	—	46.9*

*Model extrapolation.

B. Performance Bottleneck Analysis

1) Resonance Frequency as Design Target: The reported $-3\,\mathrm{dB}$ bandwidth is the standard control systems definition, measured relative to the low-frequency gain, but it is not the most informative metric for transmission design. The resonance frequency is a more natural design target: it can be estimated analytically before a prototype is built, it directly indicates where the transmission begins to behave dynamically, and pushing it above the frequency range of interest eliminates the resonance peak from the operating range entirely. The resonance peak visible in the Square Configuration FRF exceeds $10\,\mathrm{dB}$, which would be problematic for position control without active damping or compensation. The design recommendations in this section are therefore framed in terms of resonance frequency rather than $-3\,\mathrm{dB}$ bandwidth.

2) Compliance Model vs Measurement: The series compliance model presented in Section V-D predicted a Square Configuration stiffness of $38.1\,\mathrm{N\,m/rad}$ and a Straight-Line stiffness of $62.9\,\mathrm{N\,m/rad}$. The measured values are $14.5\,\mathrm{N\,m/rad}$ and $48.5\,\mathrm{N\,m/rad}$ respectively. The Straight-Line prediction is within $30\,\%$ of the measurement, indicating the model captures the dominant compliance sources adequately for the configuration without corner joints. The Square prediction is $163\,\%$ higher than measured, indicating a significant unmodeled compliance source that scales with joint count.

The compliance breakdown in Table III confirms that

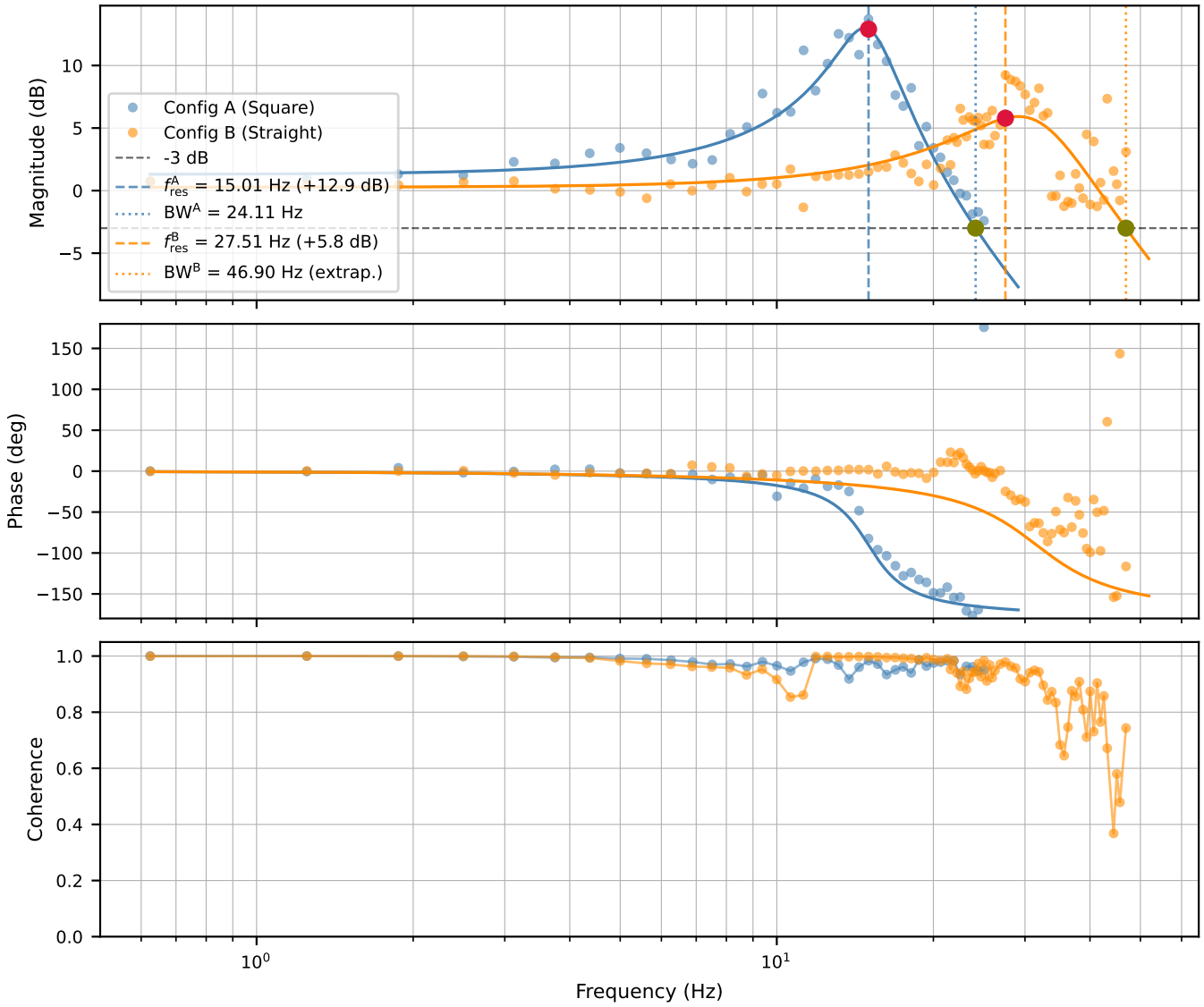

Fig. 14: Combined FRF of both configurations. *Top to bottom:* magnitude (dB), phase (deg), coherence. *Square Configuration* (9 m total, ten 90° bends), assembled from five measurement runs: resonance at $f_{\text{res}} = 15.0\,\text{Hz}$, $-3\,\text{dB}$ bandwidth of 24.1 Hz; magnitude rolloff follows the expected $-40\,\text{dB}$ per decade second-order slope; coherence exceeds 0.8 at all measured frequencies. *Straight-Line Configuration* (7.5 m total, no bends), assembled from twelve measurement runs: resonance at $f_{\text{res}} = 27.5\,\text{Hz}$, extrapolated $-3\,\text{dB}$ bandwidth of 46.9 Hz; coherence exceeds 0.8 up to approximately 35 Hz.

bearing housing compliance is the largest single contributor in both configurations. However, the in-plane model alone cannot account for the discrepancy. The bearing housing can also deflect out-of-plane relative to the crank rotation plane. The out-of-plane direction is governed by the weaker cross-sectional axis, with stiffness reduced by a factor $(h_{\text{oop}}/h_{\text{ip}})^3$ relative to the in-plane value. For the current housing geometry this ratio is $(12.5/40)^3 \approx 0.030$, meaning the out-of-plane stiffness is approximately 33 times lower than the in-plane stiffness. Out-of-plane deflection arises from any misalignment between the pushrod axis and the crank rotation plane, which cannot be eliminated entirely in a hand-assembled prototype.

The total compliance of a bearing housing subject to both in-plane and out-of-plane loading is:

$$C_{\text{holder,total}} = (1-\alpha)\,C_{\text{holder,ip}} + \alpha\,C_{\text{holder,oop}} \tag{17}$$

where $\alpha \in [0,1]$ is the fraction of the pushrod force acting out of plane due to assembly misalignment. At $\alpha = 0.30$, the predicted Square stiffness drops to $19.0\,\text{N m/rad}$, nearing the measured $14.5\,\text{N m/rad}$. For the Straight-Line Configuration, the same value of α gives $50.1\,\text{N m/rad}$, consistent with the measured $48.5\,\text{N m/rad}$. Out-of-plane bearing housing deflection therefore accounts for the discrepancy between the in-plane model and the measured stiffness in both configurations.

The parameter α was not measured directly and was instead back-calculated from the measurement. Direct measurement of the pushrod misalignment angle at each joint is recommended

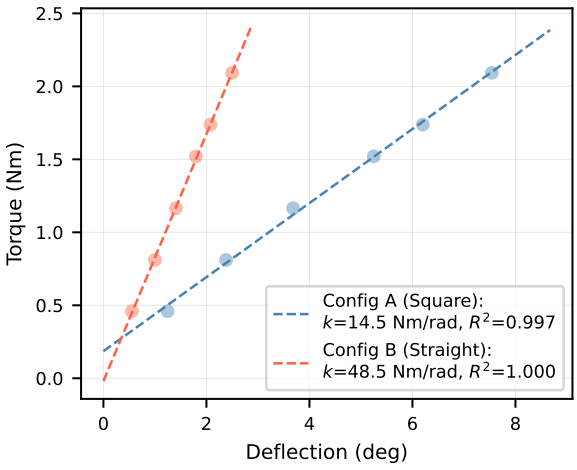

Fig. 15: Torsional stiffness measurement results for both configurations. A linear fit gives the Square Configuration $k_A = 14.5\,\mathrm{N\,m/rad}$ with $R^2 = 0.997$, and the Straight-Line Configuration $k_B = 48.5\,\mathrm{N\,m/rad}$ with $R^2 = 1.000$.

as a next step, as it would allow the compliance model to be used predictively rather than retrospectively.

3) Improvement Paths: The primary recommendation is to replace the 3D-printed PLA bearing housings with machined aluminum or to mount bearings onto the stiff frame. PLA has an elastic modulus approximately 20 times lower than aluminum, and the 3D-printed geometry produces the dominant compliance contribution identified above. Stiffer housings would reduce both the in-plane and out-of-plane compliance simultaneously. Based on the compliance breakdown, eliminating housing compliance entirely would raise the predicted Square stiffness to approximately $59.9\,\mathrm{N\,m/rad}$, giving a resonance frequency of approximately $30.5\,\mathrm{Hz}$, well above the $20\,\mathrm{Hz}$ target.

A secondary option is reduction of the crank radius. The resonance frequency scales as $f_n \propto 1/r_{\text{crank}}$, since reflected inertia scales as $m_{\text{refl}} \cdot r_{\text{crank}}^2$ while torsional stiffness of the rods is independent of crank radius. The minimum crank radius that still satisfies the $\pm 40°$ range of motion requirement is:

$$r_{\text{min}} = \frac{r_{\text{torsion}} + r_{\text{pushrod}}}{\sin(\theta_{\text{RoM}})} \tag{18}$$

where $r_{\text{torsion}} = 15\,\mathrm{mm}$, $r_{\text{pushrod}} = 5\,\mathrm{mm}$, and $\theta_{\text{RoM}} = 40°$, giving $r_{\text{min}} \approx 31\,\mathrm{mm}$. The current endcap design limits range of motion to approximately $\pm 42°$, well below the geometric maximum of $\pm 74°$ permitted by the $75\,\mathrm{mm}$ crank. Redesigning the endcap would allow the crank radius to be reduced to $31\,\mathrm{mm}$ while maintaining the range of motion requirement, raising the resonance frequency by a factor of $75/31 \approx 2.4$ through inertia reduction alone. However, crank radius reduction is only advisable after housing stiffness has been improved: if housing compliance dominates, reducing the crank radius makes the housing compliance relatively worse, since the housing compliance contribution scales as $1/r_{\text{crank}}^2$.

It should also be noted that the measurement of transmission stiffness between a free input and blocked output is not fully representative of operation with a damped human hand load. In practice, the hand presents a significant impedance at the end-effector, which would damp the resonance and shift the resonance frequency downward while reducing the peak magnitude [9, 28].

C. Design Limitations

1) Torsion Rod Diameter Selection: The torsion rod outer diameter of $30\,\mathrm{mm}$ was selected by estimating the resonance frequency of a pure torsion rod and verifying it exceeded $20\,\mathrm{Hz}$. In that estimate, the crank radius was incorrectly assumed equal to the rod outer radius, i.e. $r_{\text{crank}} = r_{\text{rod}} = 15\,\mathrm{mm}$. The actual crank radius is $75\,\mathrm{mm}$.

TABLE VI: Effect of crank radius assumption on estimated resonance frequency for a $30\,\mathrm{mm}$ aluminum torsion rod over $9\,\mathrm{m}$.

r_{crank}	$15\,\mathrm{mm}$	$75\,\mathrm{mm}$
m_{refl} (kg)	2.217	0.229
f_n (Hz)	55	34

Table VI illustrates the consequence of the incorrect assumption. Using the actual crank radius of $75\,\mathrm{mm}$ reduces the estimated resonance frequency from $55\,\mathrm{Hz}$ to $34\,\mathrm{Hz}$, a factor of 1.6. Both values still exceed the $20\,\mathrm{Hz}$ requirement for a pure torsion rod without joint compliance, so the incorrect assumption did not invalidate the feasibility check. However, it produced an overly optimistic baseline: once joint compliance is included in the assembled prototype, the resonance drops to $15.0\,\mathrm{Hz}$ in the Square Configuration, revealing that the available margin was much smaller than the initial estimate suggested.

2) Stiffness Estimation Timing: The series compliance model was constructed retrospectively, after prototype fabrication and measurement. Had this model been applied before the final prototype iteration, the bearing housing compliance would have been identified as the dominant bottleneck before the validation experiments were conducted on the final prototype. Replacing the 3D-printed housings with stiffer alternatives would have been straightforward at that stage. For the next design iteration, performing the compliance analysis before fabrication is strongly recommended.

3) Reflected Mass Model: The analytical reflected mass estimate differs from the measurement-derived value for both configurations. The measurement-derived reflected mass is approximately $290\,\mathrm{g}$ for both configurations, while the analytical model gives $417\,\mathrm{g}$ for the Square and $302\,\mathrm{g}$ for the Straight-Line. Two sources of uncertainty contribute to this discrepancy.

The first is the effective radius of each mass component. Pushrod assemblies were modeled as point masses at the crank radius, but each assembly consists of the tube, rod ends, axles, slide bearings, endcaps, and couplers, each at a slightly different effective radius. Lumping all of this mass at the crank tip may have overestimated the inertial contribution of components that sit closer to the rotation axis.

The second is the placement of the distributed-to-point-mass boundary in the $I/3$ approximation. The approximation divides the system into a distributed chain contributing $I/3$, and a concentrated final stage contributing its full inertia. In this model the boundary was placed at the output crank, with the output pushrod and handle treated as the final point mass. Because the output pushrod is a stiff element with minimal compliance contribution, including it in the final stage produced the best agreement with the measurement-derived value. However, the correct boundary placement is not uniquely defined for a non-uniform chain of elements, and a different choice would shift the predicted reflected mass.

The measurement-derived value is the more reliable of the two, since it is derived directly from the measured stiffness and resonance frequency rather than from geometric estimates. The analytical model is best understood as a design tool for comparing configurations and identifying dominant contributors, not as a precise predictor of absolute inertia. Direct characterization of each component's inertia contribution is recommended to resolve the discrepancy in a future iteration.

4) Static Friction: The Square Configuration met the static friction requirement with $0.007\,\mathrm{N\,m}$ per joint, below the $0.0225\,\mathrm{N\,m}$ limit. For the Square Configuration, the igus rod ends were the primary friction source. Rod ends vary considerably in friction between the ball and housing, and it is recommended to screen rod ends before assembly in future designs.

The Straight-Line Configuration did not meet the requirement, yielding $0.0335\,\mathrm{N\,m}$ per joint. The elevated friction was caused by sliding contact between the $6\,\mathrm{m}$ torsion rod and the 3D-printed support brackets, which lack rolling elements. Replacing the sliding support brackets with rolling contact bearings is recommended to reduce friction and prevent wear.

D. Applicability of the Current Transmission

To illustrate the applicability of the transmission to the intended research context, consider the protocol of Vlaar et al., in which continuous periodic wrist disturbances were applied to stroke patients during EEG recording to quantify somatosensory cortical responses [7]. The disturbance signal was a multisine spanning $0.8\,\mathrm{Hz}$ to $19.2\,\mathrm{Hz}$ with an amplitude of $0.02\,\mathrm{rad}$ $(1.15°)$ RMS. Both developed configurations exceed the $20\,\mathrm{Hz}$ bandwidth required to transmit such a signal, and the small disturbance amplitude lies within the linear operating range confirmed by the stiffness measurements.

The Vlaar protocol applies position-controlled disturbances. Transmission compliance introduces a small angular difference between input and output but does not distort the motion delivered to the wrist; it requires only that the actuator exert additional force to deflect the compliant transmission before the output moves. At the highest excited frequency of $19.2\,\mathrm{Hz}$, the peak inertial torque demand is:

$$\tau = m_{\text{refl}} \cdot r_{\text{crank}}^2 \cdot \omega^2 \cdot \hat{\theta} \tag{19}$$

where $m_{\text{refl}} = 0.29\,\mathrm{kg}$, $r_{\text{crank}} = 0.075\,\mathrm{m}$, $\omega = 2\pi \times 19.2\,\mathrm{rad/s}$, and $\hat{\theta} = 0.02\,\mathrm{rad}$. Evaluating gives $\tau \approx 0.047\,\mathrm{N\,m}$. The resulting angular deflection is $\Delta\theta = \tau/k$, giving:

$$\Delta\theta_A = \frac{0.047\,\mathrm{N\,m}}{14.5\,\mathrm{N\,m/rad}} \approx 0.003\,\mathrm{rad} \tag{20}$$

corresponding to approximately $15\,\%$ of the disturbance amplitude. For the Straight-Line Configuration, the higher stiffness reduces the deflection to $\Delta\theta_B \approx 0.001\,\mathrm{rad}$, or less than $5\,\%$. Both values are small relative to the disturbance amplitude and can be further reduced by compensating the known static deflection in the commanded input angle. The MaRCHMan transmission is therefore mechanically compatible with the Vlaar protocol and represents a viable path toward combined EEG and fMRI experiments in a single MR-Conditional setup.

E. MR-Conditionality: Required Substitutions and Expected Performance Impact

The current prototype contains several components incompatible with MR-Conditional operation. The steel bolts clamping the joint plates onto the torsion tubes, and the steel T-slot nuts fastening the bracket assemblies to the frame, are the primary deviations. Replacing steel bolts with nylon or titanium alternatives is straightforward. Nylon fasteners are fully non-magnetic and lightweight but have lower shear and tensile strength than steel. Titanium fasteners match steel in strength while remaining non-magnetic, at higher cost. The T-slot nut requires a purpose-designed clamping mechanism, as non-magnetic drop-in replacements are not commercially standard.

The steel roller bearings supporting the torsion rods carry only radial load during normal operation. Substituting ceramic or polymer rolling-contact bearings of equivalent geometry is not expected to meaningfully affect static friction, as the bearing contact is not the dominant friction source in the current prototype.

MR-Conditionality does not require the complete absence of metal. As confirmed during a site visit to Amsterdam Universitair Medisch Centrum, steel components are acceptable in the MRI room provided they are not within the exclusion zone around the bore. Actuator-side components that remain in the control room could retain steel fasteners and bearings without issue. Only components entering the scanner room, and particularly those near the bore, require non-magnetic substitution. Involving an MRI technical specialist early in the next design iteration is strongly recommended.

F. Methods Limitations

1) Clock Synchronization and Frequency Shifting: The multisine excitation signal was generated in MATLAB at a design sample rate of $250\,\mathrm{Hz}$ and transmitted to the Proprio as a raw sample vector without an explicit time axis. The Proprio operates at an internal playback rate of $312.5\,\mathrm{Hz}$, causing the signal to play back at a rate $312.5/250 = 1.25$ times higher than intended. All excitation frequencies were therefore shifted upward by a factor of 1.25, and the $24\,\mathrm{s}$ signal completed playback in approximately $19\,\mathrm{s}$. This was confirmed by generating an equivalent signal at $312.5\,\mathrm{Hz}$, which played back at the intended duration. Because the excited frequencies were

identified with the peak-finding approach from the sensor 0 signal rather than from the designed frequency vector, the frequency shift does not affect the validity of the FRF estimate. For future work, matched sample rates between signal generation and actuator playback are recommended, alongside synchronization of the Arduino clock with the actuator control system.

2) FRF Fit and Bandwidth Estimation: A single degree-of-freedom mass-spring-damper model was fitted to the combined FRF of both configurations. For the Square Configuration the fit is well-supported: the resonance peak and the onset of $-40\,\mathrm{dB/decade}$ rolloff are clearly visible within the measured range, and the $-3\,\mathrm{dB}$ crossing is approached but not fully reached. The reported bandwidth of $24.1\,\mathrm{Hz}$ is a short model extrapolation supported by the fit. For the Straight-Line Configuration the $-3\,\mathrm{dB}$ crossing lies well beyond the measured range, in a region where coherence drops below 0.8. The reported bandwidth of $46.9\,\mathrm{Hz}$ is a model extrapolation and should be treated with caution. The conclusion that the Straight-Line Configuration maintains $0\,\mathrm{dB}$ gain over a substantially wider frequency range than the Square Configuration is supported directly by the measured data and is independent of the fit.

G. Modularity and MRI Room Integration

The current prototype is not modular; it was designed and assembled as a single integrated structure for validation purposes. A transmission for clinical or research use must be modular for two reasons: MRI rooms are typically fully booked during research sessions, leaving little time for setup and teardown, and the transmission cannot remain permanently installed between sessions. A modular design consisting of discrete torsion stages and pushrod stages connected via a quick-release mechanism would allow assembly, use, and disassembly within a single session without tools. Each torsion stage should clamp to a rigid surface in the scanner room; the rigidity of the mounting points is as important as the stiffness of the moving components, as any compliance in the support structure appears in series with the transmission stiffness.

The MRI patient bed introduces an additional integration challenge. The bed slides into the bore with the patient, so any transmission component attached to the bed must either move with it or disconnect and reconnect after positioning. A practical solution is a final connection stage inserted after patient positioning: a pushrod stage with a tool-free quick-release at one end, locked in place once the bed is in its final position. Safety considerations for emergency patient removal must be addressed in the mechanical design of this connection: the quick-release must allow rapid disconnection without tools.

VII. Conclusions

This paper presented the design and experimental validation of the MaRCHMan, a torsion-pushrod transmission for MR-Conditional haptic manipulation. The prototype is a proof-of-concept for a transmission system that is a strong basis for any future MR-Conditional haptic manipulator capable of supporting combined EEG-fMRI motor control research.

The transmission employs alternating torsion rods and pushrods to transmit motion and force mechanically from outside the MRI room into the scanner bore over a distance of $9\,\mathrm{m}$. Two configurations were validated: the Square Configuration, incorporating ten 90° bends, and the Straight-Line Configuration, without corner joints. Most proof-of-concept requirements were satisfied by both configurations: a control bandwidth exceeding $20\,\mathrm{Hz}$, torque transmission of at least $1.2\,\mathrm{N\,m}$, a range of motion of $[-42^\circ, 42^\circ]$, and no observable backlash. Static friction exceeded the requirement in the Straight-Line Configuration, caused by sliding contact between the $6\,\mathrm{m}$ torsion rod and the 3D-printed support brackets.

Comparing the two configurations revealed that the Square Configuration is approximately 3 times less stiff than the Straight-Line Configuration despite similar reflected mass, confirming that the bandwidth difference is driven by stiffness rather than inertia. A series compliance model identified the 3D-printed bearing housings as the dominant compliance source. The in-plane model predicted $38.1\,\mathrm{N\,m/rad}$ for the Square Configuration; including out-of-plane bearing housing deflection at a misalignment fraction of $\alpha = 0.3$ reduces the prediction to $19.0\,\mathrm{N\,m/rad}$, approaching the measured $14.5\,\mathrm{N\,m/rad}$. Pushrod axial stiffness is approximately three orders of magnitude higher than bearing housing compliance and does not contribute meaningfully to the bottleneck.

The primary recommendation for the next iteration is to replace the 3D-printed PLA bearing housings with stiffer alternatives, like pillow block bearings or mounting bearings directly onto the stiff aluminum frame. Eliminating housing compliance is predicted to raise the Square Configuration resonance frequency from $15.0\,\mathrm{Hz}$ to approximately $31\,\mathrm{Hz}$. Crank radius reduction from $75\,\mathrm{mm}$ to $31\,\mathrm{mm}$ is a secondary option that further raises the resonance frequency through inertia reduction, but should only be pursued after housing stiffness has been addressed. The current prototype uses steel fasteners and bearings and has not been validated in an MRI environment. Steel components are acceptable outside the bore exclusion zone, so only the in-bore segment requires MR-Conditional substitution.

This work provides a validated transmission architecture, a quantified compliance model identifying the bearing housing as the primary bottleneck, and concrete design targets for the next iteration, bringing a complete MR-Conditional haptic manipulator one step closer to realization.

Acknowledgment

The author acknowledges the use of Claude (Anthropic) as an AI assistant during this thesis. Claude was used for generating Python code for plots, proofreading, and editorial improvement of written sections.

REFERENCES

[1] M. Bonanno, P. De Pasquale, B. Fonti, E. Gjonaj, S. De Salvo, A. Quartarone, and R. S. Calabrò, "Neural control meets biomechanics in the motor assessment of neurological disorders: a narrative review," *Frontiers in Neural Circuits*, vol. 19, p. 1608328, Jun. 2025. [Online]. Available: https://pmc.ncbi.nlm.nih.gov/articles/PMC12245779/

[2] D. M. Wolpert and M. Kawato, "Multiple paired forward and inverse models for motor control," *Neural Networks*, vol. 11, no. 7, pp. 1317–1329, Oct. 1998. [Online]. Available: https://www.sciencedirect.com/science/article/pii/S0893608098000665

[3] WHO, "Over 1 in 3 people affected by neurological conditions, the leading cause of illness and disability worldwide." [Online]. Available: https://www.who.int/news/item/14-03-2024-over-1-in-3-people-affected-by-neurological-conditions--the-leading-cause-of-illness-and-disability-worldwide

[4] M. P. Vlaar and A. C. Schouten, "System identification for human motion control," in *2015 IEEE International Instrumentation and Measurement Technology Conference (I2MTC) Proceedings*, May 2015, pp. 600–605. [Online]. Available: https://ieeexplore.ieee.org/document/7151336

[5] Y. Ma, W. Sun, N. Zhou, J. He, and C. Ma, "Neurons in Primary Motor Cortex Encode External Perturbations during an Orientation Reaching Task," *Brain Sciences*, vol. 11, no. 9, p. 1125, Aug. 2021. [Online]. Available: https://pmc.ncbi.nlm.nih.gov/articles/PMC8470506/

[6] D. Balderas, M. Rojas, D. Balderas, and M. Rojas, "Human Movement Control," in *Automation and Control Trends*. IntechOpen, Oct. 2016. [Online]. Available: https://www.intechopen.com/chapters/51207

[7] M. P. Vlaar, T. Solis-Escalante, J. P. A. Dewald, E. E. H. van Wegen, A. C. Schouten, G. Kwakkel, F. C. T. van der Helm, J. de Munck, C. Meskers, M. Saes, L. Haring, C. Winters, A. Andringa, D. Hoevenaars, I. de Castro Fernandes, S. Zandvliet, A. Daffertshofer, J. Yao, Y. Yang, M. van de Ruit, K. Kalogianni, L. Filatova, and on behalf of the 4D-EEG consortium, "Quantification of task-dependent cortical activation evoked by robotic continuous wrist joint manipulation in chronic hemiparetic stroke," *Journal of NeuroEngineering and Rehabilitation*, vol. 14, no. 1, p. 30, Apr. 2017. [Online]. Available: https://doi.org/10.1186/s12984-017-0240-3

[8] O'Malley, M. and Gupta, A., "Haptic Interfaces," 2008. [Online]. Available: https://www.researchgate.net/publication/279616558_Haptic_Interfaces

[9] S. Sharifi, F. Luft, L. de Boer, A. W. G. Buijink, W. Mugge, A. C. Schouten, T. Heida, L. J. Bour, and A. F. van Rootselaar, "Closing the loop: Novel quantitative fMRI approach for manipulation of the sensorimotor loop in tremor," *NeuroImage*, vol. 262, p. 119554, Nov. 2022. [Online]. Available: https://www.sciencedirect.com/science/article/pii/S1053811922006693

[10] D. Bode, W. Mugge, A. C. Schouten, A. F. Van Rootselaar, L. J. Bour, F. C. T. Van Der Helm, and P. Lammertse, "Design of a magnetic resonance-safe haptic wrist manipulator for movement disorder diagnostics," *Journal of Medical Devices, Transactions of the ASME*, vol. 11, no. 4, 2017, type: Journal Article.

[11] M. P. Vlaar, W. Mugge, P. F. C. Groot, S. Sharifi, L. J. Bour, F. C. T. van der Helm, A.-F. van Rootselaar, and A. C. Schouten, "Targeted brain activation using an MR-compatible wrist torque measurement device and isometric motor tasks during functional magnetic resonance imaging," *Magnetic Resonance Imaging*, vol. 34, no. 6, pp. 795–802, Jul. 2016. [Online]. Available: https://www.sciencedirect.com/science/article/pii/S0730725X16000217

[12] R. F. Ahmad, A. S. Malik, N. Kamel, and F. Reza, "EEG-fMRI combination for better understanding of brain functions: Pros and cons," in *2015 IEEE International Conference on Signal and Image Processing Applications (ICSIPA)*, Oct. 2015, pp. 278–281. [Online]. Available: https://ieeexplore.ieee.org/document/7412204

[13] E. Ebrahimzadeh, S. Saharkhiz, L. Rajabion, H. B. Oskouei, M. Seraji, F. Fayaz, S. Saliminia, S. M. Sadjadi, and H. Soltanian-Zadeh, "Simultaneous electroencephalography-functional magnetic resonance imaging for assessment of human brain function," *Frontiers in Systems Neuroscience*, vol. 16, Jul. 2022. [Online]. Available: https://www.frontiersin.org/journals/systems-neuroscience/articles/10.3389/fnsys.2022.934266/full

[14] Q. Xiao, R. Monfaredi, M. Musa, K. Cleary, and Y. Chen, "Mr-conditional actuations: A review," *Annals of Biomedical Engineering*, vol. 48, no. 12, pp. 2707–2733, 2020, export Date: 28 May 2025; Cited By: 26.

[15] ASTM, "Practice for Marking Medical Devices and Other Items for Safety in the Magnetic Resonance Environment," 2023. [Online]. Available: http://www.astm.org/cgi-bin/resolver.cgi?F2503-23E1

[16] F. Sergi, A. C. Erwin, and M. K. O'Malley, "Interaction control capabilities of an mr-compatible compliant actuator for wrist sensorimotor protocols during fmri," *IEEE/ASME Transactions on Mechatronics*, vol. 20, no. 6, pp. 2678–2690, 2015.

[17] Q. Ding, Y. Lu, A. Kyme, and S. S. Cheng, "Towards a multi-imager compatible continuum robot with improved dynamics driven by modular sma," in *Proceedings - IEEE International Conference on Robotics and Automation*, vol. 2021-May, Conference Proceedings, pp. 11 930–11 937, export Date: 28 May 2025; Cited By: 13.

[18] Z. Tang, S. Sugano, and H. Iwata, "Development and evaluation of an mri compatible finger rehabilitation device for stroke patients," in *IEEE International Conference on Intelligent Robots and Systems*, vol. 2015-December, Conference Proceedings, pp. 5005–5010, export Date: 28 May 2025; Cited By: 4.

[19] Y. M. Senturk and V. Patoglu, "*MRI-VisAct* : a Bowden-cable-driven MRI-compatible series viscoelastic

actuator," *Transactions of the Institute of Measurement and Control*, vol. 40, no. 8, pp. 2440–2453, May 2018. [Online]. Available: https://journals.sagepub.com/doi/10.1177/0142331217730429

[20] V. Groenhuis and S. Stramigioli, "Rapid Prototyping High-Performance MR Safe Pneumatic Stepper Motors," *IEEE/ASME Transactions on Mechatronics*, vol. 23, no. 4, pp. 1843–1853, 2018, type: Journal Article.

[21] Z. Dong, Z. Guo, K. H. Lee, G. Fang, W. L. Tang, H. C. Chang, D. T. M. Chan, and K. W. Kwok, "High-Performance Continuous Hydraulic Motor for MR Safe Robotic Teleoperation," *IEEE Robotics and Automation Letters*, vol. 4, no. 2, pp. 1964–1971, 2019, type: Journal Article.

[22] S. Menon, A. Soviche, J. Mithrakumar, A. Subbarao, H. Ganti, and O. Khatib, "Haptic fmri: A novel five dof haptic interface for multi-axis motor neuroscience experiments," in *2017 IEEE World Haptics Conference (WHC)*, Conference Proceedings, pp. 13–18.

[23] B. Vigaru, J. Sulzer, and R. Gassert, "Design and Evaluation of a Cable-Driven fMRI-Compatible Haptic Interface to Investigate Precision Grip Control," *IEEE Transactions on Haptics*, vol. 9, no. 1, pp. 20–32, Jan. 2016. [Online]. Available: https://ieeexplore.ieee.org/document/7286837/

[24] J. H. Jung, N. Pan, and T. J. Kang, "Capstan equation including bending rigidity and non-linear frictional behavior," *Mechanism and Machine Theory*, vol. 43, no. 6, pp. 661–675, Jun. 2008. [Online]. Available: https://www.sciencedirect.com/science/article/pii/S0094114X07001152

[25] D. Chen, Y. Yun, and A. D. Deshpande, "Experimental characterization of Bowden cable friction," in *2014 IEEE International Conference on Robotics and Automation (ICRA)*, May 2014, pp. 5927–5933. [Online]. Available: https://ieeexplore.ieee.org/document/6907732/

[26] V. Groenhuis, F. J. Siepel, and S. Stramigioli, "Magnetic Resonance Pneumatic Stepper Motor With Multiple Concentric Shafts Output," *IEEE/ASME Transactions on Mechatronics*, vol. 27, no. 4, pp. 2379–2389, 2022, type: Journal Article.

[27] D. D. J. Williams, "A robot for wrist rehabilitation," Ph.D. dissertation, Massachusetts Institute of Technology, 2001. [Online]. Available: http://hdl.handle.net/1721.1/8551

[28] A. C. Schouten, E. de Vlugt, J. J. B. van Hilten, and F. C. T. van der Helm, "Design of a torque-controlled manipulator to analyse the admittance of the wrist joint," *Journal of Neuroscience Methods*, vol. 154, no. 1, pp. 134–141, Jun. 2006. [Online]. Available: https://www.sciencedirect.com/science/article/pii/S0165027005004498

[29] E. J. Perreault, R. F. Kirsch, and P. E. Crago, "Effects of voluntary force generation on the elastic components of endpoint stiffness," *Experimental Brain Research*, vol. 141, no. 3, pp. 312–323, Dec. 2001. [Online]. Available: https://doi.org/10.1007/s002210100880

[30] Gassert, R., Moser, R., Burdet, E, and Bleuler, H., "MRI/fMRI-Compatible Robotic System With Force Feedback for Interaction With Human Motion," 2006. [Online]. Available: https : / / www.researchgate.net / publication / 3415118_MRIfMRI - Compatible_Robotic_System_With_Force_Feedback_for_Interaction_With_Human_Motion

[31] Stokey, W., "VIBRATION OF SYSTEMS HAVING DISTRIBUTED MASS AND ELASTICITY," in *Harris' Shock and Vibration Handbook*.

[32] M. Eryildiz, "Effect of Build Orientation on Mechanical Behaviour and Build Time of FDM 3D-Printed PLA Parts: An Experimental Investigation," *European Mechanical Science*, vol. 5, pp. 116–120, Sep. 2021.

[33] W. Mugge, J. Schuurmans, A. C. Schouten, and F. C. T. Van Der Helm, "Sensory Weighting of Force and Position Feedback in Human Motor Control Tasks," *The Journal of Neuroscience*, vol. 29, no. 17, pp. 5476–5482, Apr. 2009. [Online]. Available: https://www.jneurosci.org/lookup/doi/10.1523/JNEUROSCI.0116-09.2009

[34] dr. Mark van de Ruit, "ME41066: System Identification and Parameter Estimation," Jan. 2026.

[35] P. Welch, "The use of fast Fourier transform for the estimation of power spectra: A method based on time averaging over short, modified periodograms," *IEEE Transactions on Audio and Electroacoustics*, vol. 15, no. 2, pp. 70–73, Jun. 1967. [Online]. Available: https://ieeexplore.ieee.org/document/1161901/

Appendix A
Prototype Development

Remote Torque Transmission for MR-Conditional Haptic Manipulation: A Torsion-Rod Approach

T.A. Valk

Delft University of Technology, Delft, 2628CD, The Netherlands

This appendix documents the design iterations and fabrication details for the prototype described in Section III of the main paper. The appendix also includes data tables containing the information required for reproducing the modeled results in Section IV of the main paper. The problem statement, clinical motivation, system requirements, concept selection and preliminary calculations are defined in the main paper and are not repeated here.

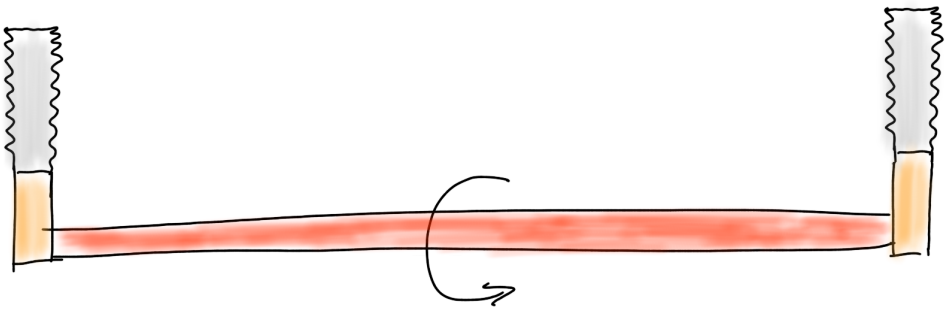

Figure A.1: Simple sketch of the first prototype

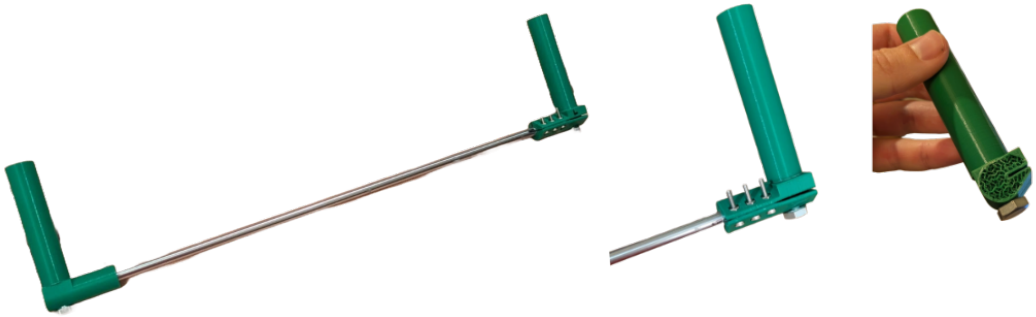

Figure A.2: Iteration 1: torsion rod with 3D-printed clamp and handle. The clamp is tightened with M3 bolts and bonded with Loctite adhesive. The handle contains an embedded M8 bolt for bending stiffness. On the right the breakage is shown.

A.1 Design Iterations

A.1.1 Iteration 1: First Torsion Rod Clamp

The first iteration was a minimal prototype intended to answer three practical questions: how to clamp onto a torsion rod without slippage, how the handle feels to operate, and whether failure occurs at unexpected locations. A sketch of the idea is shown in Figure A.1.

A leftover steel rod was used as the torsion element. A clamp was 3D-printed and tightened onto the rod with M3 bolts. Rotating the clamp required considerable force, suggesting that at larger rod diameters a friction clamp alone may suffice without adhesive; at the diameter tested, Loctite adhesive was added to prevent slippage. A long M8 bolt was embedded in the handle to provide additional bending stiffness. An overview of the prototype is given in Figure A.2.

The prototype failed at the interface between the clamp and the handle, which was the expected weak point given that a 3D-printed plastic part was loaded in bending against a steel rod. The failure confirmed that 3D-printed components should bear minimal

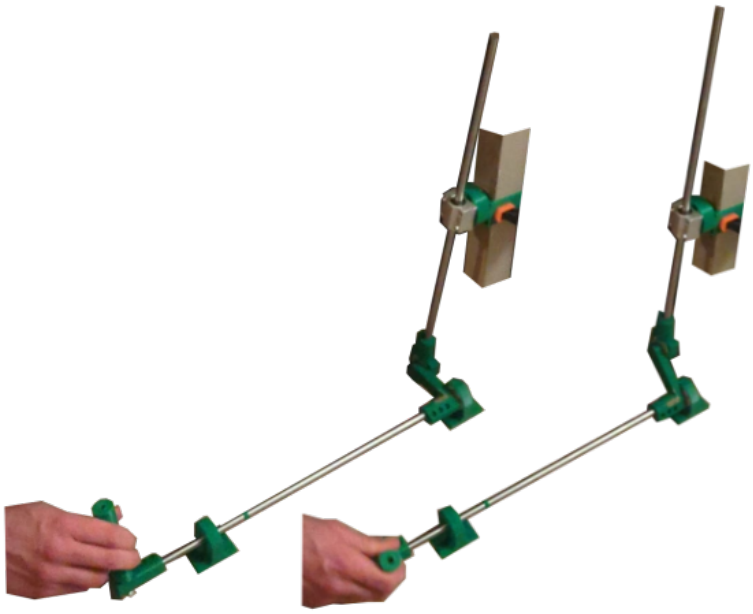

Figure A.3: Crank-and-slider joint added to iteration 1, converting torsional motion of the rod into linear pushrod motion guided by a slide bearing.

structural loads in future iterations, and that load-bearing interfaces should be reinforced with metal inserts or replaced with aluminum parts. The handle size was adequate for comfortable grip and required no modification.

A simple crank-and-slider joint was added to demonstrate conversion of torsional motion into linear motion, shown in Figure A.3. The pushrod translates vertically and is guided by a plain slide bearing. Ideally, the pushrod would connect to a second torsion stage, but a guided slider was sufficient to validate the operating principle at this stage.

A.1.2 Iteration 2: Rigid Arms, Alignment Issues

The second iteration extended the concept to demonstrate that motion could be transported along a path with multiple 90° bends, as required in a full MRI installation. The transmission chain topology is shown in Figure A.4: torsion rods handle the straight segments and crank-pushrod stages redirect motion at each bend.

Two 90° bends were incorporated, routing motion up and over a table edge to demonstrate that the principle scales to a multi-stage configuration. The CAD assembly is shown in Figure A.5 and the physical prototype in Figure A.6.

Several problems were identified during assembly and testing. Alignment of the torsion stages was difficult to achieve because the crank arms were rigid and the pushrods used groove ball bearings, which require the groove plane to remain perpendicular to the

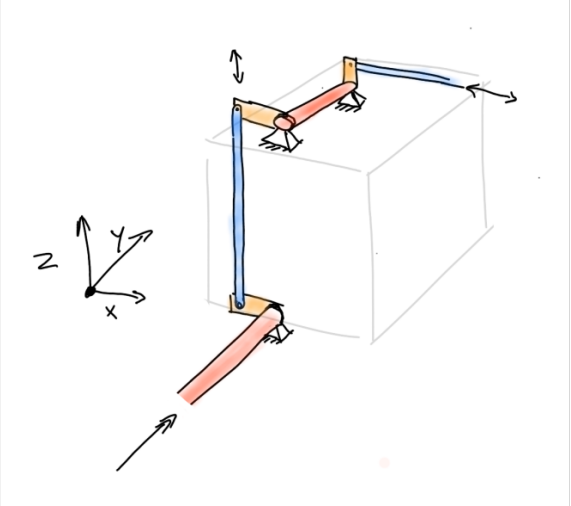

Figure A.4: Transmission chain topology showing alternating torsion rods (blue) and pushrods (pink) with crank joints at each 90° bend.

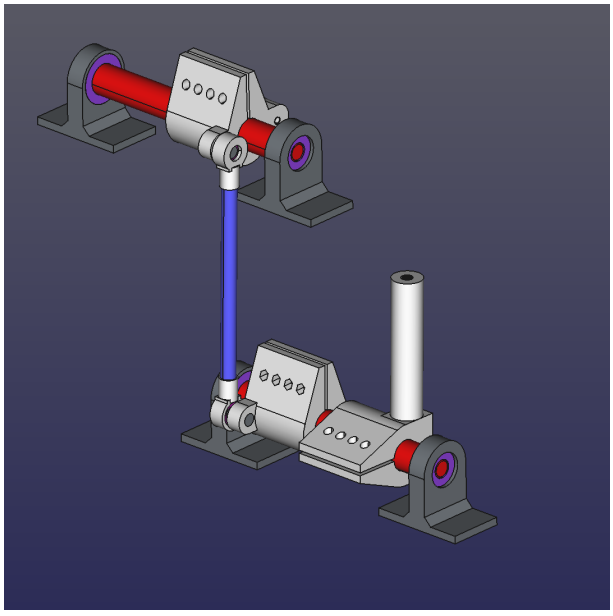

Figure A.5: CAD assembly of iteration 2. Rod lengths are shortened in the model for clarity; the physical prototype used full-length rods.

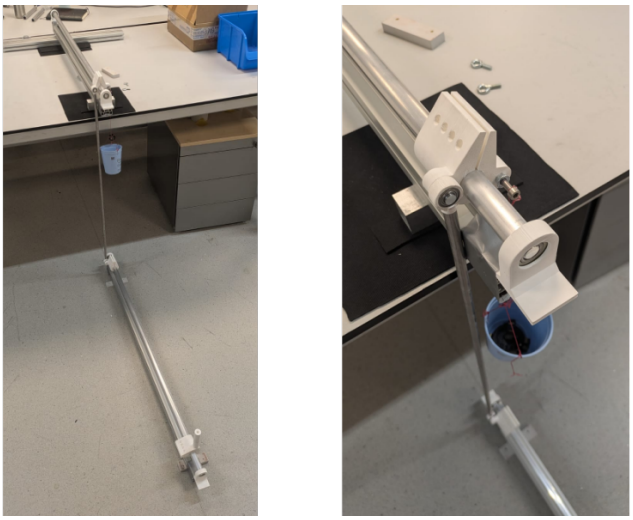

Figure A.6: Physical prototype of iteration 2, showing two 90° bends and the crank-pushrod joints at each corner.

pushrod axis throughout the full range of motion. Additionally, the rod sections were not mounted to a rigid frame, allowing the pushrods to push the torsion rods out of alignment rather than rotating them. The crank radius of 25 mm was also insufficient, limiting the range of motion to approximately ±50° before the pushrod would collide with the torsion rod. The following iteration addressed the alignment issue and increased the crank radius. Spherical rod ends were not yet incorporated in the next iteration, as the lead time was too high.

A.1.3 Iteration 3: Single Plate, First Bandwidth Results

The primary problem identified in iteration 2 was misalignment between torsion stages. A compliant plate element was introduced to address the misalignment: a thin plate has high in-plane stiffness but low out-of-plane bending stiffness, allowing it to accommodate small angular misalignments passively while remaining stiff in the load-bearing direction. An early concept of the plate design is shown in Figure A.7.

The entire transmission was mounted on aluminum extrusion profiles for the first time, providing a rigid structural frame that prevented the pushrods from displacing the torsion rods. The initial PMMA plate was replaced with a 2 mm aluminum plate, as PMMA proved too compliant under load. The crank radius was increased from 25 mm to 50 mm to allow a larger range of motion. ZF Electronics AN820032 angle sensors were added to the input and output shafts for the first time, logged by an Arduino at 200 Hz, enabling quantitative performance measurement. The complete setup is shown in Figure A.8. The wiring diagram of the sensors to the Arduino is shown in Figure A.9. The sensor itself is depicted in Figure A.10.

A first bandwidth estimation was performed using hand excitation, following the approach

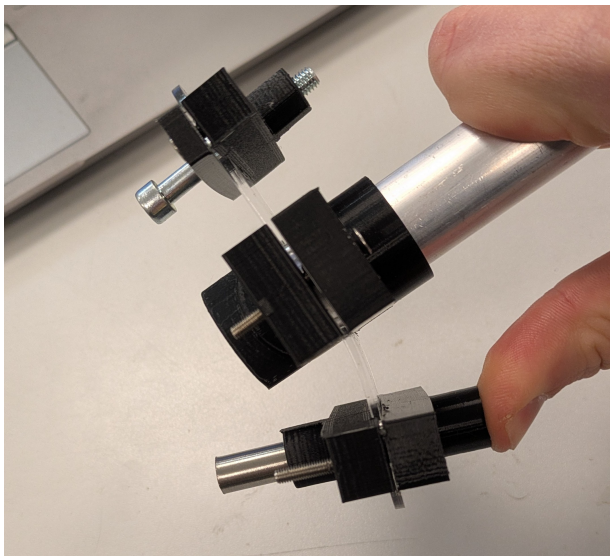

Figure A.7: The plate element bends out of plane to accommodate angular misalignment between torsion stages. The plate shown is 2 mm thick PMMA.

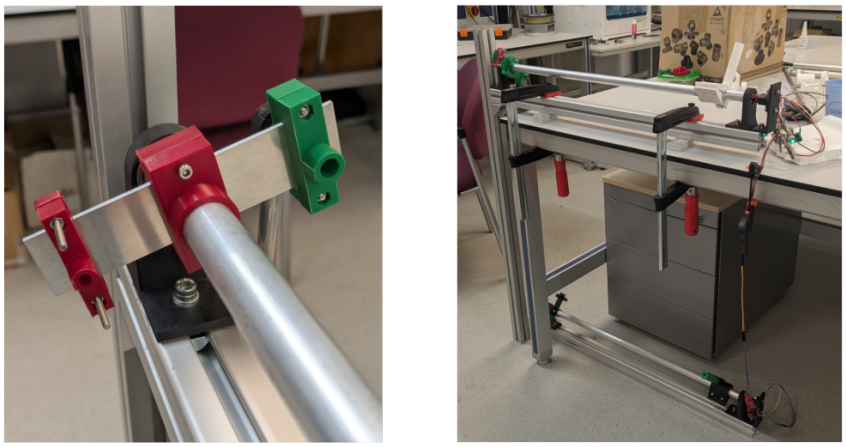

Figure A.8: Iteration 3: aluminum plate joint detail (left) and complete setup mounted on extrusion profiles (right).

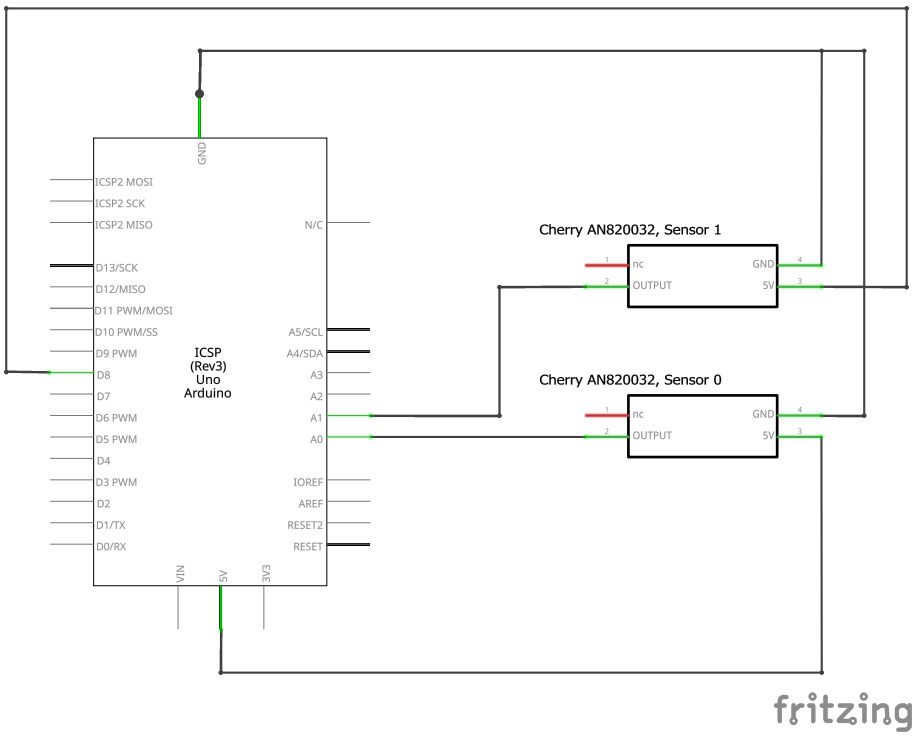

Figure A.9: The wiring diagram of the Arduino.

Figure A.10: ZF Electronics AN820032 angle sensor. The magnet, depicted on the right was mounted directly on the input and output shaft. The sensor was mounted on the input bracket.

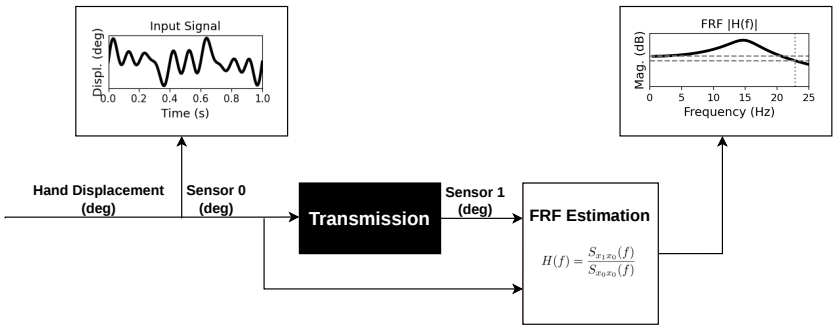

Figure A.11: Schematic of the hand-excitation bandwidth estimation method used in iteration 3. Input and output angles are recorded simultaneously and processed into a frequency response estimate.

illustrated in Figure A.11. Coherence dropped above 10 Hz, and the frequency content of the applied force was unknown. Hand excitation was therefore deemed insufficient for reliable FRF estimation, and the Proprio hydraulic actuator was used for all subsequent measurements.

The result, shown in Figure A.12, indicated 0 dB gain up to 10 Hz, meaning input and output motion were equal in magnitude across the full range of reliable human excitation. Coherence dropped below 0.8 above 10 Hz, indicating insufficient excitation power at higher frequencies rather than a loss of transmission performance. The bandwidth marker in the figure is beyond 10 Hz and is therefore unreliable. It should not be interpreted as the true bandwidth of the system. The result was nonetheless encouraging: the transmission showed no measurable attenuation up to the limit of hand excitation, suggesting the actual bandwidth was higher than 10 Hz. Determining the actual bandwidth required an actuator capable of exciting the system beyond 10 Hz with sufficient and controlled power. The method used to achieve this with the final prototype is described in Section III of the main paper.

The results justified scaling the concept up into a final prototype. Two design changes were carried forward. First, the groove ball bearings from iteration 2 were replaced with spherical rod ends, which inherently tolerate angular misalignment. Second, the single-plate design placed the pushrod attachment point offset from the plate midplane, generating an undesirable bending moment in the plate under load. The plates were therefore doubled up in the final design, with the pushrod connecting between the two plates at the midplane, placing the load symmetrically and eliminating the out-of-plane bending.

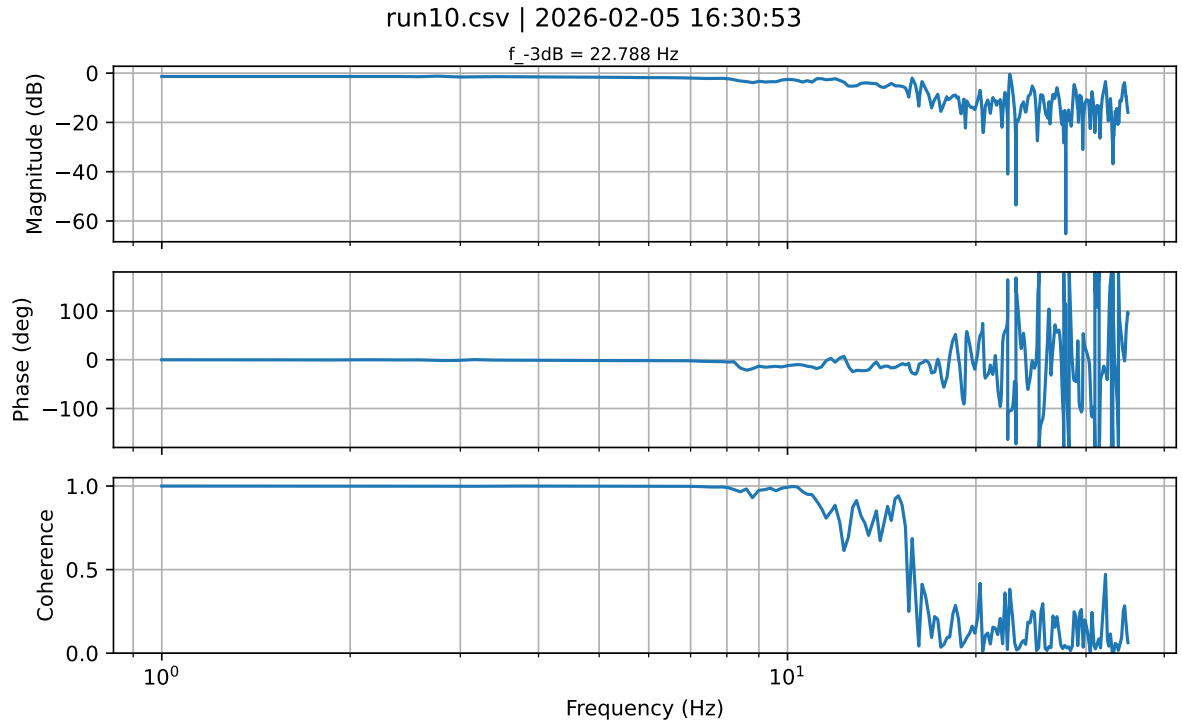

Figure A.12: First bandwidth measurement of iteration 3 using hand excitation. The 0 dB gain region extends to 10 Hz. Coherence drops below 0.8 above 10 Hz, making the bandwidth estimate beyond that frequency unreliable.

A.1.4 Iteration 4: Final Prototype

The double-plate joint introduced in iteration 3 was refined into a fully symmetric assembly. Each joint consists of two aluminum plates that slide onto the torsion rod and are clamped together by two 3D-printed clamps tensioned with bolts. An axle is suspended between the plates and retained by two slide bearings, which are held in a clamp fitting around the outer faces of the plates. The spherical rod end attaches to the axle, connecting the torsion rod crank to the pushrod. Load is transferred symmetrically through both plates, eliminating the out-of-plane bending moment identified in iteration 3. The assembled joints are shown in Figure A.13.

A small O-ring was added between the slide bearing and the rod end to eliminate axial play. Without the O-ring, the rod end could slide along the axle under load, introducing backlash into the transmission. The O-ring creates a light preload that keeps the rod end seated without restricting the spherical rotation needed for misalignment tolerance. The O-ring installation is shown in Figure A.14.

The pushrods are hollow aluminum tubes. Solid rods were used initially, but a buckling analysis confirmed that hollow tubes of the selected wall thickness provided sufficient buckling resistance at the maximum expected compressive load, at a significantly lower mass. The assembled pushrod is shown in Figure A.15. Two tube halves are joined by a shaft coupling, which attaches to each tube with a setscrew. Longitudinal adjustment of

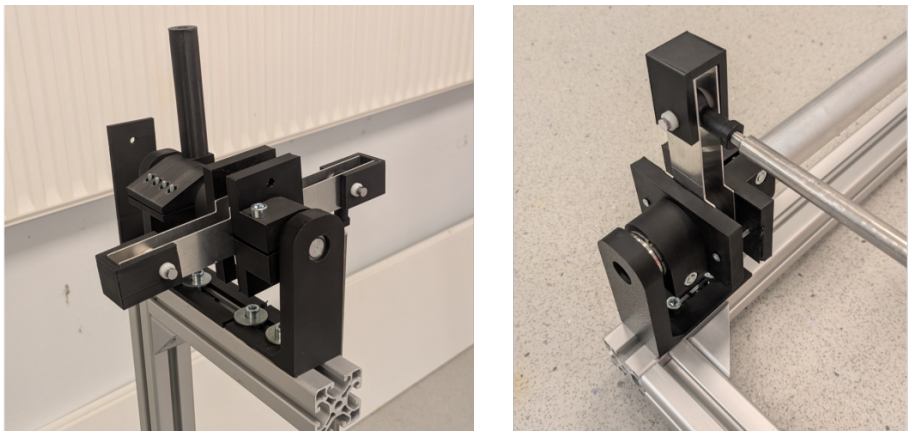

Figure A.13: Double-plate joint assembly at the input handle (left), incorporating a spherical rod end on the suspended axle, and at an intermediate joint (right).

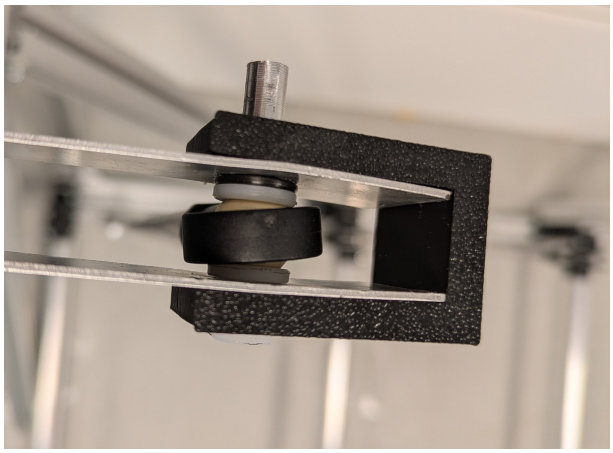

Figure A.14: O-ring installed between the slide bearing and the rod end to eliminate axial play on the axle.

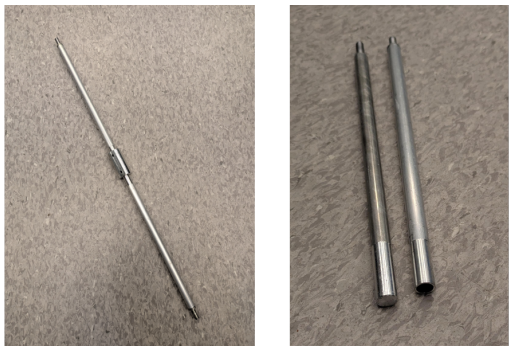

Figure A.15: Assembled pushrod with shaft coupling (left). Solid and hollow pushrod variants shown for comparison (right); the hollow variant was selected for the final prototype.

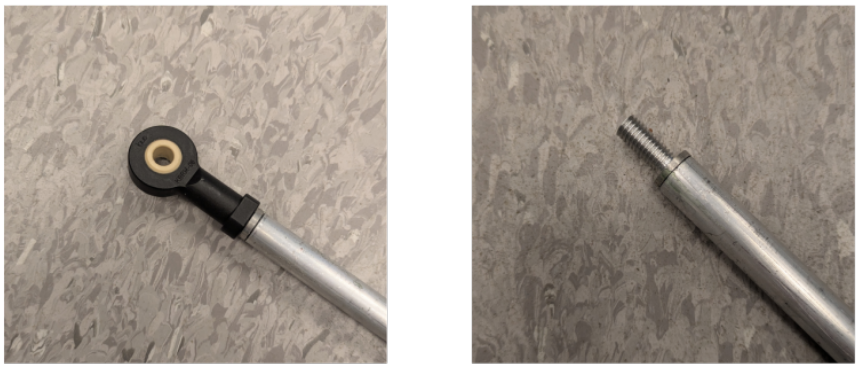

Figure A.16: igus KRBM-06 spherical rod end (left). Right-hand threaded aluminum insert bonded into the hollow pushrod tube end with Loctite 638 (right).

the two halves within the coupling allows the transmission to be aligned during assembly without disassembling the joints. Both tube ends are right-hand threaded to accept the igus KBRM-06 spherical rod end, shown in Figure A.16. The threaded interface is a machined aluminum insert bonded into the tube end using Loctite 638 anaerobic adhesive. The igus KBRM-06 rod ends are constructed from iglide polymer and are MR-Safe; they were prioritized for MR-Safe material selection given their direct role in transmission performance.

The torsion rods are also hollow aluminum tubes to minimize rotational inertia. Solid aluminum inserts are bonded into both ends of each tube using Loctite 638, providing a solid interface for the steel roller bearings that suspend the torsion rod in its mounting bracket. The insert and assembled torsion rod are shown in Figure A.17.

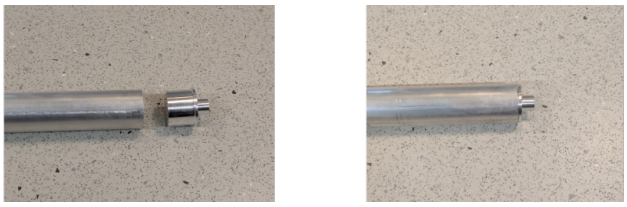

Figure A.17: Hollow torsion rod tube with solid aluminum insert prior to bonding (left). Assembled torsion rod with insert seated in the steel roller bearing (right).

A.2 Compliance and Reflected Mass Models

A.2.1 Reflected Mass Model Data

Table A.1: Reflected mass budget for both configurations. Effective radius is the assumed moment arm for each component. Components above the dividing line are distributed elements contributing $I/3$; components below contribute their full inertia. The measurement-derived reflected mass is included for comparison.

Component	Mass (g)	r_{eff} (mm)	Configs
Distributed elements (contribute $I/3$)			
Torsion rods	1476	14.5	A, B
Torsion rod inserts (per joint)	39	14.0	A, B
Crank-actuator assembly	220	75	A, B
Input rod assembly	140	75	A, B
Horizontal pushrods ($\times 2$)	230	75	A only
Horizontal counter rod	140	75	A only
Shaft couplers ($\times 3$)	360	20	B only
Concentrated elements (contribute full mr^2)			
Handle	50	30	A, B
Output rod assembly	150	75	A, B
Predicted m_{refl} (g)		Square: 417	Straight: 302
Measured m_{refl} (g)		Square: 291	Straight: 289

A.2.2 Compliance Model

Table A.2: Geometric and material parameters for the series compliance model. All components modeled as cantilever beams unless noted. Clamp and coupler stiffness values include a factor of 10 to account for steel bolt clamping (*).

Component	Material	Dimensions	p_{infill}	k (N m rad^{-1})
Torsion rod	Al 6061	$\oslash 30\,\text{mm} \times 1\,\text{mm}$, $L = 6\,\text{m}$	—	84.1
Pushrods (Square)	Al 6061	$\oslash 10\,\text{mm} \times 1\,\text{mm}$, $L = 3\,\text{m}$	—	3711
Pushrods (Straight)	Al 6061	$\oslash 10\,\text{mm} \times 1\,\text{mm}$, $L = 1.5\,\text{m}$	—	7422
Crank plates	Al 6061	$b = 1\,\text{mm}$, $h = 20\,\text{mm}$, $L = 75\,\text{mm}$, $\times 2$	—	3733
Bearing housing, Square IP	PLA ($E/3$)	$b = 12.5\,\text{mm}$, $h = 40\,\text{mm}$, $L = 80\,\text{mm}$	0.15	1050
Bearing housing, Square OOP	PLA ($E/3$)	$b = 40\,\text{mm}$, $h = 12.5\,\text{mm}$, $L = 80\,\text{mm}$	0.15	102
Bearing housing, Straight IP	PLA ($E/3$)	$b = 25\,\text{mm}$, $h = 40\,\text{mm}$, $L = 80\,\text{mm}$	0.15	2101
Bearing housing, Straight OOP	PLA ($E/3$)	$b = 40\,\text{mm}$, $h = 25\,\text{mm}$, $L = 80\,\text{mm}$	0.15	257
Rod end (iglidur)	iglidur J	$\oslash 10\,\text{mm}$ solid, $L = 30\,\text{mm}$	0.70	72 158
Clamp*	PLA	$\oslash 40\,\text{mm}/30\,\text{mm}$ ring, $L = 84\,\text{mm}$	0.15	5768
Coupler*	PLA	$\oslash 44\,\text{mm}/30\,\text{mm}$ tube, $L = 150\,\text{mm}$	1.00	21 691

*Effective stiffness includes $\times 10$ factor for steel bolt clamping.

Table A.3: Compliance breakdown for both configurations, with and without out-of-plane bearing housing deflection ($\alpha = 0$ and $\alpha = 0.3$). Values are total compliance contributions including joint count multiplier. Percentages are of total compliance. Measured stiffness included for comparison.

	Square ($n = 10$ joints)		Straight ($n = 4$ joints)	
Component	$\alpha = 0$	$\alpha = 0.3$	$\alpha = 0$	$\alpha = 0.3$
Torsion rod	45.3 %	22.6 %	74.8 %	59.5 %
Bearing housings	36.3 %	68.3 %	12.0 %	30.0 %
Crank plates	10.2 %	5.1 %	6.7 %	5.4 %
Clamps	6.6 %	3.3 %	4.4 %	3.5 %
Couplers	—	—	0.9 %	0.7 %
Rod ends	0.5 %	0.3 %	0.3 %	0.3 %
Pushrods	1.0 %	0.5 %	0.8 %	0.7 %
Predicted k ($\mathrm{N\,m\,rad^{-1}}$)	38.2	19.0	63.0	50.1
Measured k ($\mathrm{N\,m\,rad^{-1}}$)	14.5		48.5	

Appendix B
Signals

Remote Torque Transmission for MR-Conditional Haptic Manipulation: A Torsion-Rod Approach

T.A. Valk

Delft University of Technology, Delft, 2628CD, The Netherlands

This appendix documents the excitation signals and measurement runs used for FRF estimation of the Square and Straight-Line Configurations. Signal generation, the peak-finding procedure, and the FRF computation method are described in Section IV of the main paper.

B.1 Measurement Parameters

This section documents the excitation signal parameters and processing settings for each measurement run used in the FRF estimation of the Square Configuration and the Straight-Line Configuration. Run numbers reflect the chronological order of all measurements taken during the project; non-consecutive numbering indicates runs that were discarded or repeated. The frequency band column defines the range of the multisine excitation for that run. Δf is the frequency resolution of the multisine, determining the spacing between excited frequencies. The PSD band column defines the frequency range within which peaks were searched in the sensor 0 spectrum. Despiking indicates whether the spike-removal filter was applied to the input signal (X), output signal (Y), both (XY), or neither. The prominence threshold $P_{\min}$ is the per-run value used in the peak-finding algorithm, as described in Section IV of the main paper.

B.2 Signals: Square Configuration

Table B.1 summarizes the measurement parameters for each run of the Square Configuration. Five runs were conducted, covering the frequency range 0.5 Hz to 20 Hz in overlapping bands. Signal amplitude and gain were increased for higher-frequency runs to compensate for reduced actuator authority. Despiking was applied to the input signal in runs 79 and 80, and to the output signal in run 74.

Table B.1: Signal parameters for the Square Configuration measurement runs. $\Delta f = 0.5$ Hz. Proprio stiffness setting = 70/600.

Run	Freq. band (Hz)	PSD band (Hz)	Signal Amp.	Gain	Despiking	$P_{\min}$ (dB)
56	0.5–10	0–13	500	15	—	42
79	9.5–12.5	11.5–16	5000	3	X	50
80	12–15	14.5–19	5000	6	X	15
73	15–17.5	18–23	5000	10	X	15
74	17–20	21–26	5000	10	Y	15

Despiking notation: X = input signal despiked; Y = output signal despiked.

B.2.0.1 Run 56 (0.5 Hz to 10 Hz)

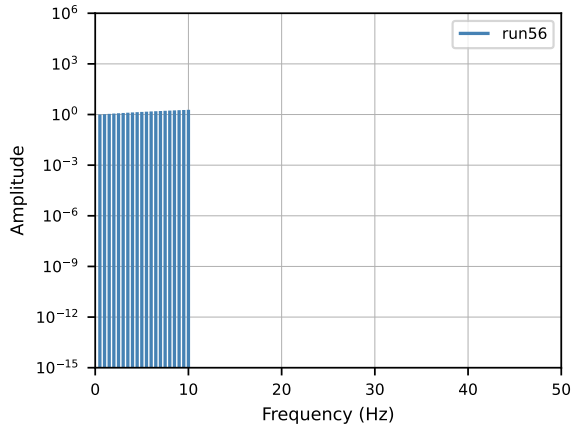

Figure B.1: Weighted input spectrum, run 56.

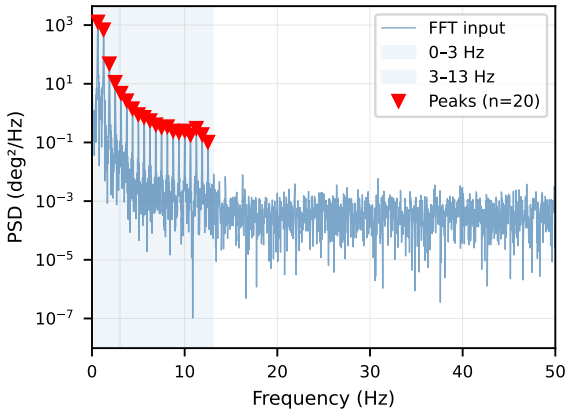

Figure B.2: PSD of input signal, run 56. Detected peaks indicated.

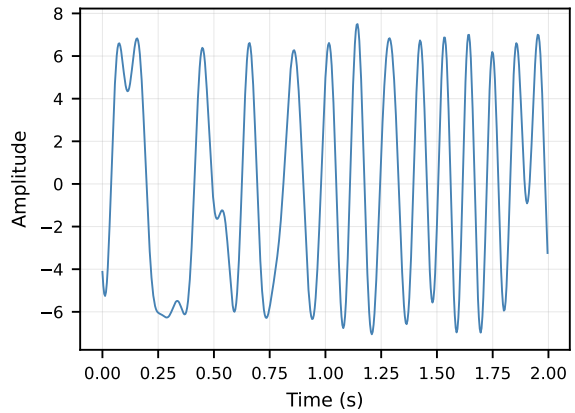

Figure B.3: Weighted time signal, run 56.

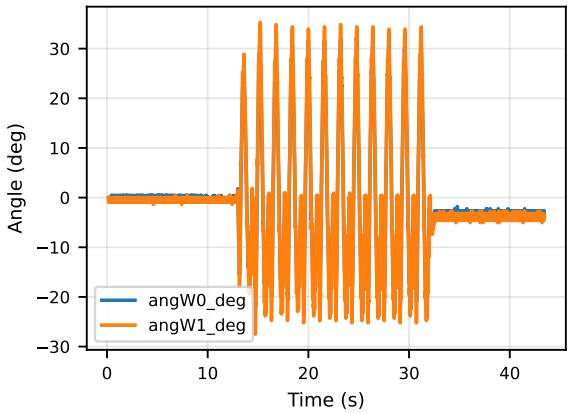

Figure B.4: Raw time signals (input and output), run 56.

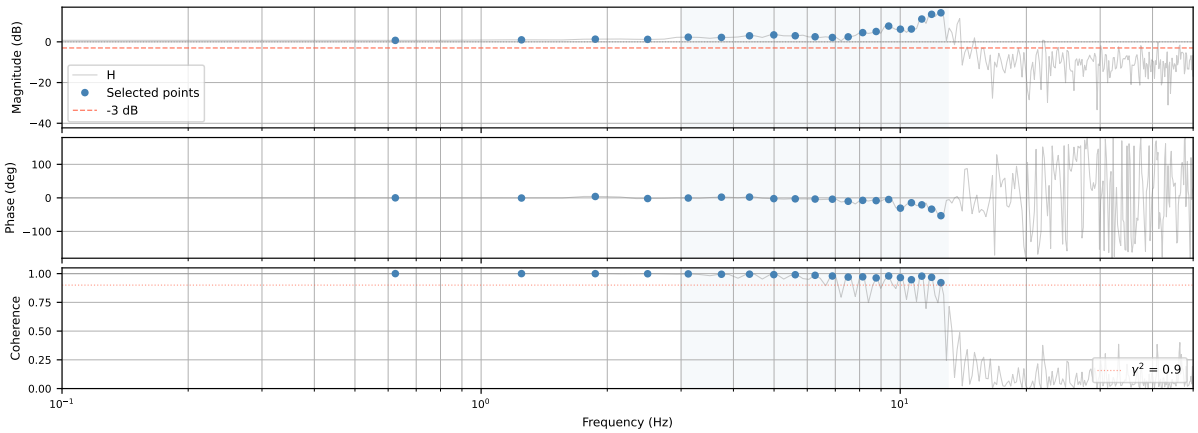

Figure B.5: Measured FRF, run 56 (0.5 Hz to 10 Hz).

B.2.0.2 Run 79 (9.5 Hz to 12.5 Hz)

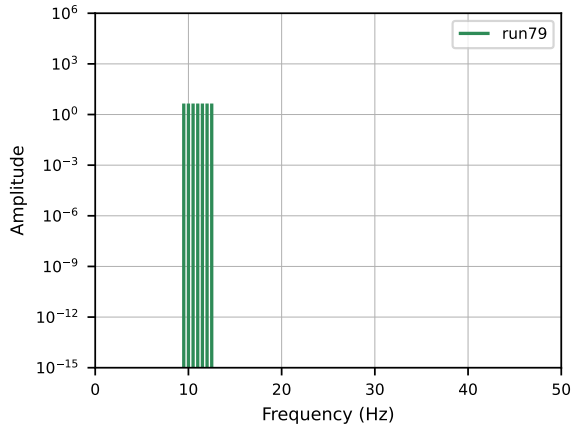

Figure B.6: Weighted input spectrum, run 79.

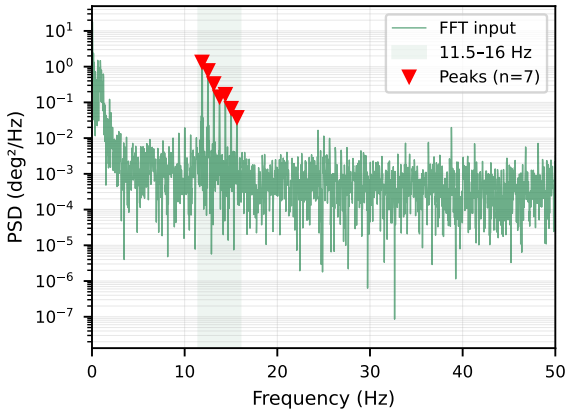

Figure B.7: PSD of input signal, run 79. Detected peaks indicated.

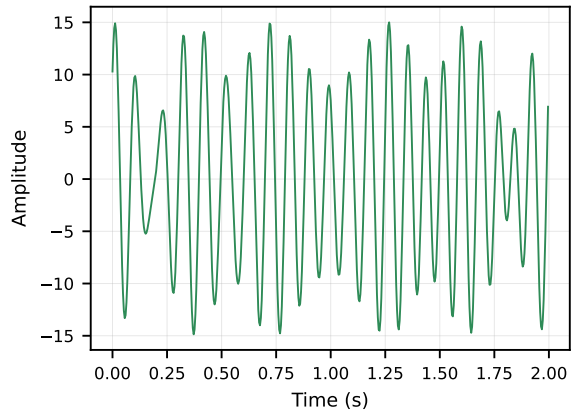

Figure B.8: Weighted time signal, run 79.

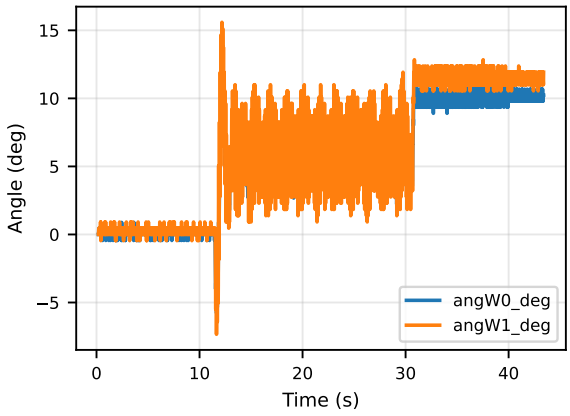

Figure B.9: Raw time signals (input and output), run 79. Input despiked.

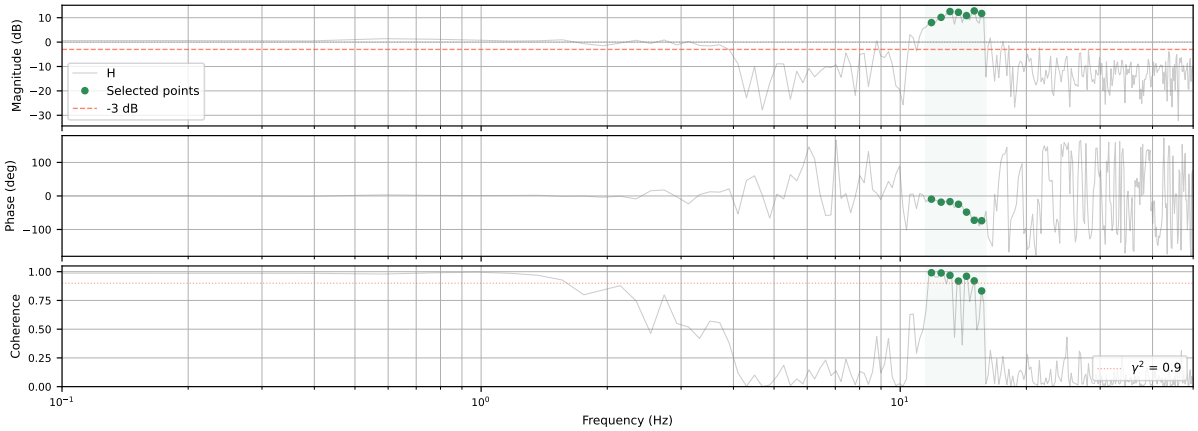

Figure B.10: Measured FRF, run 79 (9.5 Hz to 12.5 Hz).

B.2.0.3 Run 80 (12 Hz to 15 Hz)

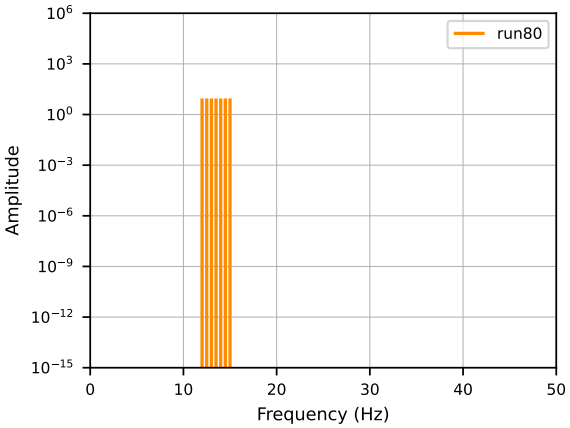

Figure B.11: Weighted input spectrum, run 80.

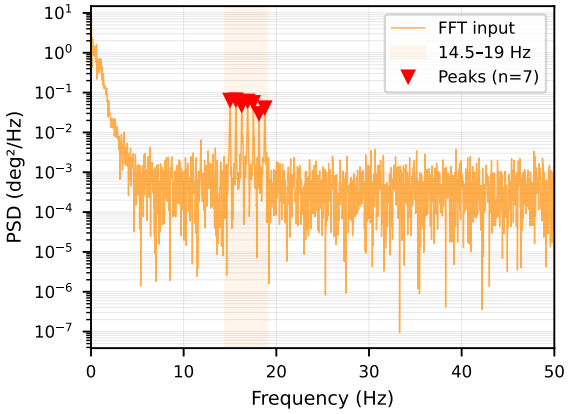

Figure B.12: PSD of input signal, run 80. Detected peaks indicated.

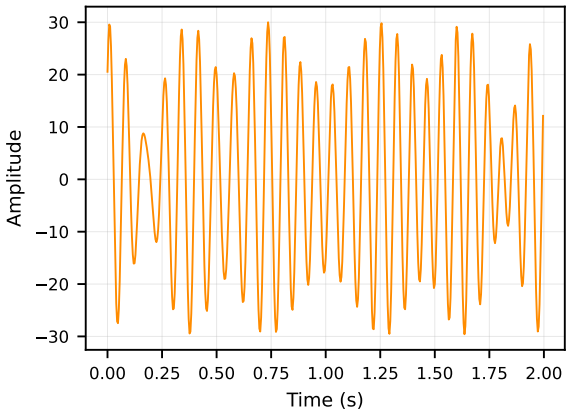

Figure B.13: Weighted time signal, run 80.

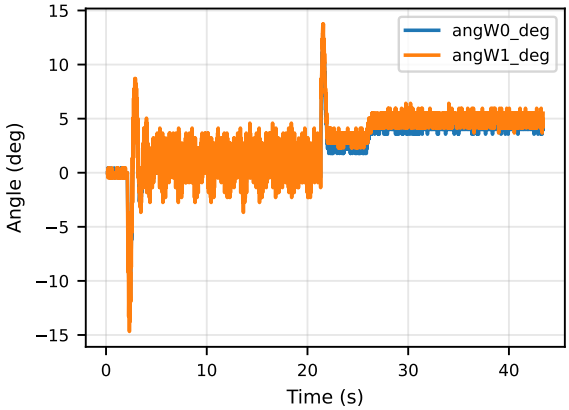

Figure B.14: Raw time signals (input and output), run 80. Input despiked.

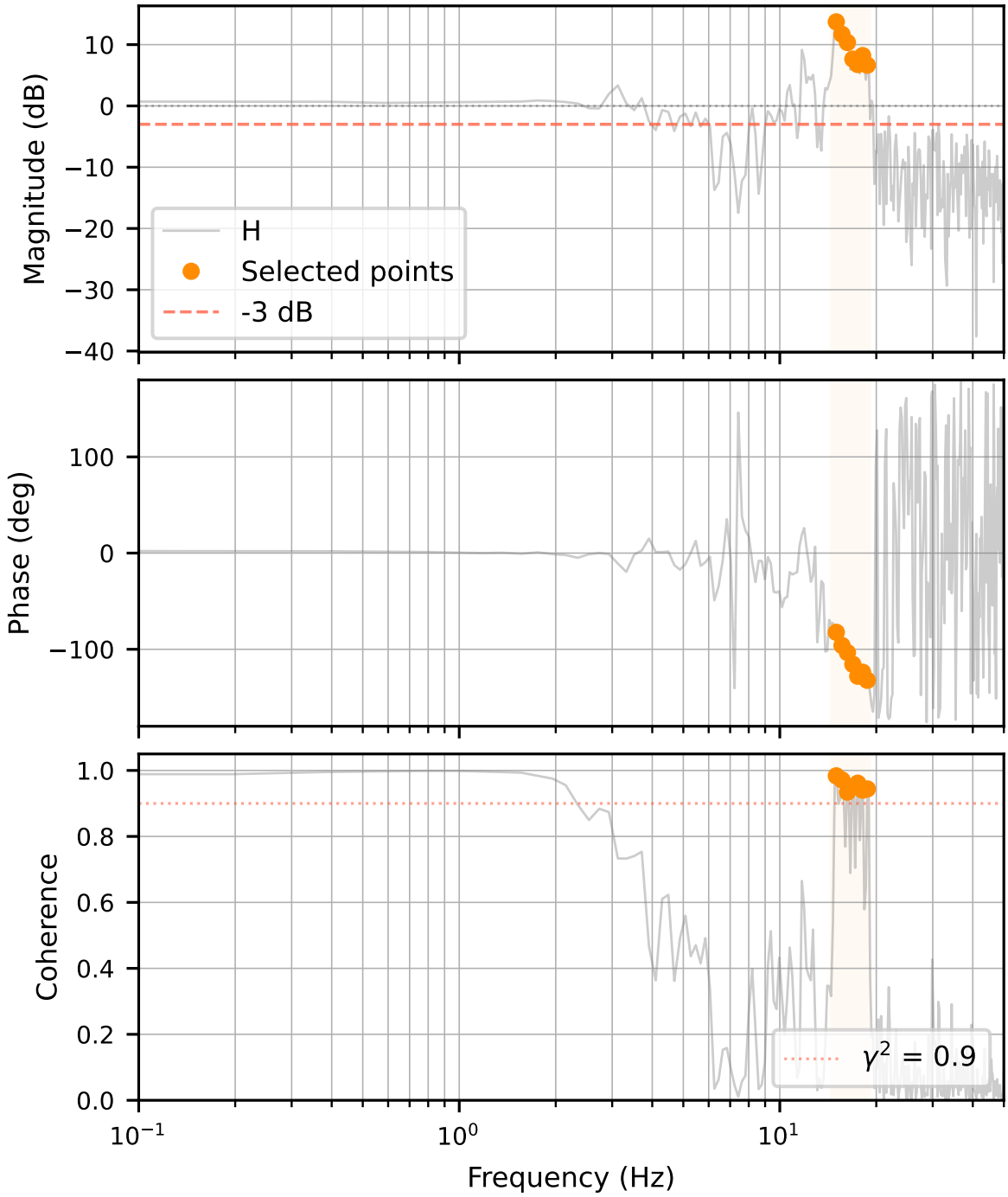

Figure B.15: Measured FRF, run 80 (12 Hz to 15 Hz).

B.2.0.4 Run 73 (15 Hz to 17.5 Hz)

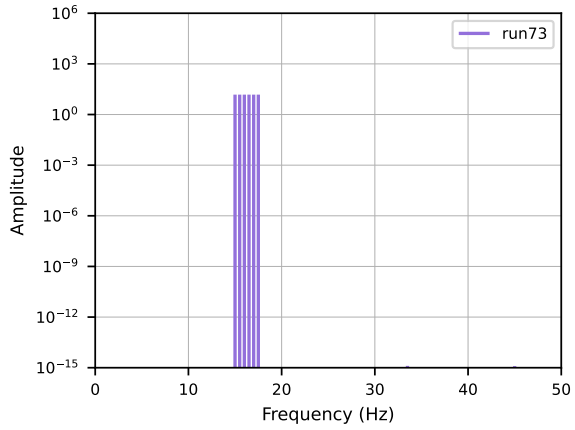

Figure B.16: Weighted input spectrum, run 73.

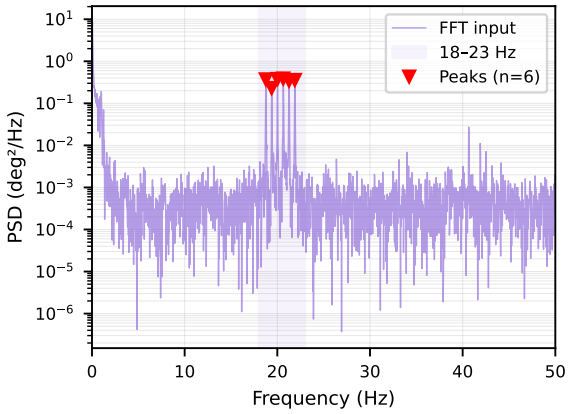

Figure B.17: PSD of input signal, run 73. Detected peaks indicated.

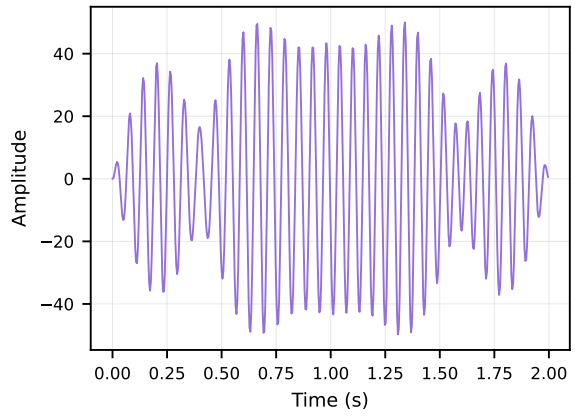

Figure B.18: Weighted time signal, run 73.

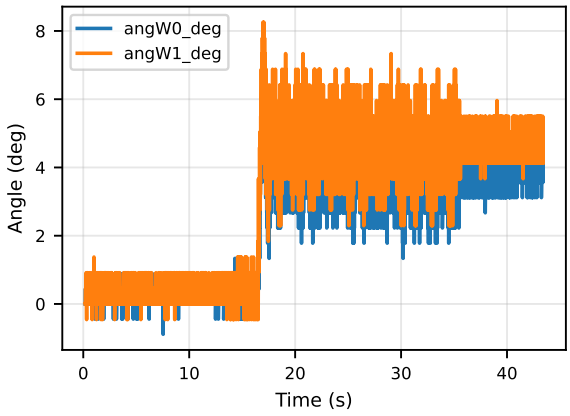

Figure B.19: Raw time signals (input and output), run 73.

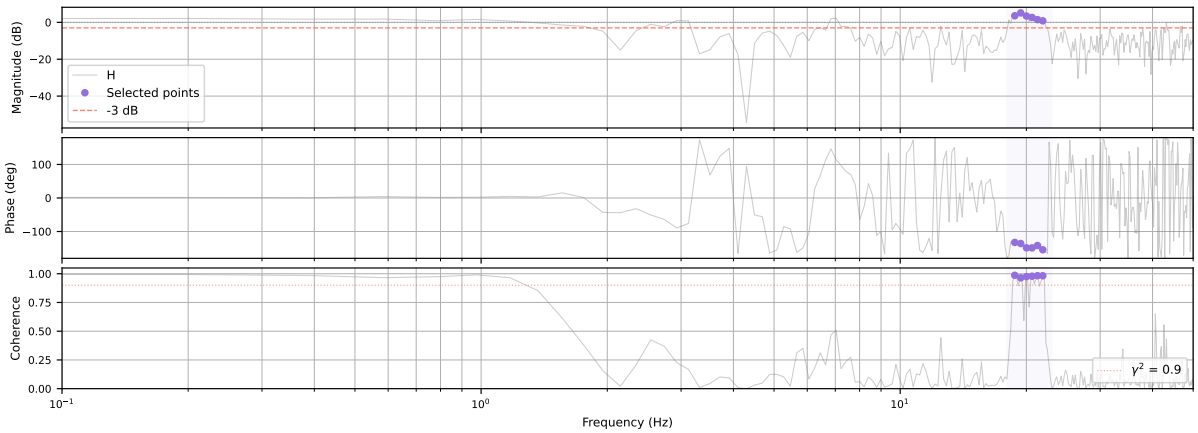

Figure B.20: Measured FRF, run 73 (15 Hz to 17.5 Hz).

B.2.0.5 Run 74 (17 Hz to 20 Hz)

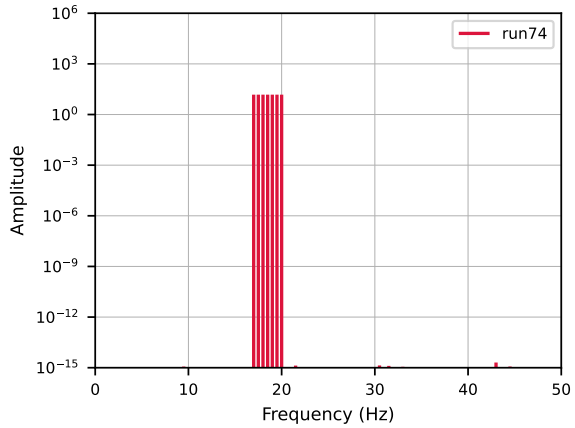

Figure B.21: Weighted input spectrum, run 74.

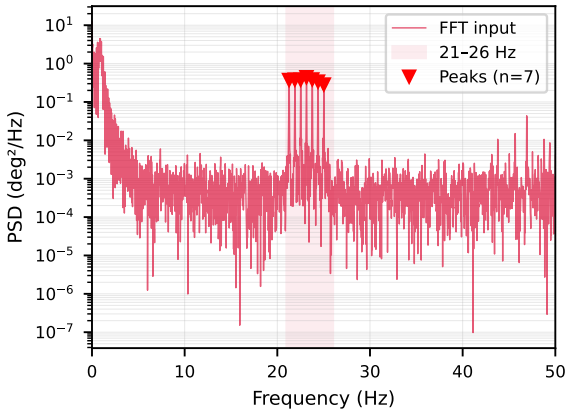

Figure B.22: PSD of input signal, run 74. Detected peaks indicated.

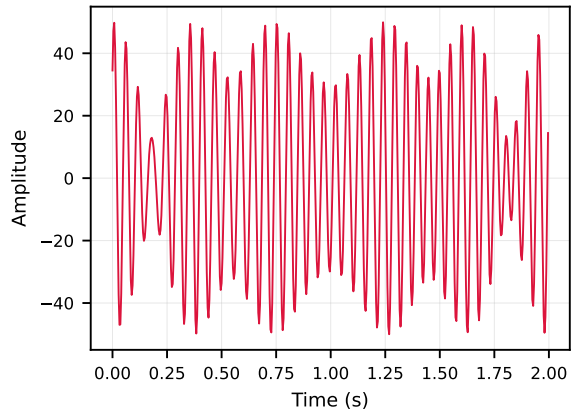

Figure B.23: Weighted time signal, run 74.

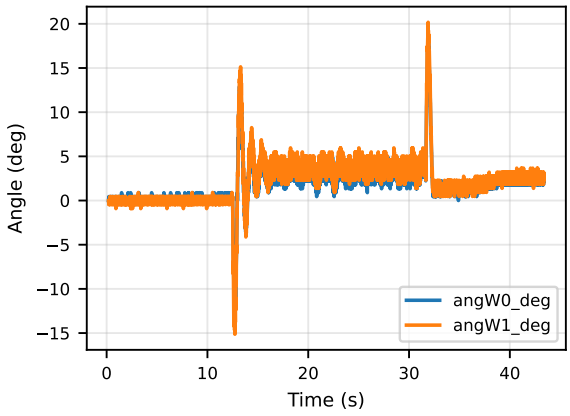

Figure B.24: Raw time signals (input and output), run 74. Output despiked.

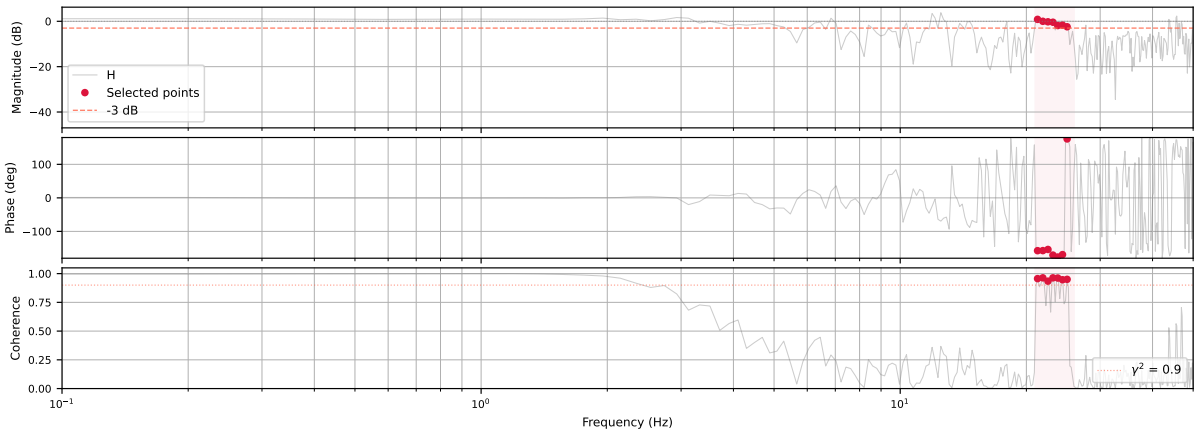

Figure B.25: Measured FRF, run 74 (17 Hz to 20 Hz).

B.2.0.6 Combined FRF

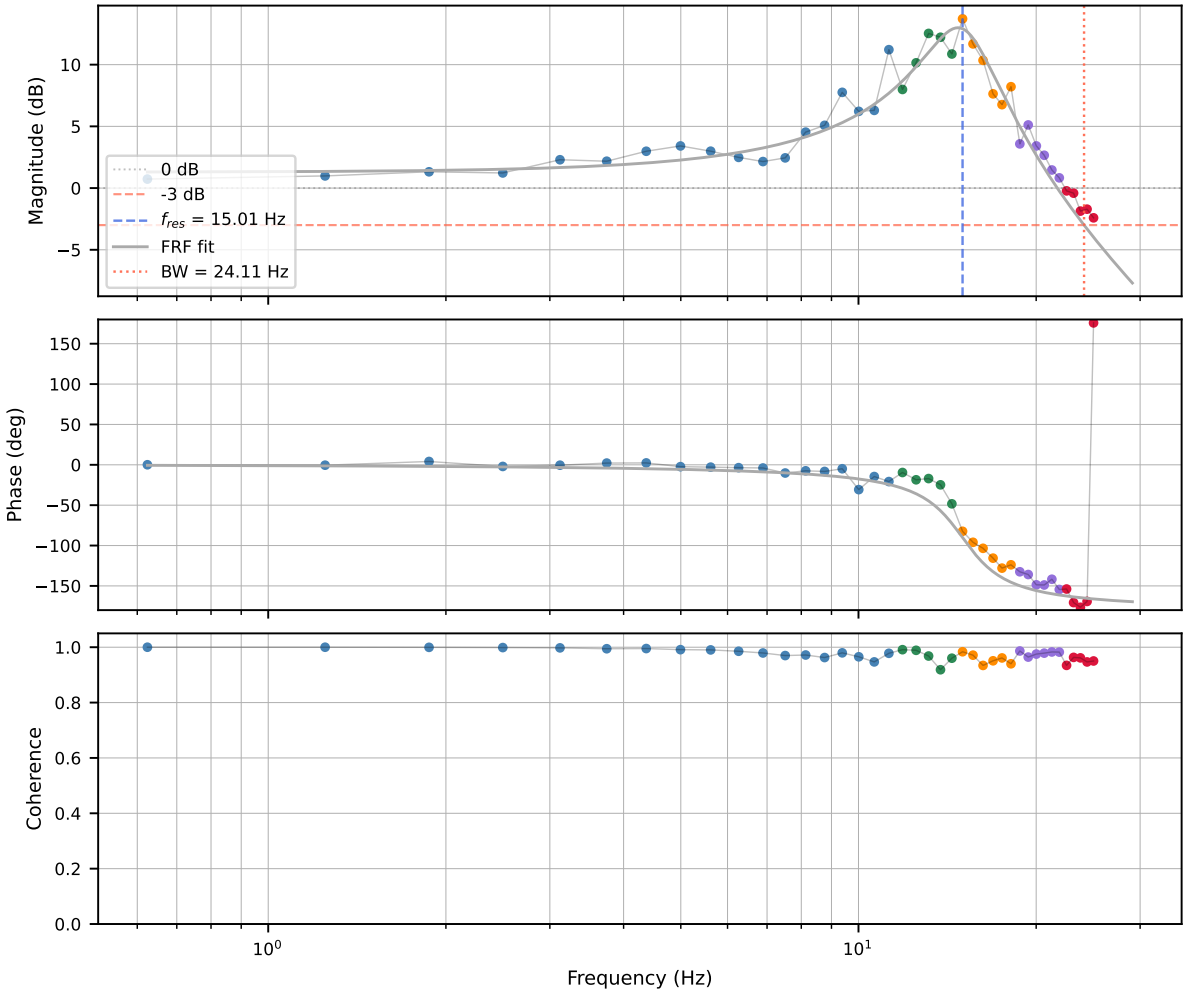

Figure B.26: Combined FRF of the Square Configuration, assembled from runs 56, 79, 80, 73, and 74. The FRF fit identifies a resonance at $f_{\mathrm{res}} = 15.01\,\mathrm{Hz}$ and predicts a $-3\,\mathrm{dB}$ bandwidth of 24.11 Hz.

B.3 Signals: Straight-Line Configuration

Table B.2 summarizes the measurement parameters for each run of the Straight-Line Configuration. Twelve runs were conducted, covering the frequency range 0.5 Hz to 37.5 Hz in overlapping bands. Signal amplitude was increased for runs above 24.5 Hz to compensate for reduced actuator authority at higher frequencies. Both input and output signals were despiked in all runs. Run 95 used a frequency resolution of $\Delta f = 0.25$ Hz; all other runs used $\Delta f = 0.5$ Hz.

Table B.2: Signal parameters for the Straight-Line Configuration measurement runs. $\Delta f = 0.5$ Hz except run 95 ($\Delta f = 0.25$ Hz). Proprio stiffness setting = 200/600.

Run	Freq. band (Hz)	PSD band (Hz)	Signal Amp.	Gain	Despiking	$P_{\min}$ (dB)
85	0.5–10	0–13	500	15	XY	42
88	9.5–12.5	11.5–16	5000	15	XY	50
89	12–15.5	14.5–19	5000	15	XY	15
92	15–17.5	18.5–22	5000	15	XY	15
95	17–21	21–26	5000	15	XY	15
96	19.5–22.5	24–28.5	5000	15	XY	15
97	22–25	27–31.5	5000	15	XY	30
100	24.5–27.5	30.5–34.5	20000	15	XY	15
102	27–30	33.5–38	20000	15	XY	15
103	29.5–32.5	36.5–41	20000	15	XY	30
105	32–35	40–43	30000	15	XY	15
107	34.5–37.5	42.5–47	30000	15	XY	15

Despiking notation: X = input signal despiked; Y = output signal despiked.

B.3.0.1 Run 85 (0.5 Hz to 10 Hz)

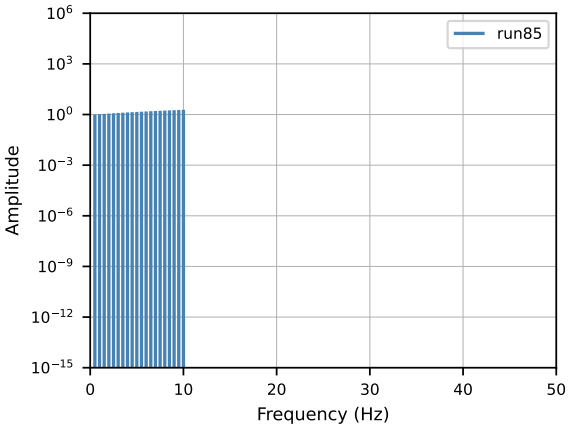

Figure B.27: Weighted input spectrum, run 85.

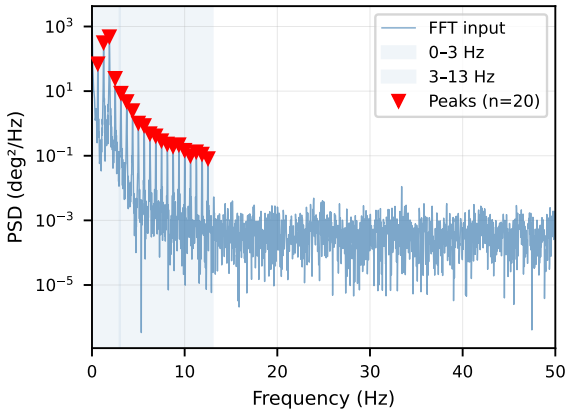

Figure B.28: PSD of input signal, run 85. Detected peaks indicated.

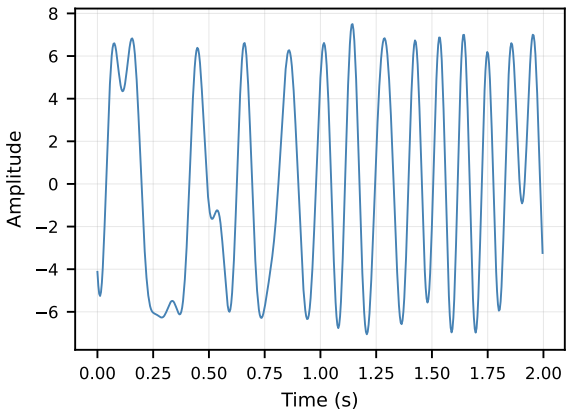

Figure B.29: Weighted time signal, run 85.

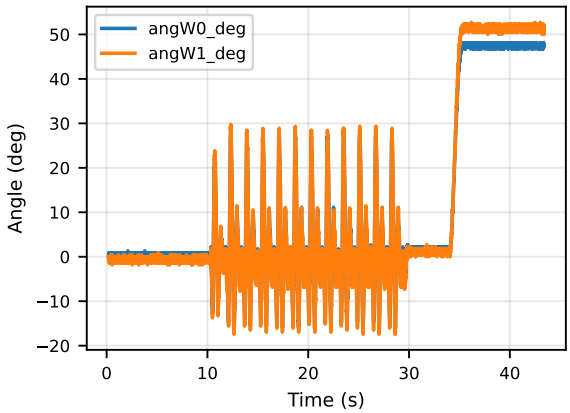

Figure B.30: Raw time signals (input and output), run 85. Both signals despiked.

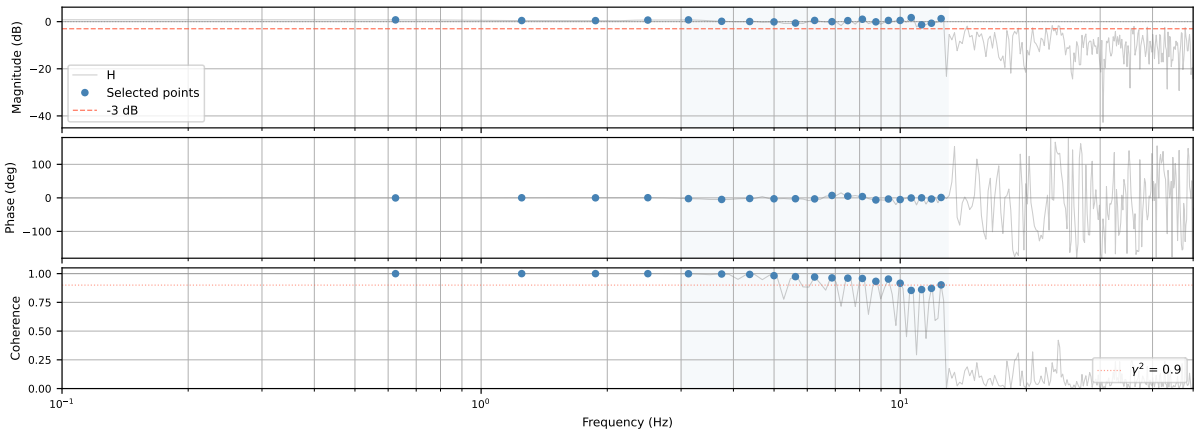

Figure B.31: Measured FRF, run 85 (0.5 Hz to 10 Hz).

B.3.0.2 Run 88 (9.5 Hz to 12.5 Hz)

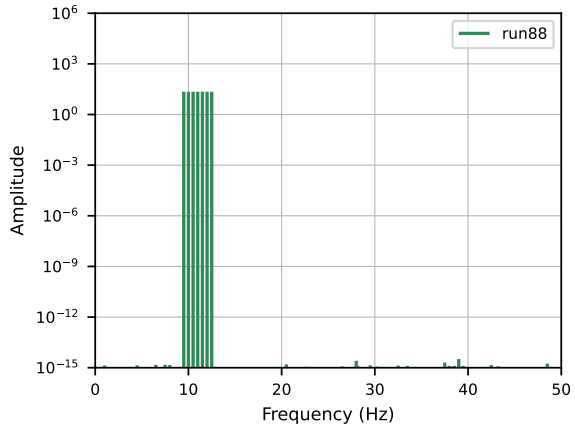

Figure B.32: Weighted input spectrum, run 88.

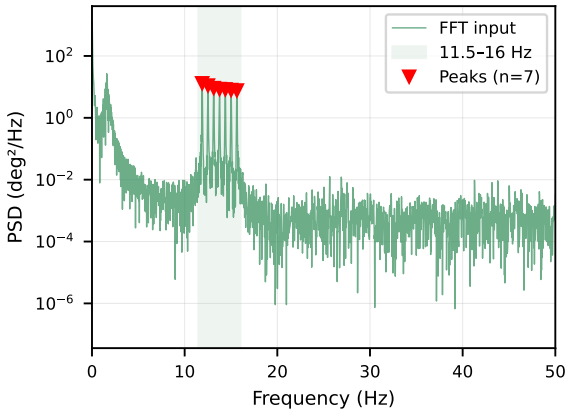

Figure B.33: PSD of input signal, run 88. Detected peaks indicated.

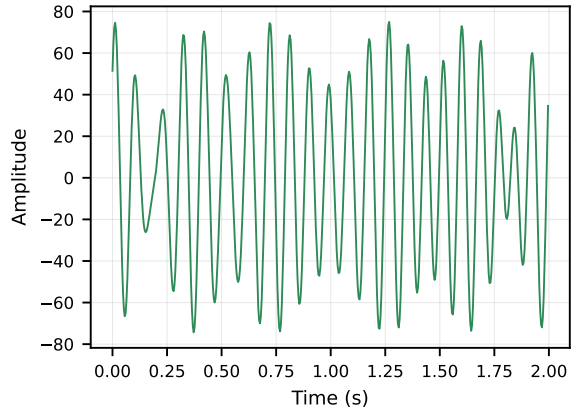

Figure B.34: Weighted time signal, run 88.

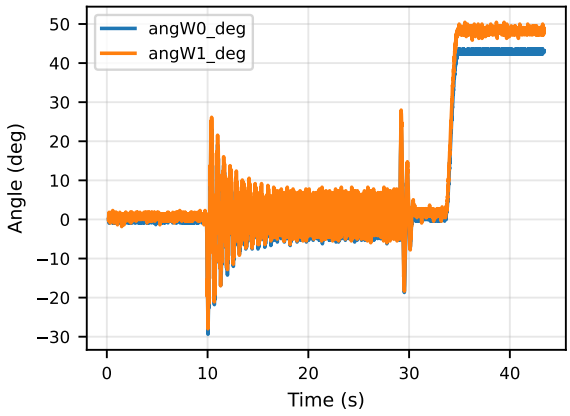

Figure B.35: Raw time signals (input and output), run 88. Both signals despiked.

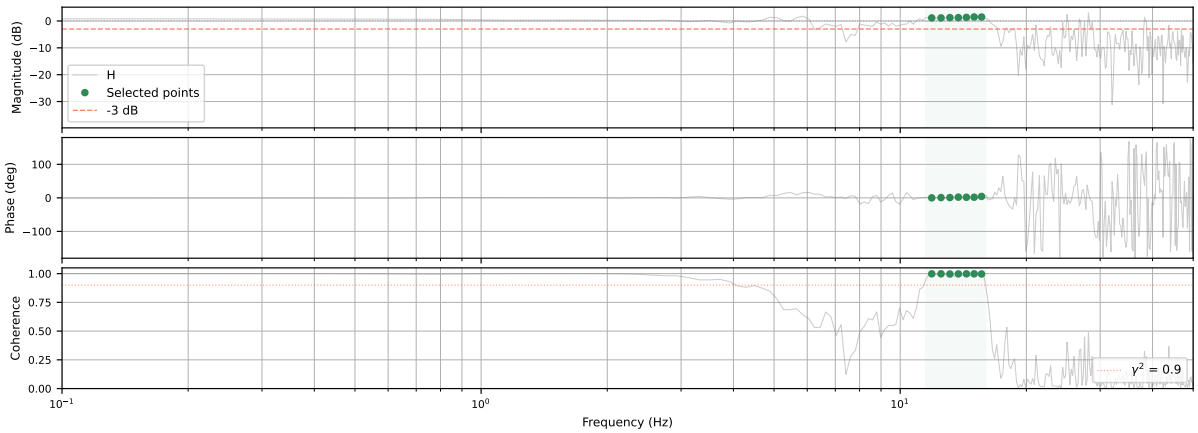

Figure B.36: Measured FRF, run 88 (9.5 Hz to 12.5 Hz).

B.3.0.3 Run 89 (12 Hz to 15.5 Hz)

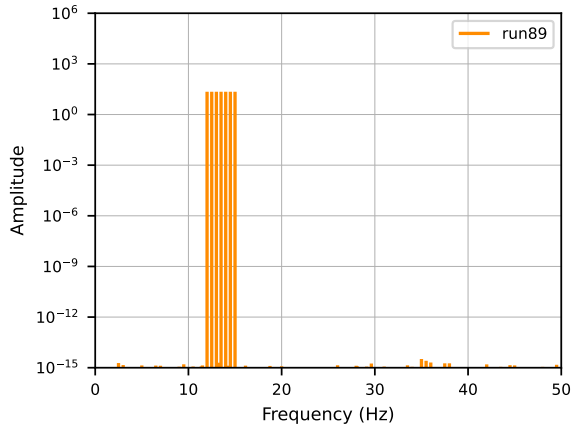

Figure B.37: Weighted input spectrum, run 89.

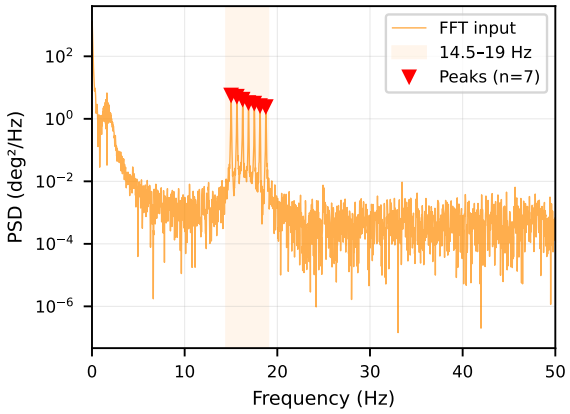

Figure B.38: PSD of input signal, run 89. Detected peaks indicated.

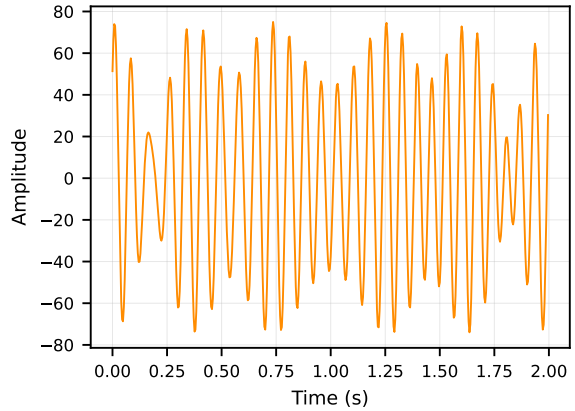

Figure B.39: Weighted time signal, run 89.

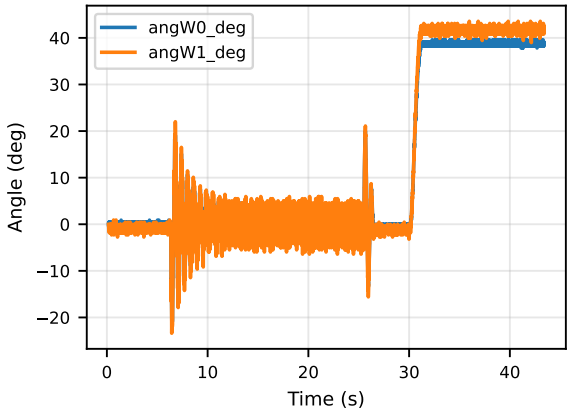

Figure B.40: Raw time signals (input and output), run 89. Both signals despiked.

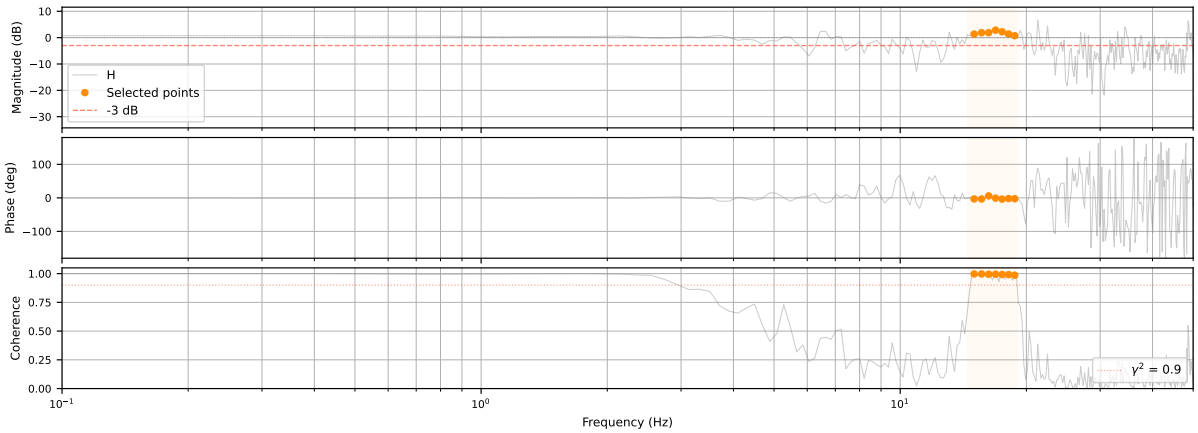

Figure B.41: Measured FRF, run 89 (12 Hz to 15.5 Hz).

B.3.0.4 Run 92 (15 Hz to 17.5 Hz)

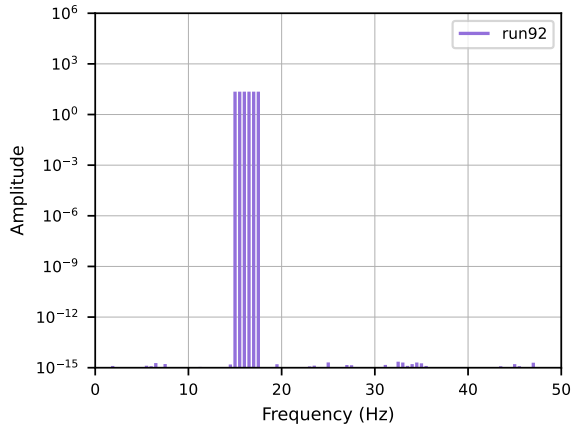

Figure B.42: Weighted input spectrum, run 92.

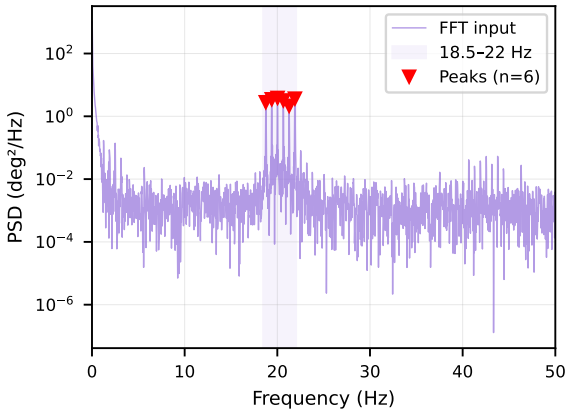

Figure B.43: PSD of input signal, run 92. Detected peaks indicated.

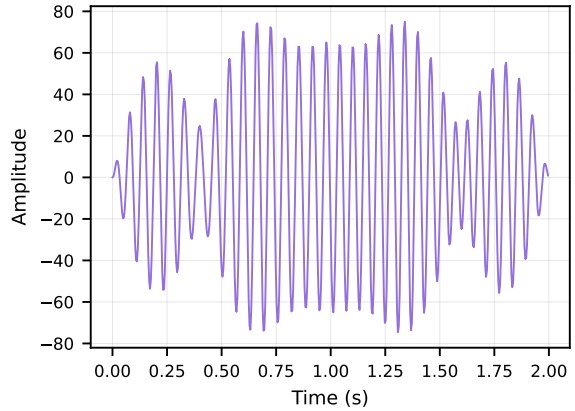

Figure B.44: Weighted time signal, run 92.

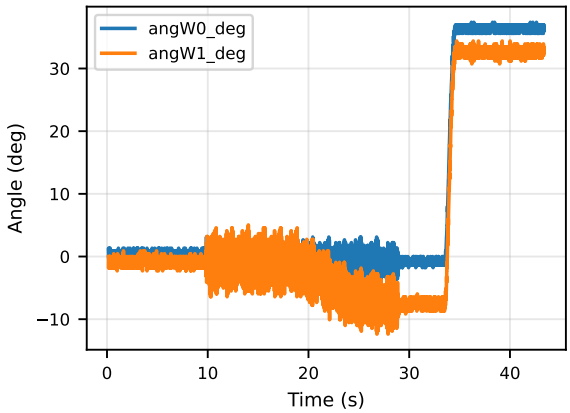

Figure B.45: Raw time signals (input and output), run 92. Both signals despiked.

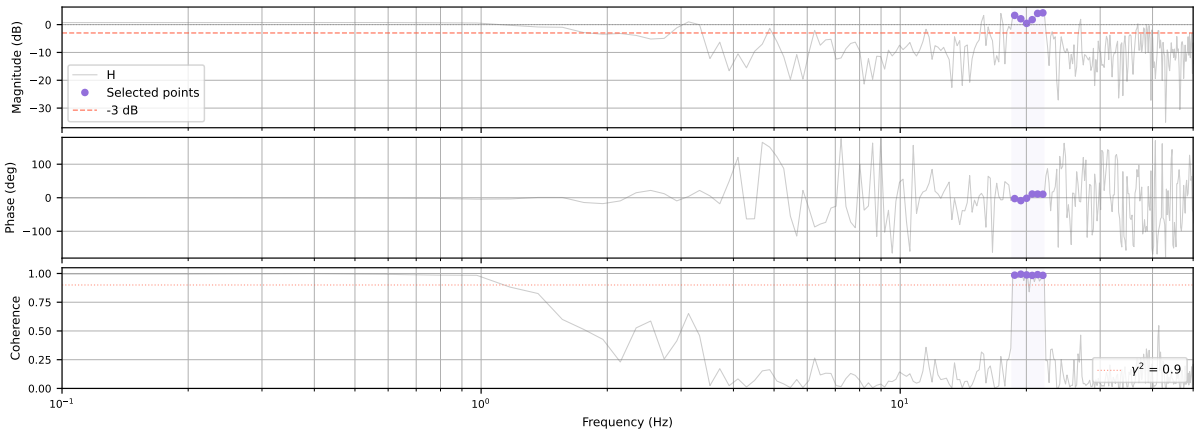

Figure B.46: Measured FRF, run 92 (15 Hz to 17.5 Hz).

B.3.0.5 Run 95 (17 Hz to 21 Hz)

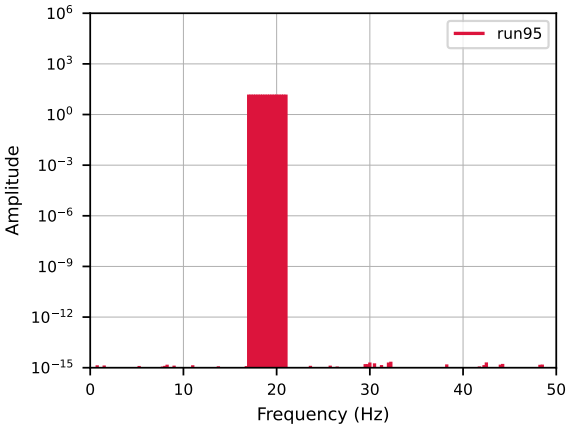

Figure B.47: Weighted input spectrum, run 95.

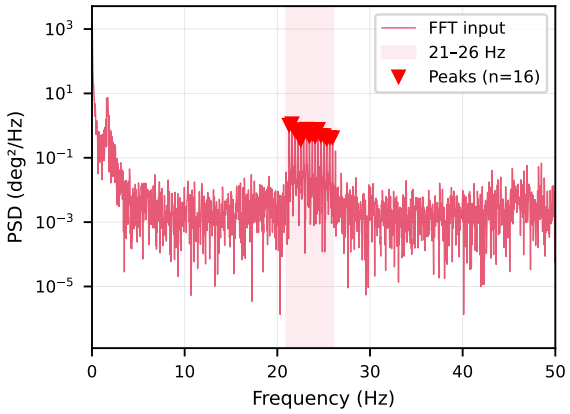

Figure B.48: PSD of input signal, run 95. Detected peaks indicated.

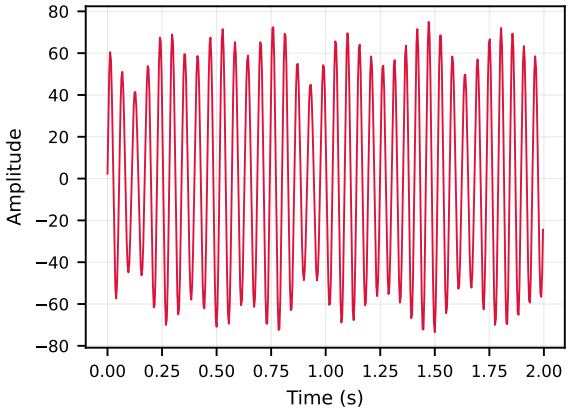

Figure B.49: Weighted time signal, run 95.

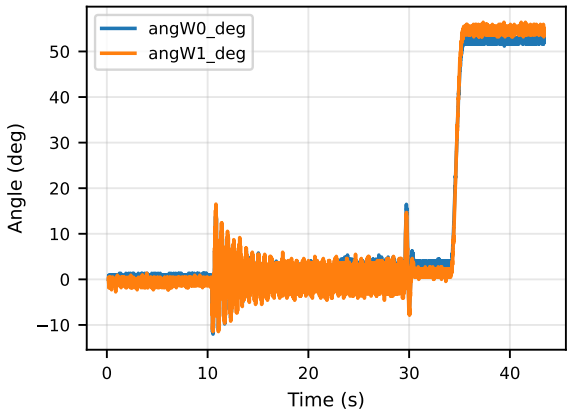

Figure B.50: Raw time signals (input and output), run 95. Both signals despiked. $\Delta f = 0.25\,\text{Hz}$.

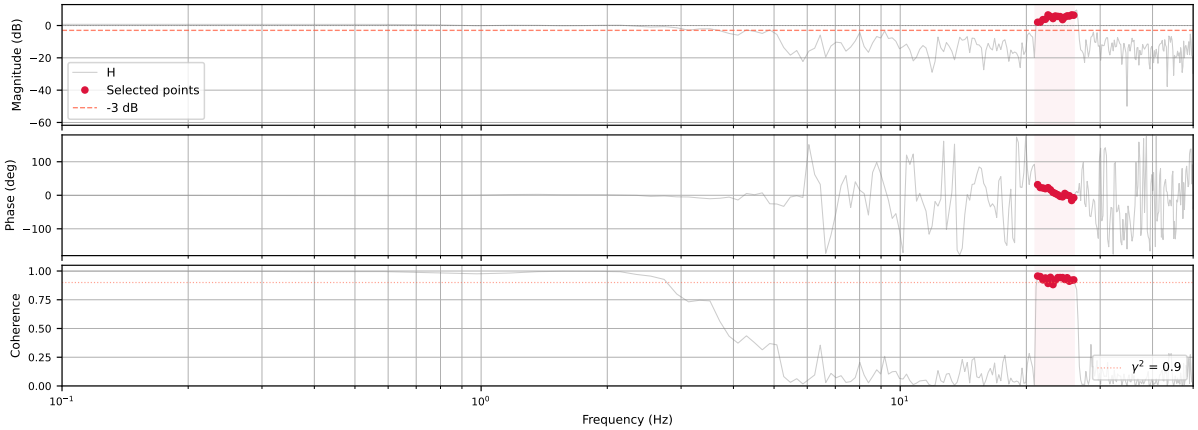

Figure B.51: Measured FRF, run 95 (17 Hz to 21 Hz).

B.3.0.6 Run 96 (19.5 Hz to 22.5 Hz)

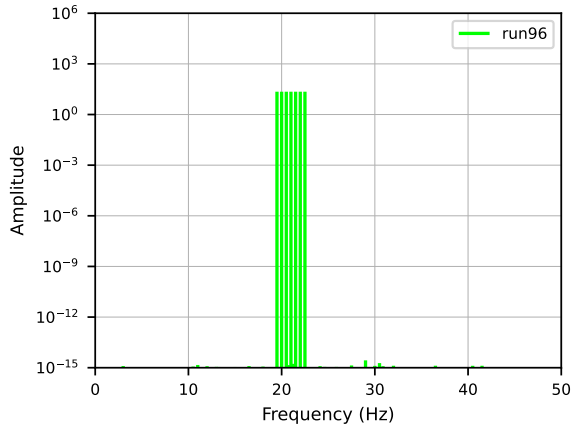

Figure B.52: Weighted input spectrum, run 96.

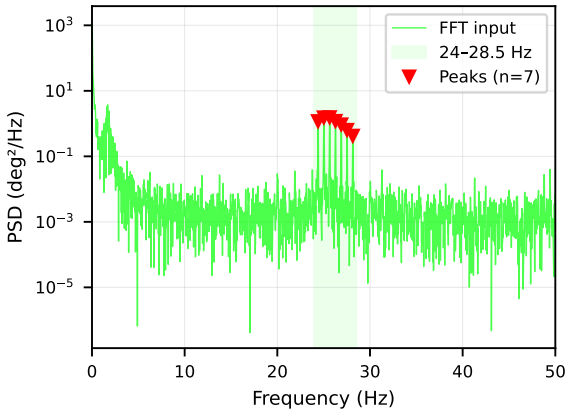

Figure B.53: PSD of input signal, run 96. Detected peaks indicated.

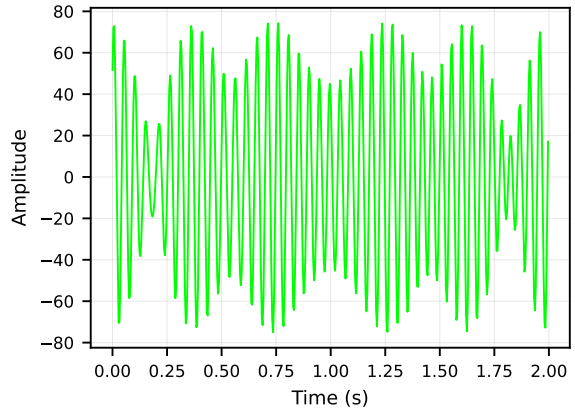

Figure B.54: Weighted time signal, run 96.

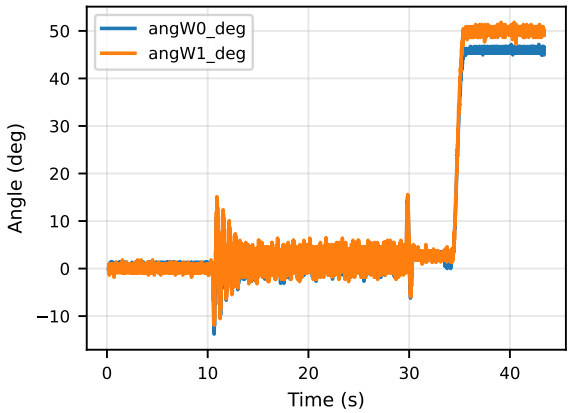

Figure B.55: Raw time signals (input and output), run 96. Both signals despiked.

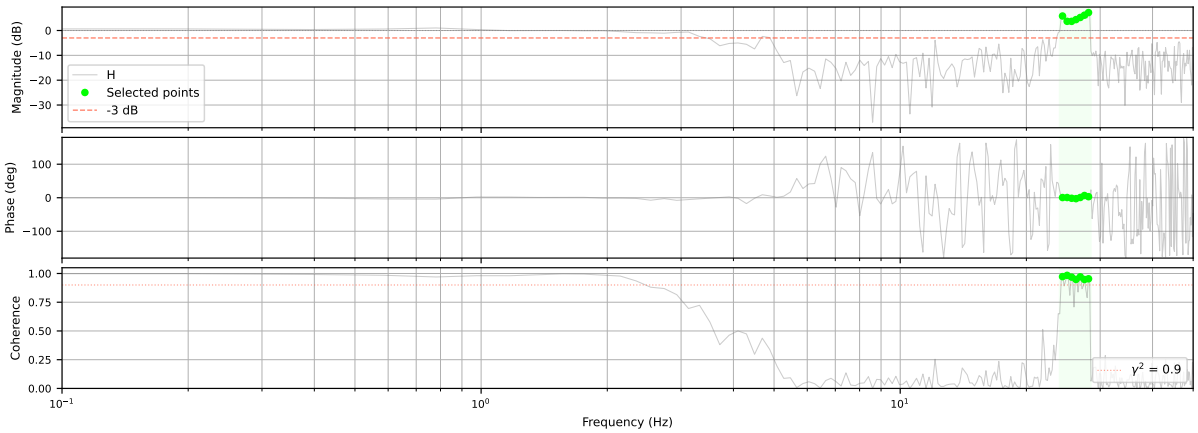

Figure B.56: Measured FRF, run 96 (19.5 Hz to 22.5 Hz).

B.3.0.7 Run 97 (22 Hz to 25 Hz)

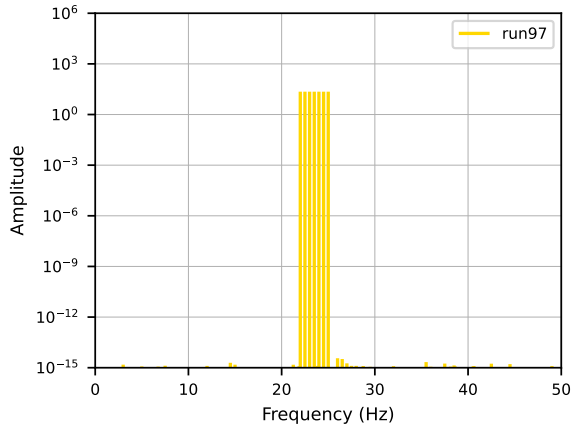

Figure B.57: Weighted input spectrum, run 97.

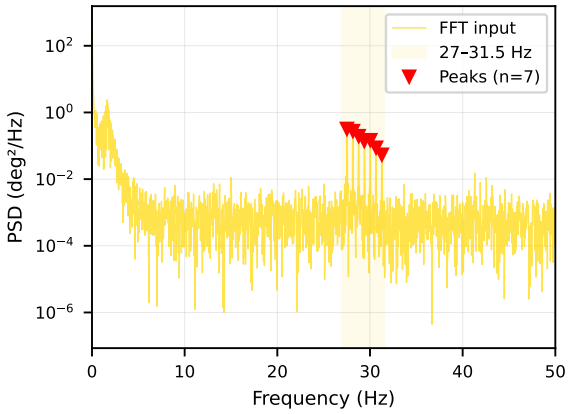

Figure B.58: PSD of input signal, run 97. Detected peaks indicated.

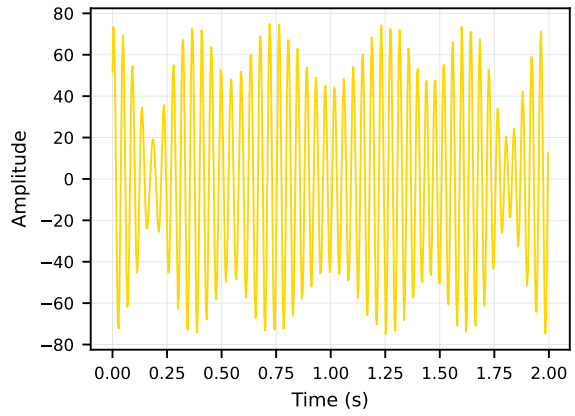

Figure B.59: Weighted time signal, run 97.

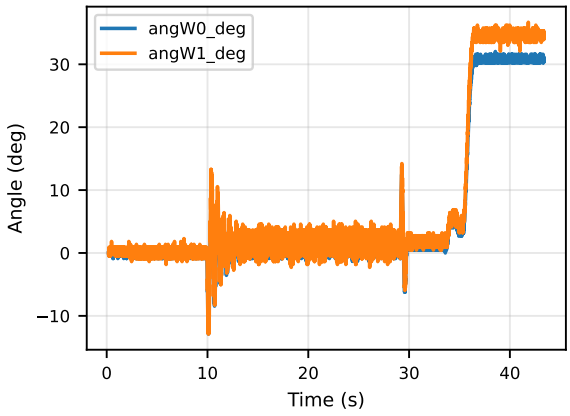

Figure B.60: Raw time signals (input and output), run 97. Both signals despiked.

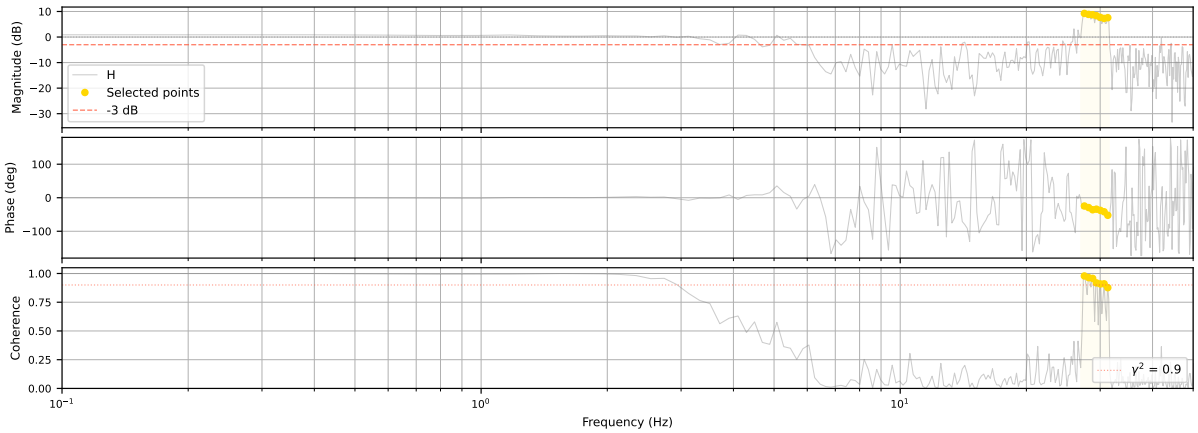

Figure B.61: Measured FRF, run 97 (22 Hz to 25 Hz).

B.3.0.8 Run 100 (24.5 Hz to 27.5 Hz)

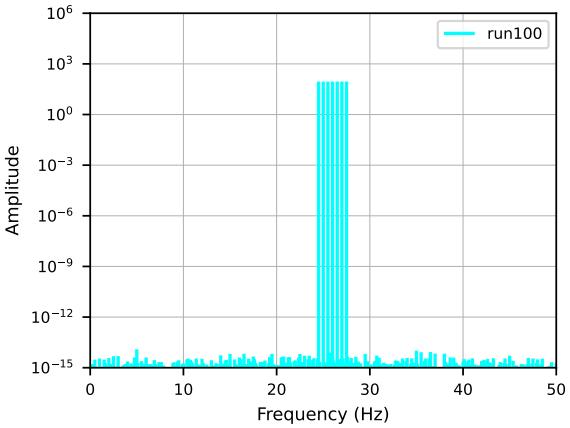

Figure B.62: Weighted input spectrum, run 100.

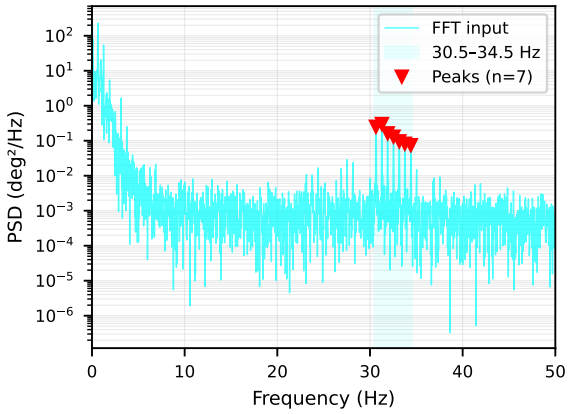

Figure B.63: PSD of input signal, run 100. Detected peaks indicated.

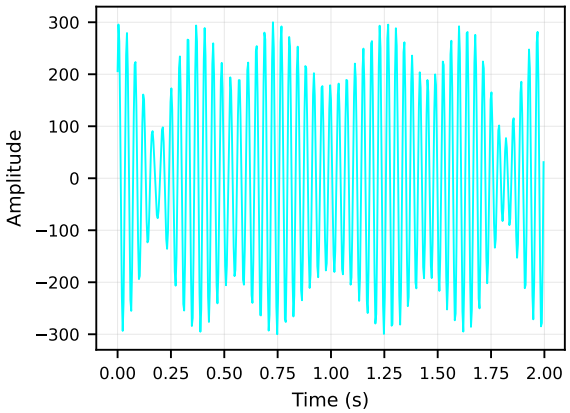

Figure B.64: Weighted time signal, run 100.

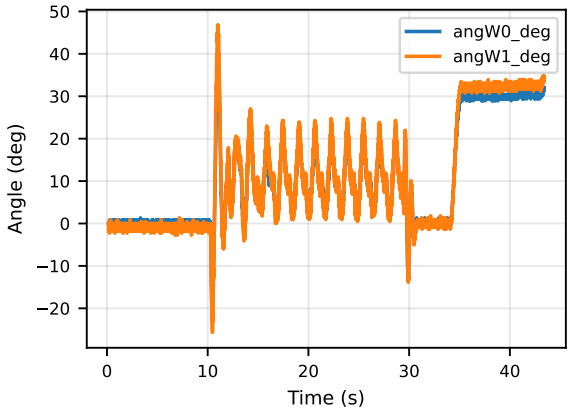

Figure B.65: Raw time signals (input and output), run 100. Both signals despiked.

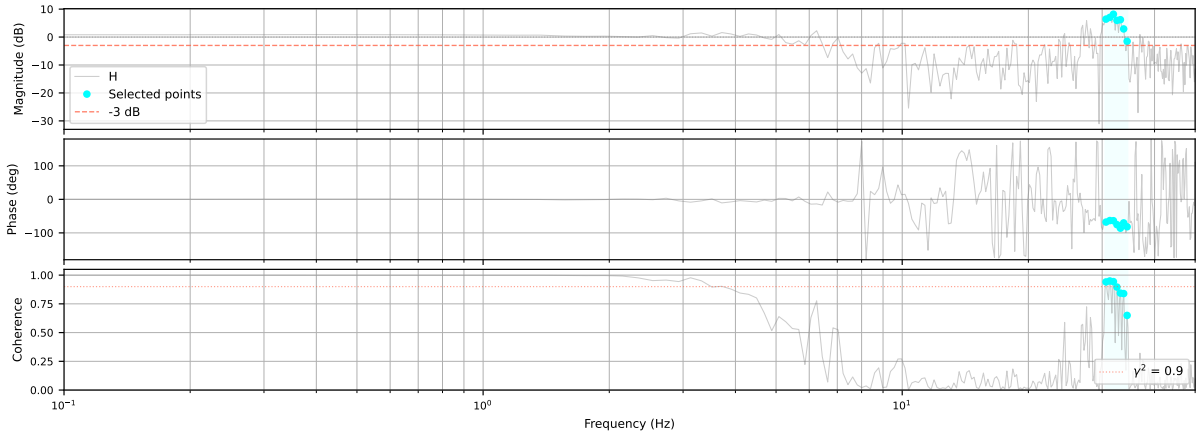

Figure B.66: Measured FRF, run 100 (24.5 Hz to 27.5 Hz).

B.3.0.9 Run 102 (27 Hz to 30 Hz)

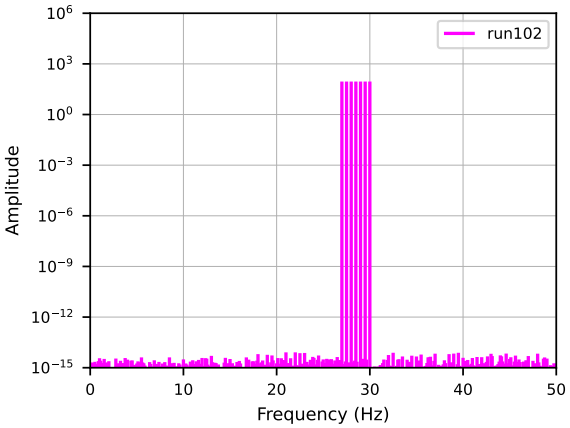

Figure B.67: Weighted input spectrum, run 102.

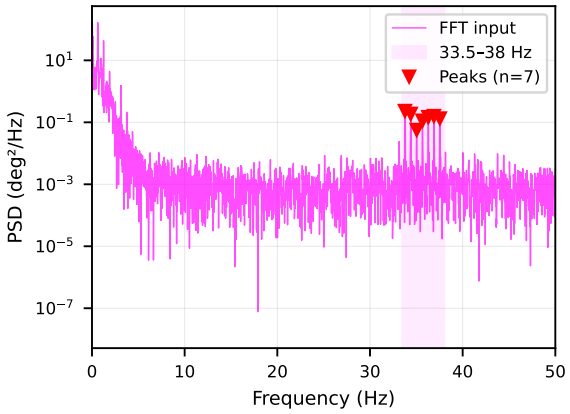

Figure B.68: PSD of input signal, run 102. Detected peaks indicated.

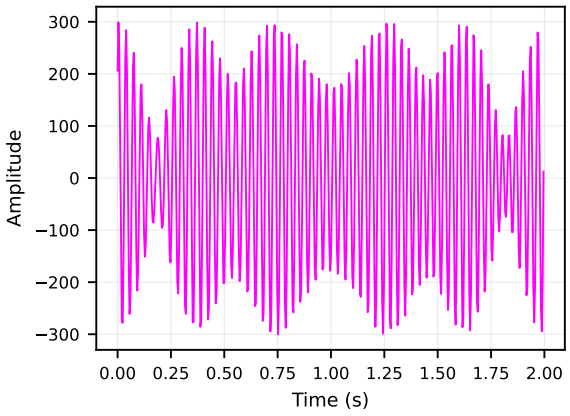

Figure B.69: Weighted time signal, run 102.

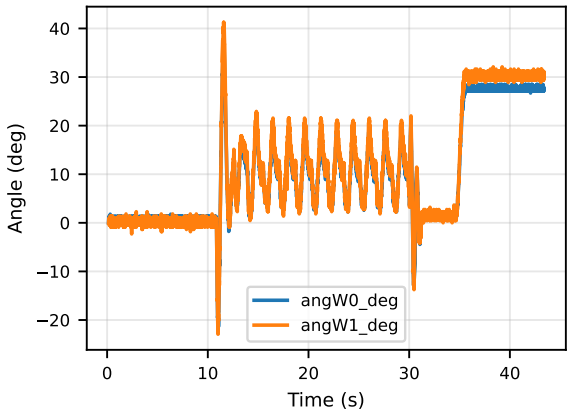

Figure B.70: Raw time signals (input and output), run 102. Both signals despiked.

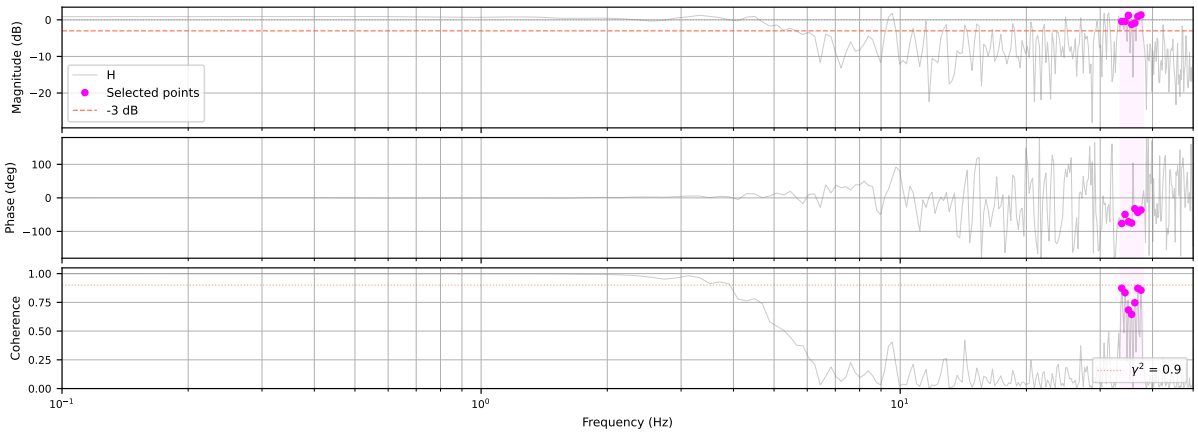

Figure B.71: Measured FRF, run 102 (27 Hz to 30 Hz).

B.3.0.10 Run 103 (29.5 Hz to 32.5 Hz)

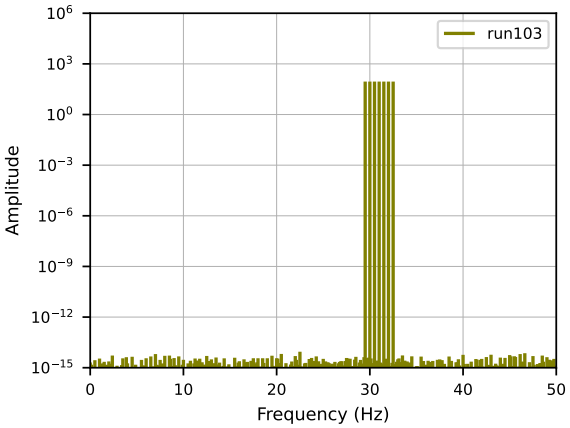

Figure B.72: Weighted input spectrum, run 103.

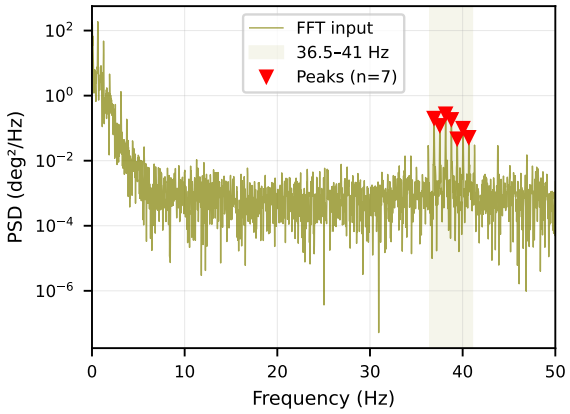

Figure B.73: PSD of input signal, run 103. Detected peaks indicated.

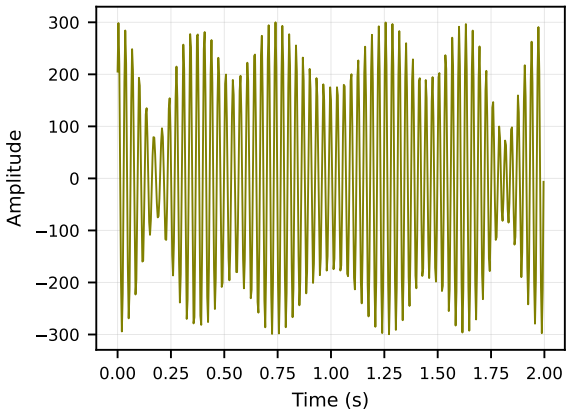

Figure B.74: Weighted time signal, run 103.

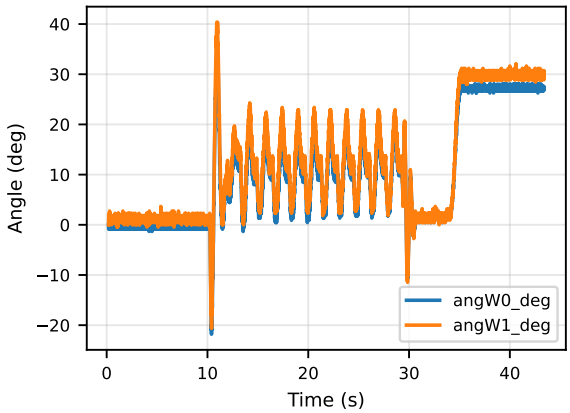

Figure B.75: Raw time signals (input and output), run 103. Both signals despiked.

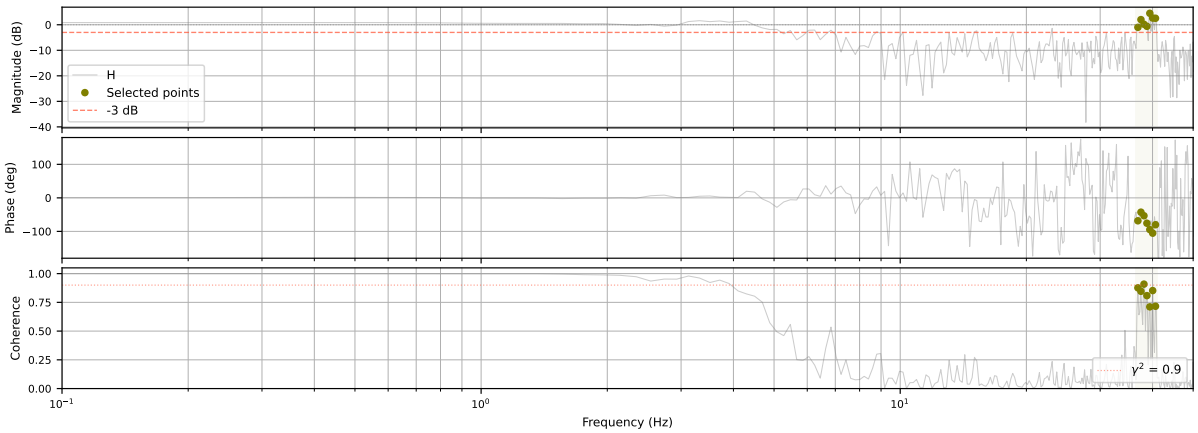

Figure B.76: Measured FRF, run 103 (29.5 Hz to 32.5 Hz).

B.3.0.11 Run 105 (32 Hz to 35 Hz)

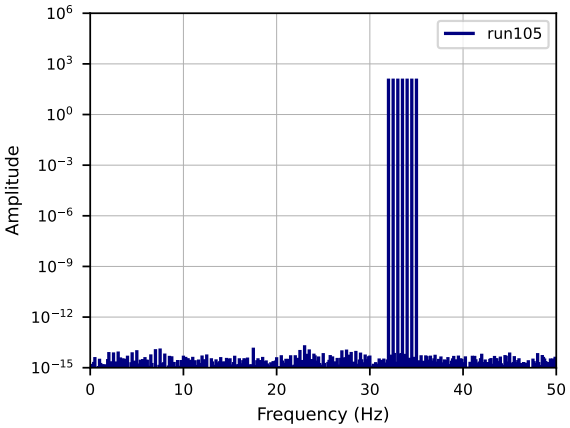

Figure B.77: Weighted input spectrum, run 105.

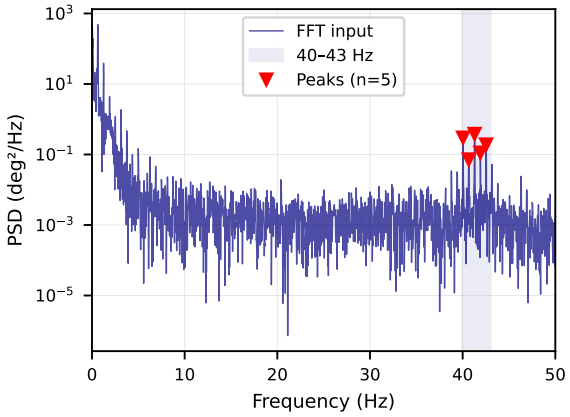

Figure B.78: PSD of input signal, run 105. Detected peaks indicated.

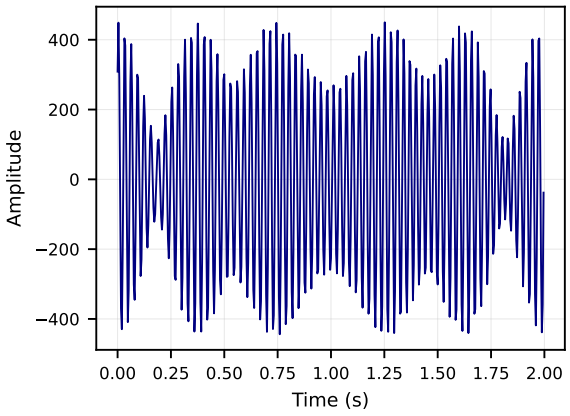

Figure B.79: Weighted time signal, run 105.

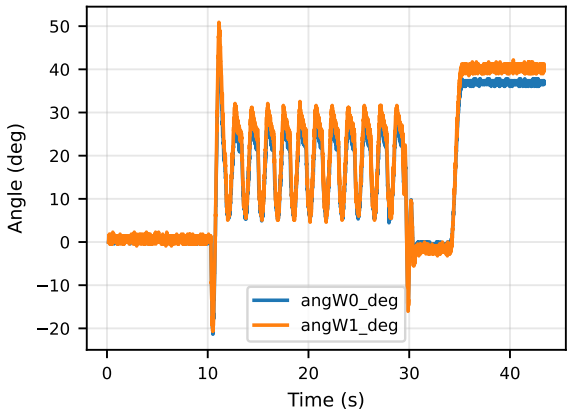

Figure B.80: Raw time signals (input and output), run 105. Both signals despiked.

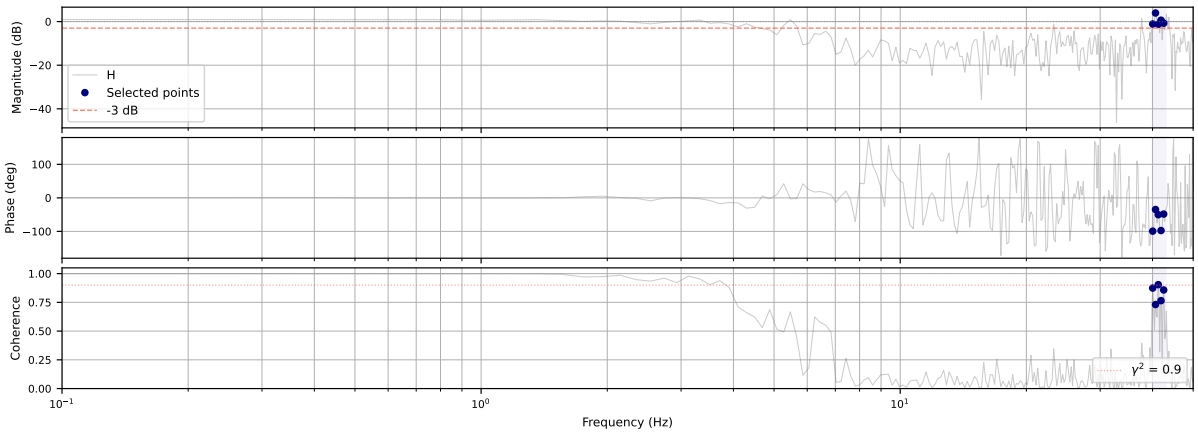

Figure B.81: Measured FRF, run 105 (32 Hz to 35 Hz).

B.3.0.12 Run 107 (34.5 Hz to 37.5 Hz)

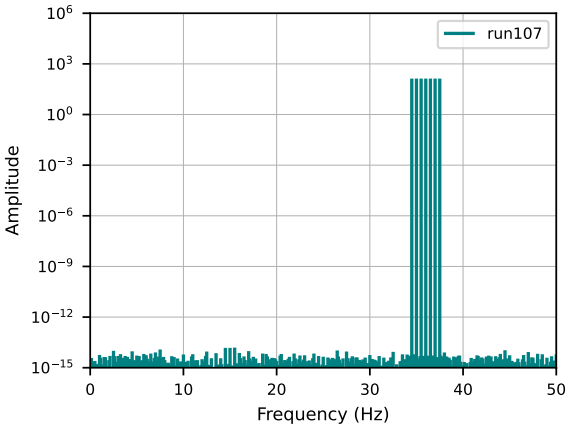

Figure B.82: Weighted input spectrum, run 107.

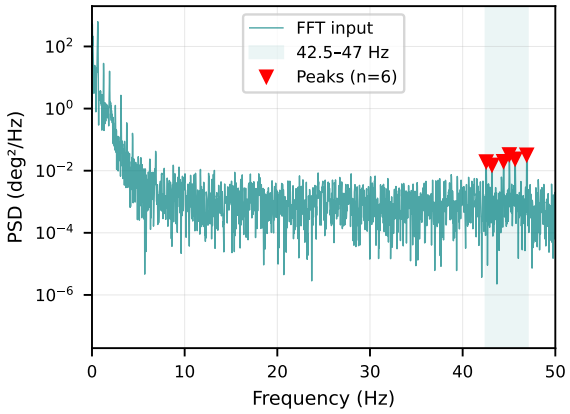

Figure B.83: PSD of input signal, run 107. Detected peaks indicated.

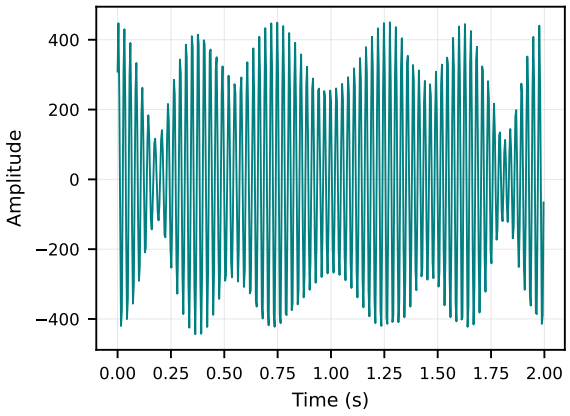

Figure B.84: Weighted time signal, run 107.

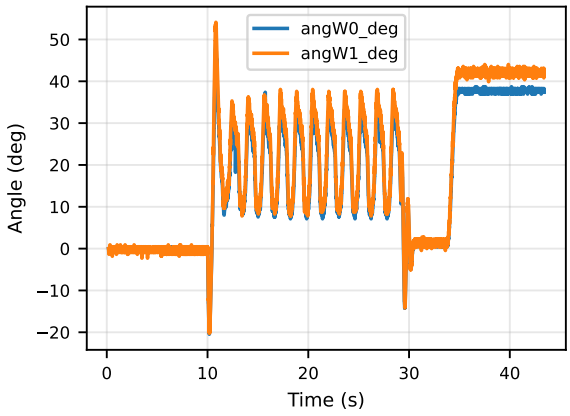

Figure B.85: Raw time signals (input and output), run 107. Both signals despiked.

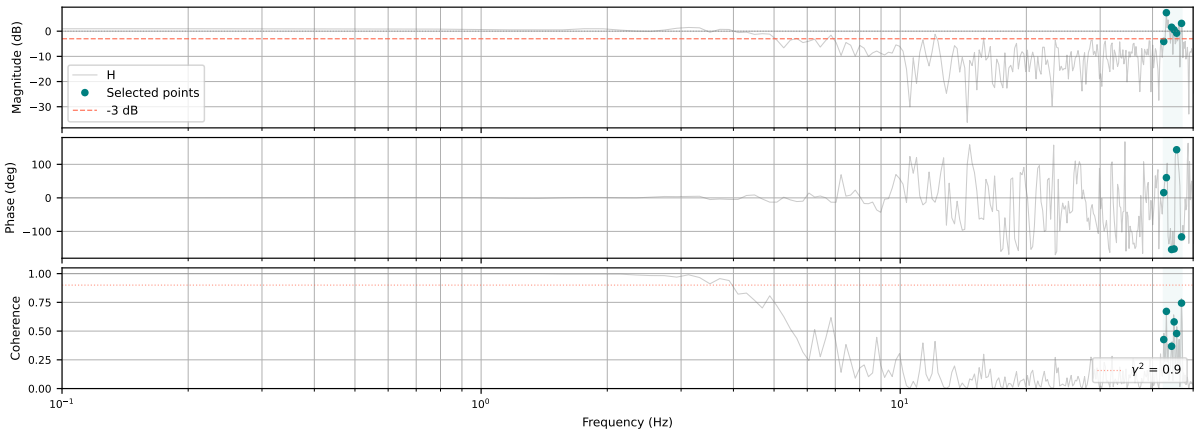

Figure B.86: Measured FRF, run 107 (34.5 Hz to 37.5 Hz).

B.3.0.13 Combined FRF

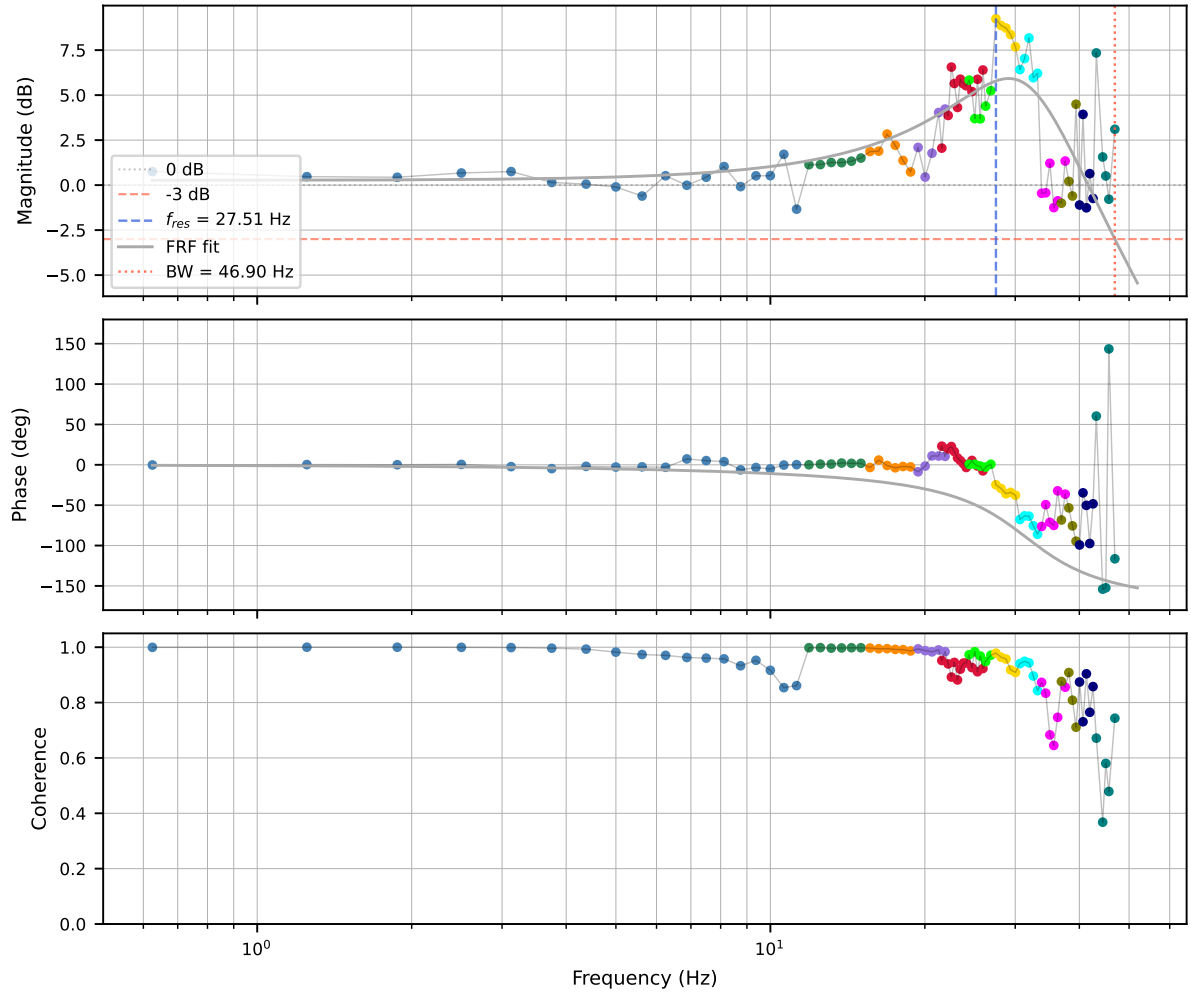

Figure B.87: Combined FRF of the Straight-Line Configuration, assembled from runs 85, 88, 89, 92, 95, 96, 97, 100, 102, 103, 105, and 107. The FRF fit identifies a resonance at $f_{\mathrm{res}} = 27.51\,\mathrm{Hz}$ and extrapolates a $-3\,\mathrm{dB}$ bandwidth of 46.90 Hz. The $-3\,\mathrm{dB}$ crossing lies beyond the measured frequency range; the reported bandwidth is a model extrapolation.